
A CMOS camera employing a double junction active pixel

Keith Michael Findlater



A thesis submitted for the degree of Doctor of Philosophy.
The University of Edinburgh.
June 2001



Abstract

Solid-state image sensors usually employ a checker-board array of red, green and blue (RGB) filters to perform colour imaging. Due to this, only one third of the incident light gets converted into output signal. Additionally, in the most commonly used arrangement, twice as many pixels are allocated to sense green compared to red or blue, producing an uneven sampling of the three colour signals throughout the image. This results in more severe aliasing in the red and blue channels relative to green.

This thesis investigates the colour imaging performance that can be obtained by combining the inherent spectral dependence of light absorption depth in silicon with a suitable colour filter array. This colour filter array can contain less colours of wider bandwidth, which makes more efficient use of the illumination. A novel active pixel is developed which contains two photo-junctions stacked vertically in the silicon. Device simulation of the spectral response, along with quantum efficiency measurement, is used to assess the raw spectral selectivity of the double junction structure in two standard CMOS technologies. The response with various colour filter combinations is also presented showing that colour imaging with only two filters should be possible.

Active pixel circuitry suitable for such a photo-diode structure is discussed, and the calculated noise performance for the double junction pixel is compared with the standard 3-transistor active pixel. This analysis shows that comparable performance can be achieved using the new pixel type. The design of a simple analogue output 184 x 154 pixel image sensor using the double junction pixel is described. A full characterisation of the performance of the sensor is presented and results compared with a standard sensor.

In order to complete a camera system, the processing needed to obtain colour images is implemented in software. Example images from the new camera are given and the colorimetric accuracy of the sensor with different filter combinations is discussed. Results show that the colour reproduction, though acceptable, is not yet as accurate as with a standard RGB sensor. Test patterns are used to examine the aliasing artifacts of the camera. Again, comparison with the standard approach is used to highlight the relative strengths and weaknesses.

Finally, a critical discussion of the double junction approach is given. Suggestions for improvements to the techniques used in this work are made, along with ideas for future research that depend on predicted developments in image sensor technology.

Declaration of originality

I hereby declare that the research recorded in this thesis and the thesis itself was composed and originated entirely by myself in the Department of Electronics and Electrical Engineering at The University of Edinburgh, and at STMicroelectronics Imaging Division, Edinburgh.

Other people who have contributed significantly to this work are acknowledged at the appropriate places in the thesis text.

Keith M Findlater

Acknowledgements

There are many people that I would like to thank. Firstly, my academic supervisor, Dr. David Renshaw, has provided an exceptionally good level of supervision throughout this project. His relaxed manner and excellent humour, combined with a keen interest in the project material, always made our discussions both useful and enjoyable.

Next, a big thank you to my industrial supervisor Dr. Robert K. Henderson. Not only was he very generous with his time and knowledge of analogue design, he also made me pick up my badminton racket once again for which I will be eternally grateful. Thanks also to my second (unofficial) industrial supervisor and future boss J.E.D. Hurwitz who provided the original idea for the project. I do not think there is much chance that he will ever run out of ideas, or enthusiasm for the field of image sensors, which can only be a good thing.

I would not have been able to undertake this work without the support of EPSRC grant 98318217 and the CASE sponsorship of STMicroelectronics Imaging Division. My summer work at ST was also very valuable, from a training point of view as well as financially.

I feel that I have benefitted greatly from working with many people at STMicroelectronics. Drew Holmes, Donald Baxter, Toby Bailey, and all the sensor design team at ST have helped me acquire the necessary knowledge to complete this work. More importantly, they are a great bunch of people to work with, always friendly, and always interested. The same applies to the technology group: Lindsay Grant, Stewart Smith, Andrew 'Nonsense' Murray, and Jeff Raynor, who have always been a great help. Many other people from various groups in ST have helped me, notably Berend Meijer and Elaine Paris with test structure measurement and equipment setup.

My fellow research students at ST have also been great to work with. Thanks to Matthew Purcell for many arguments and discussions, some useful, some pointless, all of them entertaining. May your culinary genius last forever. Thanks to Graeme Storm for introducing me to Edinburgh University Badminton Club during my eighth year here, and showing me just how much progress I could still make! Better late than never.

Thanks also to my colleagues in the Vision systems and Integrated Systems Groups at Edin-

burgh University, especially Andrew Peacock in developing the Vision systems code library, for all their help, feedback on the project, and nights out.

Perhaps most importantly of all, lots of love to all my good friends in Edinburgh: Matthew Lynch, Damon Thompson, Katy Fisher, Andrew Dempster, Eric Volk, and my sister Kate, and everyone else (you know who you are).

No thank you list would be complete without a mention of my parents, Marion and Brian, who have instilled me with a desire to learn, to be self-sufficient, and who always encouraged me to do the best I could in academia. This thesis is for them. Thanks also to the rest of my family, including my brother Andy, for all their advice and encouragement over the years.

Finally, thanks and lots of love to my girlfriend Lindsay, who throughout the past 3 years has put up with my erratic working patterns, techno-babble, and drifts into image sensor land over dinner, with incredible patience (yes really).

Thank you all.

Keith M Findlater

21 May 2001

Contents

Declaration of originality	iii
Acknowledgements	iv
Contents	v
List of figures	ix
List of tables	xiii
Acronyms and abbreviations	xiv
1 Introduction	1
1.1 Image sensors	1
1.2 Human vision	2
1.3 Camera systems	3
1.3.1 Breakdown	3
1.3.2 Optics	4
1.3.3 Image sensor	5
1.3.4 Signal processing	11
1.4 This project	14
1.4.1 A two-colour CFA	15
1.4.2 A two-colour pixel	16
1.4.3 Possible benefits and disadvantages	16
1.5 Project aims	17
1.6 Methodologies	18
1.7 Breakdown of thesis structure	18
2 Background	20
2.1 Introduction	20
2.2 Photo-diode physics	20
2.2.1 Spectral response and sensitivity	20
2.2.2 Dark current	23
2.3 Solid-state colour sensors	24
2.3.1 Bulk silicon	24
2.3.2 Bias voltage based	28
2.3.3 Thin film	29
2.3.4 Summary	33
2.4 CMOS pixel circuits	34
2.4.1 1-transistor pixel	35
2.4.2 3-transistor pixel	36
2.4.3 3-transistor cell with cascode	38
2.4.4 4-transistor pixel	38
2.4.5 Logarithmic pixel	40
2.4.6 Summary of pixel circuits	42
2.5 Conclusion	43

3	TCAD modelling of photo-diode structures	44
3.1	Introduction	44
3.2	TCAD methodology	44
3.2.1	Simulator limitations	44
3.2.2	Experimental procedure	46
3.3	Standard diode results and experiments	47
3.3.1	Base case	47
3.3.2	Effect of epitaxial layer	48
3.3.3	Cross-talk	51
3.4	Double junction preliminary results	51
3.5	DJ optimisation	54
3.5.1	Experimental design	54
3.5.2	Analysis of main effects	54
3.5.3	Optimisation	58
3.6	Conclusion	59
4	Quantum efficiency measurements	60
4.1	Introduction	60
4.2	Test structure design	60
4.3	Measurement setup	61
4.4	Unfiltered results	62
4.4.1	0.35 μm technology	63
4.4.2	0.5 μm technology	64
4.5	Results with filters	66
4.6	Conclusion	68
5	Sensor design	69
5.1	Introduction	69
5.2	Double junction active pixel circuits	69
5.2.1	Six transistor pixel	69
5.2.2	Eight transistor pixel	72
5.3	Pixel noise analysis	74
5.3.1	Factors limiting the signal	74
5.3.2	Sources of noise in active pixels	76
5.3.3	Signal to noise ratio	77
5.3.4	Results of analysis	78
5.4	Pixel layout	82
5.4.1	6-T pixel	82
5.4.2	8-T pixel	84
5.5	Sensor overview	88
5.5.1	Output signal chain	89
5.5.2	Verification	90
5.6	Conclusions	90
6	Sensor characterisation	92
6.1	Introduction	92
6.2	Noise as a measurement tool	92

6.2.1	Photon-transfer curve of the double junction sensor	95
6.3	Charge collection	95
6.3.1	Conversion gain	95
6.3.2	Sensitivity	97
6.3.3	Cross-talk	99
6.3.4	Pixel response non-uniformity	104
6.4	Noise	107
6.4.1	Temporal noise	107
6.4.2	Fixed pattern noise	108
6.4.3	Dark current	109
6.5	Comparison with standard sensor	113
6.6	Conclusions	113
7	Colour image reconstruction	115
7.1	Introduction	115
7.2	Colour matrixing	115
7.2.1	Method	116
7.2.2	Results	116
7.2.3	The problem of white balance	117
7.2.4	Impact of matrixing on signal-to-noise ratio	121
7.3	Reconstruction of images	124
7.3.1	Reconstruction method	124
7.3.2	Example reconstruction	127
7.4	Colour aliasing	128
7.5	Conclusion	132
8	Conclusion	134
8.1	Critical discussion of current approach	134
8.2	Improvements to project approach	135
8.3	Future work	137
8.3.1	Triple well double junction structure	137
8.3.2	Amorphous silicon structures	139
8.4	Final remarks	141
A	List of publications	142
	References	143

List of figures

1.1	Probable spectral sensitivity curves of the cones in the human eye. The coloured shaded regions represent the three best lights for additive tri-chromatic colour reproduction. Taken from Hunt's text.	2
1.2	Breakdown of a typical CMOS camera system.	4
1.3	An n by m two-dimensional array of pixels.	6
1.4	The RGB Bayer pattern CFA.	7
1.5	Spatial sampling of the green, blue, and red colours of the Bayer pattern.	8
1.6	Frequency domain representation of the Bayer pattern colour sampling. The area inside the dotted line represents spatial frequencies that can be imaged without aliasing.	8
1.7	Colour aliasing on a striped white shirt. The cyan and orange contours are caused by the limited resolution of the Bayer patterned image sensor. (Courtesy of STMicroelectronics).	9
1.8	Block diagram of a typical colour image reconstruction process.	12
1.9	Two colour selective pixels combined with magenta and green checkers (cross-section).	14
1.10	A two-colour CFA using magenta and green.	15
1.11	Spatial frequency domain representation of magenta and green pixel sampling.	15
1.12	The combination of a two-colour detector with magenta and green filters produces 4 responses.	16
2.1	Absorption depth in silicon vs. photon energy.	21
2.2	Representative cross section of an n^+/p diode.	22
2.3	Triple junction structure using selective epitaxial growth.	25
2.4	(a) Triple junction structure implemented in a triple well CMOS process and (b) equivalent circuit.	26
2.5	Triple junction structure responses (a) from Bartek et. al. (1)-(3) top, middle and bottom junction responses respectively and (b) from Chouikha et al. \diamond : top junction, \circ : middle, Δ : bottom, — : simulation.	27
2.6	(a) Double junction structure implemented in a CMOS process and (b) equivalent circuit.	28
2.7	Colour sensing structure employing depletion width modulation after Wolffenbuttel.	29
2.8	Amorphous colour sensing structure employing depletion width modulation after Sommer.	31
2.9	Three layer colour detector after Knipp. (a) pin-nip-pin circuit (b) 3 layer photo-detector structure (c) pinip-pinip-pinip equivalent circuit. Both circuits can be implemented by altering the layers in the structure.	32
2.10	Spectral responses of Knipp's (a) three- and (b) six- colour detector.	33
2.11	1-T pixel circuit.	36

2.12 3-T pixel circuit.	37
2.13 3-T pixel with cascode transistor to increase the conversion gain.	38
2.14 4-T pixel circuit.	39
2.15 Log pixel circuit.	41
3.1 Cross sectional view of the n^+/p_{well} photo-diode	47
3.2 Spectral response of the n^+/p_{well} photo-diode.	48
3.3 Photo-diode with 4 μm epilayer and heavily doped substrate.	49
3.4 Spectral response with varying epilayer thickness and substrate.	50
3.5 Potential profile vertically through the structure.	50
3.6 Simulated cross-talk of the standard pixel.	51
3.7 Doping profile of the defined DJ structure.	52
3.8 Simulated spectral response of the DJ structure.	53
3.9 Ratio of photo-current cross-talk between two DJ photo-diode structures.	53
3.10 Main effects on the $n_{well}/p_{substrate}$ peak response.	55
3.11 Main effects on the p^+/n_{well} peak response.	55
3.12 Contour plot showing variation in $n_{well}/p_{substrate}$ photo-current with varying epi doping and thickness. Fixed factors: P+ doping = $5e18\text{ cm}^{-3}$, P+ $X_j = 0.2\text{ }\mu\text{m}$, N-well $X_j = 2\text{ }\mu\text{m}$, N-well doping = $1e17\text{ cm}^{-3}$	56
3.13 Contour plot showing variation in p^+/n_{well} photo-current with varying N-well doping and junction depth. Fixed factors: P+ doping = $5e18\text{ cm}^{-3}$, P+ $X_j = 0.2\text{ }\mu\text{m}$, epi thickness = $7.5\text{ }\mu\text{m}$, epi doping = $5e15\text{ cm}^{-3}$	57
3.14 DJ response after optimisation.	58
4.1 Quantum efficiency measurement structure	61
4.2 Quantum efficiency measurement setup	62
4.3 Quantum efficiency of a standard n^+/p_{well} diode.	63
4.4 Quantum efficiency of a double junction structure implemented using P+/PLDD/N-well implants.	64
4.5 Quantum efficiency of a double junction structure implemented using P+/N-well implants.	65
4.6 Normalised quantum efficiency of the P+/N-well test diode.	65
4.7 Comparison of simulated and measured normalised quantum efficiency.	66
4.8 Normalised responses of the double junction structure implemented in 0.5 micron technology.	67
4.9 Normalised response with green and magenta filters.	67
4.10 Normalised response with cyan and yellow filters.	68
5.1 Six transistor active pixel circuit.	70
5.2 Operation of the six transistor active pixel circuit.	71
5.3 Eight transistor active pixel circuit.	73
5.4 Calculated SNR at 50% noise vs. photon flux for a 5 fF pixel.	78
5.5 Calculated SNR at 50% noise vs. pixel capacitance.	79

5.6	Calculated SNR at 50% noise vs. pixel generation. Starting with a 5f F pixel with 30% fill-factor and 800 nA cm^{-2} dark current, process improvements result in a 100 nA dark current, the microlenses are added to increase the light-collecting area to 70%. Next, a 4T pixel is used to eliminate kTC noise, and finally the voltage swing is doubled to 2V to improve peak SNR.	80
5.7	Calculated SNR at 50% noise for DJ and 3T cells. At some light levels the $n_{well}/p_{substrate}$ DJ SNR is very close to the absolute maximum possible at 6.8 microns due to its larger light collecting area and at all light levels is better than the standard 5fF 3T cell. Note the the 6.8 μm 3T and 9.6 μm DJ p^+/n_{well} curves are overlaid.	81
5.8	Layout of the 9.6 by 9.6 micron pixel	82
5.9	Maximum fill-factor vs. pixel pitch for the chosen 0.35 micron technology. The achieved fill-factor for 12.4, 9.6, 8.5 and 7.9 micron 6T pixels is also shown. A 3T active pixel naturally achieves a better fill factor as less transistors are required. The fill-factor of the 8T 12.4 micron cell is very poor.	83
5.10	Maximum active-area vs. pixel pitch for the chosen 0.35 micron technology. Four double junction pixels are also shown along with a 3T cell. It can be seen that the active areas of the 3T cell and the 9.6 micron double junction cell are comparable.	84
5.11	Layout of the 12.4 by 12.4 micron pixel.	85
5.12	Layout of the 8.5 by 8.5 micron pixel	86
5.13	Layout of the 7.9 by 7.9 micron pixel	86
5.14	Layout of the 8-T pixel.	87
5.15	Overview of DJ sensor architecture.	88
5.16	Schematic of the column and output stage structure.	89
5.17	Micro-graph of the image sensor.	91
6.1	Diagram of the signal chain of a camera system from incident photons to digital output.	92
6.2	Photon-transfer curve of an image sensor.	94
6.3	Measured photon transfer curve of the image sensor.	96
6.4	Sensitivity measurement setup.	98
6.5	Diagram showing dielectric stack and metal layers between microlens and photo-diode (not to scale).	100
6.6	Percentage cross-talk of P-plus outputs vs. illuminated pixel value under blue illumination.	101
6.7	Percentage cross-talk of P-plus outputs vs. illuminated pixel value under green illumination.	102
6.8	Percentage cross-talk of P-plus outputs vs. illuminated pixel value under red illumination.	102
6.9	Percentage cross-talk of N-well outputs vs. illuminated pixel value under blue illumination.	103
6.10	Percentage cross-talk of N-well outputs vs. illuminated pixel value under green illumination.	103

6.11	Percentage cross-talk of N-well outputs vs. illuminated pixel value under red illumination.	104
6.12	Diagram showing percentage cross-talk to adjacent pixels for the two pixel outputs for blue, green, and red illumination.	105
6.13	Standard deviation of the two pixel outputs vs. image mean as illumination is increased.	105
6.14	An example frame of image noise after frame subtraction.	107
6.15	Differential vertical FPN for the N-outputs.	109
6.16	Differential vertical FPN for the P-outputs.	110
6.17	Histogram of dark current at 25 degrees C.	111
6.18	Histogram of dark current at 45 degrees C.	112
6.19	Histogram of dark current at 65 degrees C.	112
7.1	Error vectors for the cyan/yellow filter combination after matrixing.	118
7.2	Error vectors for the magenta/white filter combination after matrixing.	118
7.3	Error vectors for the magenta/green filter combination after matrixing.	119
7.4	Error vectors for a RGB sensor implemented in the same technology.	119
7.5	Reconstructed image of a white sheet of paper using the fitted colour matrix.	120
7.6	Reconstructed image of a white sheet of paper using the reduced sensitivity colour matrix.	121
7.7	Error vectors for the matrix trained over a set of noisy samples.	122
7.8	Block diagram of the colour image reconstruction process.	124
7.9	Illustration of the sub-sampling step.	125
7.10	Illustration of the interpolation step.	126
7.11	Pixels used to create high pass filtered data.	127
7.12	Image reconstruction steps prior colour matrixing.	129
7.13	Image reconstruction steps to produce final colour image.	130
7.14	A chirp chart.	130
7.15	Image of a chirp chart taken with the double junction sensor without aperture correction.	131
7.16	Image of a chirp chart taken with the double junction sensor with aperture correction.	131
7.17	Image of a chirp chart taken with a Bayer patterned sensor.	132
7.18	Example image: the Macbeth colour chart.	133
7.19	Example image: toys and caffeine (essential project ingredients).	133
7.20	Image of the Macbeth colour chart taken with a commercial digital stills camera.	133
8.1	Triple-well structure.	138
8.2	Triple-well double junction pixel.	138
8.3	Colour sensing pixels using amorphous silicon.	140

List of tables

2.1	Summary of colour sensing elements	34
2.2	Summary of pixel circuits	43
3.1	Control factors in the DJ experiment	54
6.1	Sensitivity measurement results.	98
6.2	Summary of dark current measurements.	111
6.3	Comparison between double junction and standard sensor performance.	114
7.1	Summary of fit of colour output to RGB targets with various filter combinations (table shows RMS errors in RGB space)	117
7.2	Noise after colour matrixing for each colour channel with various filter combinations.	123

Acronyms and abbreviations

a-Si	amorphous-Silicon
CCD	Charge-Coupled Device
CCF	Central composite face-centered
CFA	Colour Filter Array
CMOS	Complementary Metal Oxide Semiconductor
CRT	Cathode Ray Tube
DJ	Double Junction
FPN	Fixed Pattern Noise
IR	Infra-Red
JFET	Junction Field Effect Transistor
LED	Light emitting diode
LVS	Layout-Versus-Schematic
MTF	Modulation transfer function
NLDD	N-type lightly doped drain
PLDD	P-type lightly doped drain
QE	Quantum Efficiency
RMS	Root-Mean-Square
SNR	Signal-to-Noise-Ratio
TCO	Transparent Conducting Oxide

Chapter 1

Introduction

1.1 Image sensors

Image sensors have become a familiar part of our everyday lives. Television is everywhere, security and surveillance cameras are commonplace, digital still and video cameras are quite affordable, and the market for personal computer based imaging products is rapidly expanding. Emerging markets for image sensors include mobile video communications and other hand held devices. Such applications present huge challenges in terms of power consumption, miniaturisation, and integration of multiple functions within the camera module.

Until recently, the image sensor market has been dominated by the *charge-coupled device* (CCD) [1][2] which was first proposed in 1970 by Boyle and Smith [3] and quickly adopted by industry. CCDs are to be found in most imaging applications, from low quality PC or surveillance to very high resolution astronomical and spy satellites. This is now a very mature imaging technology.

However the CCD is not the only solid-state imaging technology. In the past few years image sensors implemented in CMOS manufacturing technology have begun to gain real market share. Perhaps ironically, MOS based imagers predate CCDs by several years [4], but at the time the large geometries of the manufacturing technology made the pixel size much larger than that achievable in CCDs, which soon surpassed MOS imagers in terms of resolution. Today, sub-micron CMOS technology has removed this disadvantage and CMOS imagers can compete in terms of pixel size, while the cost of the process development does not have to be born by the image sensor development alone. CMOS image sensors allow a higher level of integration than CCDs, as the technology allows standard CMOS analogue and digital circuitry to be implemented on the same device. Single chip video and television cameras are possible [5][6][7]. Standard cell libraries can be used, reducing development time. Low power, single low-voltage supply image sensors have been implemented, while the voltage supply requirements and power consumption of CCDs are much higher.

Charge-coupled devices benefit from their maturity — the optical sensitivity, dark current, and noise performance is still superior to that obtained from CMOS imagers. There is no fundamental reason why CMOS imagers cannot match the performance of CCDs with some optimisation of the optical and photo-sensing properties of the technology. While some might say that this sort of process optimisation reduces the advantage of using the CMOS process, the use of additional process steps is already common in the industry, for example to provide double polysilicon capacitors or precision resistors for analogue CMOS circuits. The extra process modules are a small cost adder, but the underlying development of the advanced CMOS process is still funded by the wider electronics market. This view is reflected by the well known companies that have developed CMOS image sensors with specialised process variants.

1.2 Human vision

In order to understand how colour image sensors work one must first consider human vision.

The human eye contains two types of light sensing elements, called rods and cones. The rods are used at low light levels (e.g. moonlight) and provide colour-less vision. At higher light levels, the cones are used. Three different pigments are split between the cones which is thought to result in the three separate spectral responses of the eye shown in Figure 1.1. These responses have been obtained from a mixture of experimental observation using indirect measurements and genetically engineered cultures containing the pigments [8].

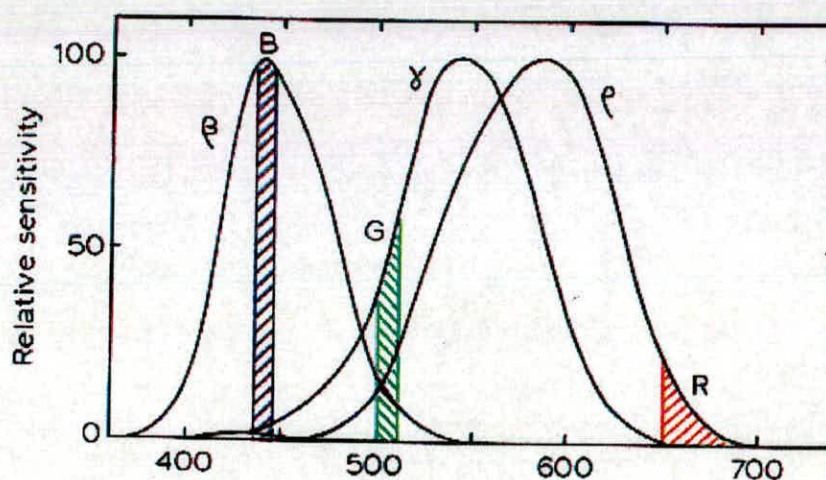


Figure 1.1: Probable spectral sensitivity curves of the cones in the human eye. The coloured shaded regions represent the three best lights for additive trichromatic colour reproduction. Taken from Hunt's text.

The three responses of the eye allow the use of *tri-chromatic* colour reproduction systems where 3 discrete stimuli are added together in the correct amounts to give the impression of a given colour. This was first demonstrated by Maxwell in the nineteenth century when he used three projectors, one red, one green, and one blue, overlaid exactly to produce a colour image. A more robust and detailed description of the tri-chromatic colour theory is beyond the scope of this thesis. An excellent introduction to colour reproduction and theory may be obtained in Hunt's '*The Reproduction of Colour*' [9].

One can imagine that an image sensor with exactly the same spectral responses as the human eye would therefore have the same colour discriminating capabilities. However, it is impossible to stimulate the eye with three discrete sources and correctly reproduce all colours. It can be seen in Figure 1.1 that considerable overlap exists between the three response curves, which means that it is impossible to stimulate the central curve without also stimulating one of the others. Many colours *can* be correctly reproduced by a suitable adjustment to stimuli of the other two curves, but this cannot be done for all colours. Hence, the tri-chromatic approach suffers from a fundamental limitation due to the nature of human vision itself. The situation is made worse by the fact that wider tri-stimuli are generally used than those shown in Figure 1.1 to increase brightness.

However, there is a further complication in colour reproduction, which is introduced by human physiology and psychology, and the tendency of the human brain to perform colour correction. In colour reproduction, it is therefore sometimes important to ensure the correct reproduction of subjectively important colours such as whites, grays or flesh colours, as these are more noticeable to the viewer if wrong. It may also be desirable to enhance the saturation of certain colours to produce a more subjectively pleasing image — depending on the target audience.

1.3 Camera systems

1.3.1 Breakdown

A camera system can be broken down into three sections:

1. The incident light from the scene to be recorded must be focused onto the image sensing elements using *optics*. In high-end applications, the scene can be focused using a lens and then split into three spectrally separated beams using a set of prisms. Three separate

image sensors (usually CCDs) are then used to record each colour channel of the image. More commonly, in lower cost cameras the scene is focused through a lens onto a mosaic patterned image sensor.

2. The image sensor (or sensors) converts the light after the optical system into an electrical signal which is then output to the next stage of the system.
3. The signals from the image sensor stage are then processed into the format required for the display. A storage stage may be involved between the sensor and this stage.

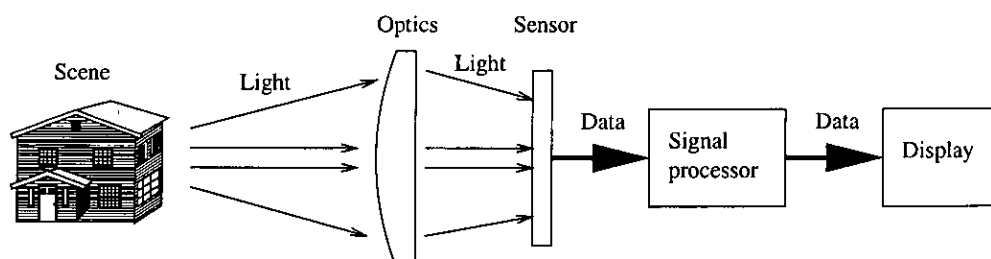


Figure 1.2: Breakdown of a typical CMOS camera system.

1.3.2 Optics

The optics can play a crucial part in the overall performance of camera system.

- At the simplest level, there exists a trade-off between the depth of field and the amount of light let through by the lens. This fraction of light F_{lens} allowed through is given by:

$$F_{lens} = \left(\frac{1}{f_{number}} \right)^2 \quad (1.1)$$

where f_{number} is the ratio of the aperture size to the focal length of the lens. A large f_{number} increases the depth of field which is desirable to improve the focus of the image. However, as image sensors work best with more light, some compromise must be made.

- At each *air/glass boundary* there is a refractive index mismatch which caused some proportion of the light to be reflected back. This reflected proportion of light R is given, for the simple case of normal incidence onto the surface, by:

$$R = \left(\frac{n_t - n_i}{n_t + n_i} \right)^2 \quad (1.2)$$

where n_t and n_i are the refractive indices of the two materials. For air/glass this means that 4% of the light will be reflected. For complicated optics many such surfaces may be present and the cumulative losses will be quite large. The use of anti-reflective coatings can reduce these losses but increases the manufacturing costs.

- The optics can also introduce significant distortions into the focused image due to spherical aberrations and vignetting, especially if a low cost lens is used. The lens will also have a low-pass spatial response, which limits the maximum resolution and minimum pixel sizes that can be used.

A review of the basics of lens systems can be found in most texts dealing with optics (e.g. [10]). In the end, the ultimate limit on resolution in image sensor systems may be lens technology. In this case, new approaches may be needed to improve resolution – for example by extracting more information from each detector element in the sensor.

1.3.3 Image sensor

1.3.3.1 Pixel array

Traditionally in lower cost systems a single image sensor has been used for colour imaging. CMOS sensors are often used in such lower cost systems. In this case, a two dimensional array of photo-diodes (or photo-gates) are used to detect light. Address and read out transistors are combined with the photo-diodes to allow the signal from each photo-diode to be sensed and converted to a suitable output signal. Each individual cell consisting of a photo-diode and its associated transistors is termed a *pixel*. Figure 1.3 shows a representation of how such pixels are usually connecting in an image sensing array.

In general, increasing the number of pixels will improve the resulting image, providing the performance of each individual pixel does not get worse at the same time. However, a larger array size, as well as taking more silicon area, increases the speed required of the read-out electronics and may therefore impact on other aspects of sensor performance, such as power consumption and noise performance.

Typical array sizes employed in image sensors cover a wide range, from low resolution QCIF (176×144), through CIF (352×288) and VGA (640×480), to much higher resolutions used in high definition TV and digital stills cameras with several million pixels.

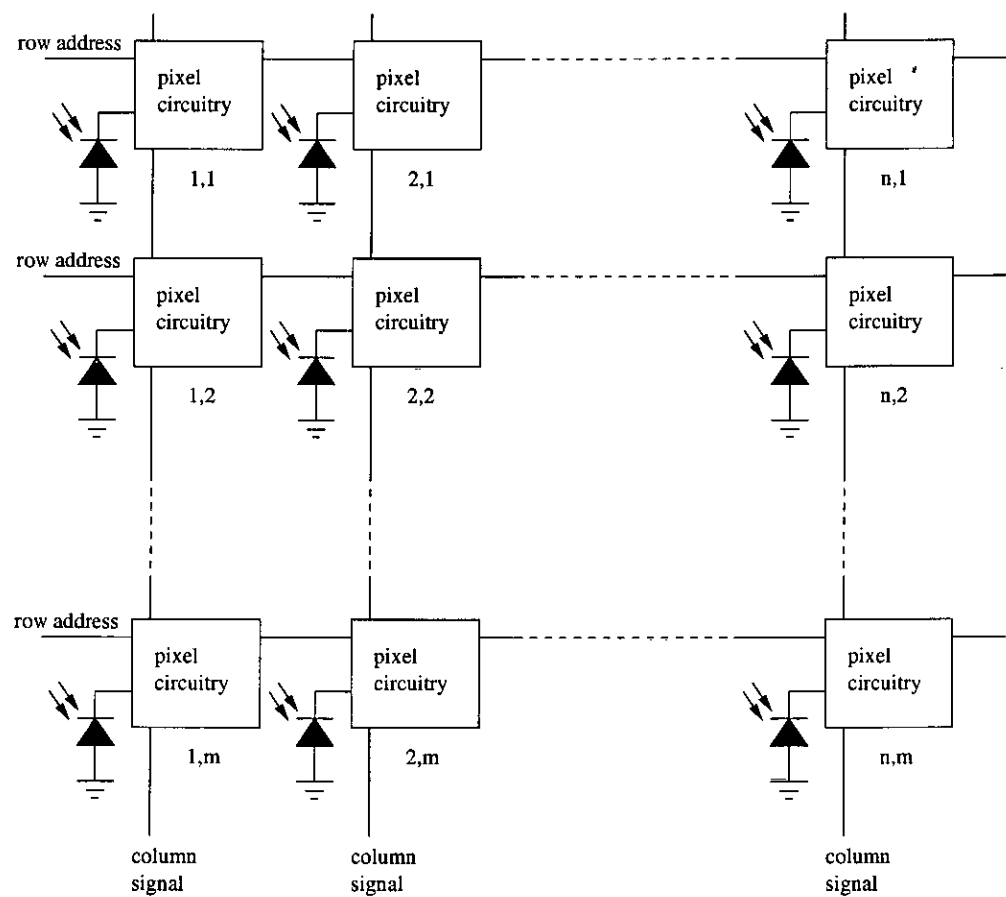


Figure 1.3: An n by m two-dimensional array of pixels.

1.3.3.2 Colour filter array

For colour imaging, the two-dimensional pixel array is combined with an overlaid mosaic pattern of colour filters to sense colour information. Such a mosaic pattern is usually termed a *colour filter array* (CFA). Various colour filter arrays have been proposed and used in solid-state image sensors. One of the more commonly used CFAs, the *Bayer pattern* [11][12] is shown in Figure 1.4. Other patterns such as RGB stripes, or complementary coloured checker-board patterns are also widely used [13]. In the Bayer CFA, twice as many pixels are dedicated to detecting green than either red or blue. This is justified by the greater acuity of the human eye towards detail contained in the green part of the spectrum. The green channel is used to generate the image detail (or *luminance*) data for the image.

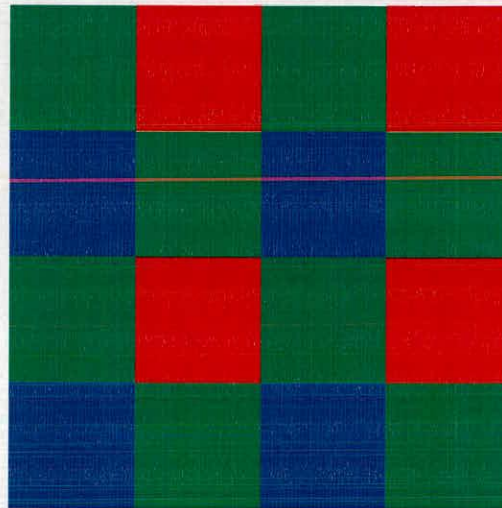


Figure 1.4: The RGB Bayer pattern CFA.

While the extra samples of the green information of the image is advantageous for estimating the luminance data, it creates problems for estimating the colour (or *chrominance*) information. One can consider a pixel array as a two-dimensional sampled data system. In this case, the sampling takes place in both the temporal and spatial domains. The spatial sampling of each pixel can be approximated by an impulse at the pixel centre (Fig 1.5). In the spatial frequency domain, these impulses are represented by a grid of impulses in multiples of $1/d_{pix}$, where d_{pix} is the pitch of the pixels of a certain colour. Such a frequency domain representation is shown in Figure 1.6, where ξ and η represent frequencies in the x and y image dimensions respectively.

Like all sampled data systems, image sensors are subject to *aliasing*. In the figure, the maximum frequencies that can be resolved without aliasing are contained within the dotted lines.

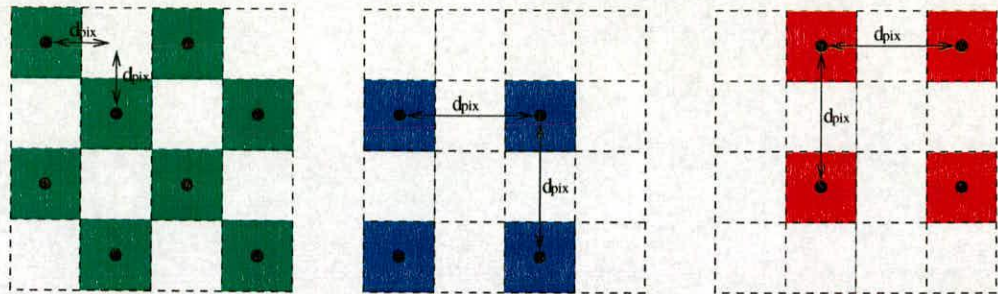


Figure 1.5: Spatial sampling of the green, blue, and red colours of the Bayer pattern.

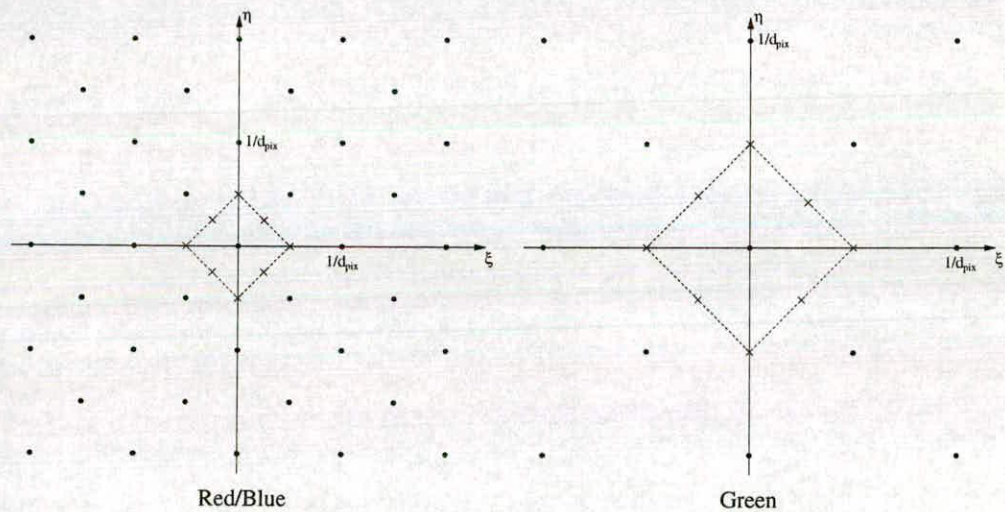


Figure 1.6: Frequency domain representation of the Bayer pattern colour sampling. The area inside the dotted line represents spatial frequencies that can be imaged without aliasing.

With the blue and red channels in the Bayer pattern, aliasing will start to occur at half the frequency of that it would in the green channel. Such aliasing is particularly noticeable along edges or stripes in images, and is quite offensive to the eye. It is often referred to as *moiré* in the literature. Figure 1.7 shows the result of such aliasing in a Bayer patterned sensor. The shirt is actually white with dark pin-stripes, but the stripes are aliased down to lower frequencies which appear as cyan and orange contours in the image. Such an effect is clearly noticeable and undesirable.



Figure 1.7: *Colour aliasing on a striped white shirt. The cyan and orange contours are caused by the limited resolution of the Bayer patterned image sensor. (Courtesy of STMicroelectronics).*

Conventional measures to reduce such aliasing effects involve the use of an optical anti-alias filter in front of the sensor to ensure that only spatial frequencies below the Nyquist limit are incident on the sensor. However, such a filter can add considerable cost. An alternative approach is to use digital signal processing techniques to mask the effects of aliasing [14]. Such an approach can reduce the apparent artifacts of the aliasing, but does not eliminate them completely or increase the level of detail in images that can be correctly resolved. It also requires extra digital circuitry to implement the processing.

1.3.3.3 Image sensor performance metrics

Modern CMOS image sensors are highly integrated mixed-signal systems. Many different trade-offs exist between, cost, power consumption, and performance. In data sheets and technical papers a number of parameters are used to describe image sensor performance:

S/N or dynamic range: the ratio of the saturation signal to the noise floor measured at zero exposure. This is effectively the dynamic range of the sensor in a single scene. A camera may have a larger inter-scene dynamic range as the exposure time can be adjusted for different illumination levels.

Peak SNR: this is peak signal-to-noise ratio at saturation. This is not the same as S/N as it includes signal dependent noise (i.e. photon shot noise) and dark current noise. Often this is quoted without the fixed pattern noise (FPN) of the sensor — only temporal noise sources are included. The justification for this is that FPN can be cancelled whereas there is no way to cancel the sensor temporal noise.

Sensitivity: This is the output voltage level of the sensor as a function of light intensity. It is usually quoted in $Vlux^{-1}s^{-1}$. However, the unit of lux does not define the spectral content of the light (it is the input spectrum normalised for the human eye response) therefore this sensitivity measurement cannot be used to predict the response to a specific colour or wavelength.

Quantum efficiency (QE): a more physics based measure of the sensor conversion from light to charge is the *quantum efficiency*. It is simply the number of electrons collected by the sensor divided by the number of incident photons. It is a function of the photon wavelength and thus this parameter should be given whenever QE is quoted.

Dark current: the pixel leakage current mean value. Usually quoted in $pAcm^{-2}$. Note that this does not give any information about the spread of dark current across the array which contributes FPN.

Conversion gain: the sensor converts photo-generated electrons into a voltage (usually within the pixel). The number of volts obtained *per* electron is the *conversion gain*. It is usually quoted in $\mu V/e^-$.

Fixed pattern noise (FPN): the fixed offsets due to the readout and pixel electronics. It is usually expressed as a percentage of the full scale or in mV . As dark current FPN is exposure

dependent it may not be included in this metric. Also, the vertical (column) and other FPN noise sources are often separated.

Resolution: the level of detail that can be obtained from an image sensor depends on the number of pixels. More pixels improves the sampling of the image and hence the maximum spatial frequencies that can be resolved without aliasing according to the Nyquist criterion.

Modulation transfer function (MTF): is the amplitude response of the imaging array to a given spatial input frequency. Generally, imaging arrays have a low-pass spatial response — the amplitude of higher spatial frequencies is attenuated due to the spatial averaging within each pixel.

Frame rate: is the maximum number of full images that can be obtained from the sensor in 1s. Often, this is limited by the speed of the readout electronics, but also the sensitivity and QE of the pixels determines the minimum exposure that can be used to obtain a reasonable SNR at a given light level.

Power consumption: is increasingly important for CMOS image sensors — especially those intended for the mobile imaging market.

Often, in data sheets or published papers, the image sensor performance specifications are vague and incomplete, which makes comparison between competing devices very difficult.

1.3.4 Signal processing

The output of the image sensor is usually digital data. To recover a complete image from the CFA patterned data and convert it to the correct form for a display it is necessary to apply signal processing [15][16].

Each block in the signal processing chain is briefly explained in the following sections.

1.3.4.1 Interpolation

The first step in the image reconstruction process is to ‘fill in’ the missing values for each pixel. Thus for each green pixel in the Bayer pattern for example, interpolated blue and red values are added. After interpolation, triplets of RGB data exist for all the pixels in the array.

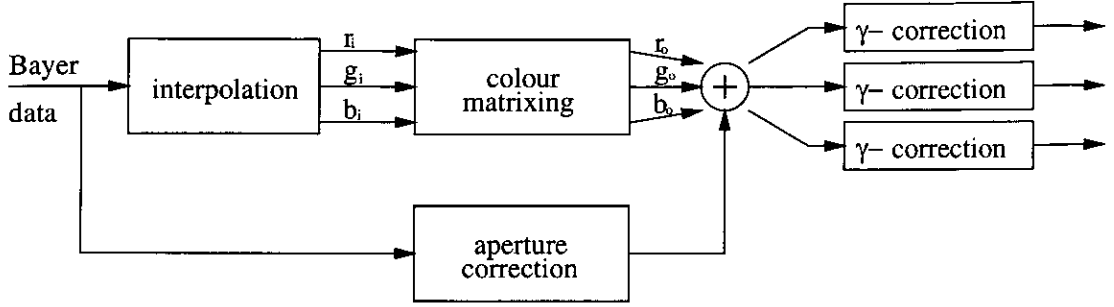


Figure 1.8: Block diagram of a typical colour image reconstruction process.

As these extra values are interpolated they are at best approximate. Their accuracy will depend on the method used and the amount of high-frequency detail in the image [17]. It has been reported in the literature that higher order interpolation algorithms generally produce more pleasing results [13][18][19].

1.3.4.2 Matrixing

The colour data from the RGB patterned image sensor is usually not suitable for direct display. This is because the colour filters themselves do not match the tri-chromatic stimuli of the display. One can consider the colour data of each pixel as a point in a three-dimensional colour space. To produce acceptable colour, a linear transformation is performed to map those coordinates onto their equivalent point in the colour space of the display [15][20][2]. Such a transformation is often referred to as *matrixing* as it can be conveniently represented by matrix algebra:

$$\begin{pmatrix} r_o \\ g_o \\ b_o \end{pmatrix} = \begin{pmatrix} m_{11} & m_{21} & m_{31} \\ m_{12} & m_{22} & m_{32} \\ m_{13} & m_{23} & m_{33} \end{pmatrix} \begin{pmatrix} r_i - r_{offset} \\ g_i - g_{offset} \\ b_i - b_{offset} \end{pmatrix} \quad (1.3)$$

The coefficients in the 3×3 matrix and the offsets can be determined by fitting to experimental data from a known set of colours. Usually, a minimum mean-squared error (least squares) method is used to do the fitting.

A problem with the colour matrixing approach is that it often significantly decreases the signal-to-noise ratio of the image. This is because the three inputs to the matrixing stage originally all come from different pixels and hence contain uncorrelated noise. Thus, the matrixing process

will add noise to the output values in an RMS manner wherever non-diagonal matrix coefficients are present.

1.3.4.3 Aperture correction

Aperture correction is used to compensate for the loss of high-frequency information that occurs during the interpolation stage, and also due to the roll-off in system MTF at higher spatial frequencies [21]. With Bayer data, it is often accomplished by adding a high-pass filtered (edge enhanced) version of the green-channel data to final image. The reader will recall that the Bayer pattern contains twice as many green pixels precisely to aid the estimation of the luminance part of the image. This improves the reproduction of fine detail in the image, providing that detail is not on highly saturated red or blue objects.

1.3.4.4 Gamma correction

The voltage-to-intensity transfer function of a cathode-ray-tube display (CRT) is non-linear. Thus, the image data must be adjusted prior to display to compensate for this transfer function [21]:

$$L_{display} = K(V_{drive})^\gamma \quad (1.4)$$

where $L_{display}$ is the luminance output of the CRT, K is a constant scaling factor, and γ is the exponent relating voltage to luminosity. During gamma correction, the data should be put the power of $1/\gamma$ to give the same relative image intensity on the display as in the original scene. However, often a different value of $1/\gamma$ is used to produce a more pleasing image, for example by increasing the contrast to reduce the intensity of darker parts of the image where the SNR is lower — making the noise less noticeable.

If the data is being captured by a computer, gamma correction is usually performed by the computer itself, and thus can be omitted from the camera's signal processing chain.

1.4 This project

Many other colour filter arrays for image sensors have been proposed — mainly those employing complementary colour filters. All have used at least three colours, and often more than three. If less colours are used in a checker-board pattern, it improves the spatial sampling of each of those colours. However, in section 1.2 it was stated that a minimum of three spectral responses are required for colour imaging. One may therefore ask: *‘is it possible to have less than three filter colours in an image sensor without invalidating the tri-chromatic colour theory?’* As can be seen throughout the remainder of this thesis, the answer to this question is ‘yes’.

In this project, a two colour CFA is used which splits the spectral content of the scene into two. This is not enough to achieve colour imaging — at least three responses are required. As will be described in this thesis, it is possible to use special photo-diode structures, with junctions vertically stacked above one another, to obtain multiple spectral responses from a single pixel. If pixels using such a structure are combined with a two-colour CFA (Fig. 1.9), 4 responses will be obtained which is sufficient for imaging.

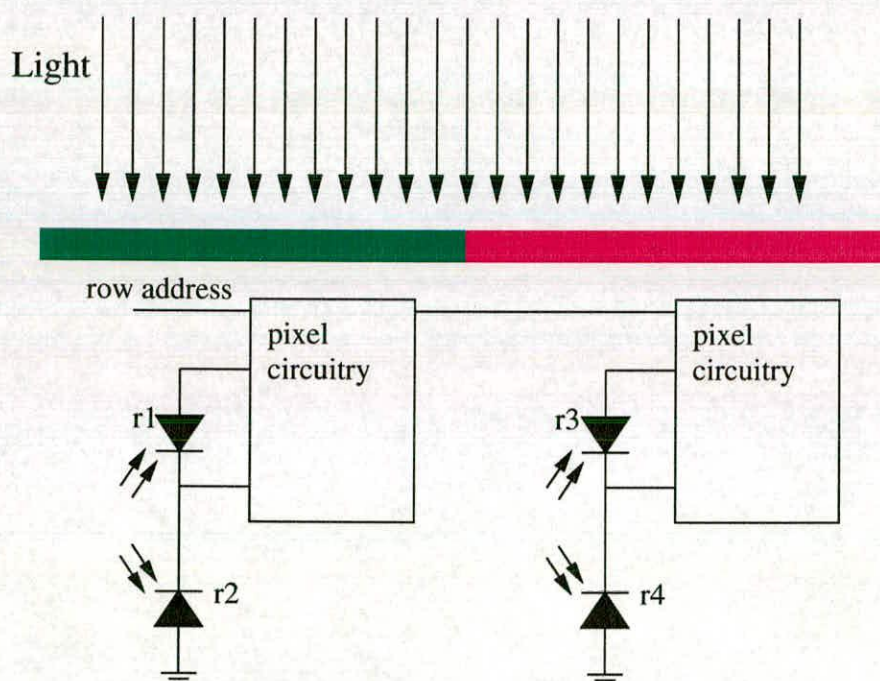


Figure 1.9: Two colour selective pixels combined with magenta and green checkers (cross-section).

1.4.1 A two-colour CFA

Consider the CFA shown below in Figure 1.10. The spatial sampling of the green and magenta checkers is equal in both the x- and y- dimensions. This is different from the standard Bayer pattern, as there are equal numbers of each filter colour.

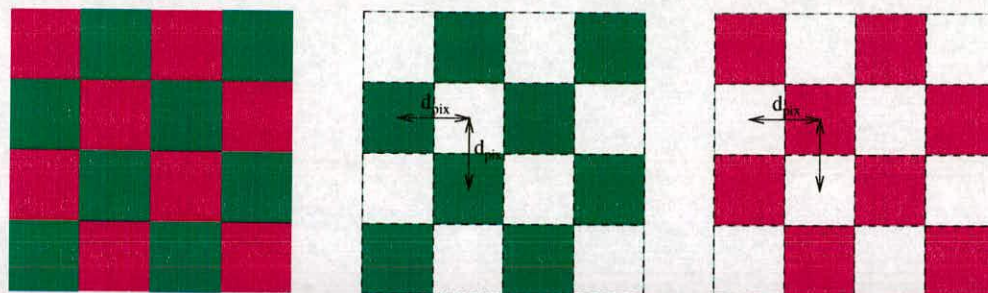


Figure 1.10: A two-colour CFA using magenta and green.

In the example given above magenta is used as a filter colour to allow both red and blue coloured light through to the pixel underneath. If the pixel has a means of discriminating between red and blue light then full-colour imaging will still be possible. Thus, the Nyquist limit on the spatial frequencies in the red and blue part of the spectrum will be the same as that for green (Fig. 1.11).

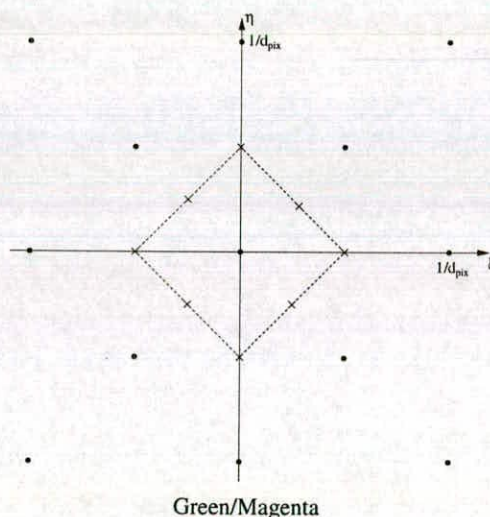


Figure 1.11: Spatial frequency domain representation of magenta and green pixel sampling.

It should be noted that the CFA colours do not have to be magenta and green, any set of filters that produces at least 3 responses when combined with the pixel underneath should be sufficient for imaging provided the whole visible spectrum is adequately covered.

1.4.2 A two-colour pixel

A requirement when using the CFA introduced in section 1.4.1 is that the pixel also has the ability to distinguish between blue and red light — or more correctly has two linearly independent responses. Chapter 2 reviews solid-state devices which have this property.

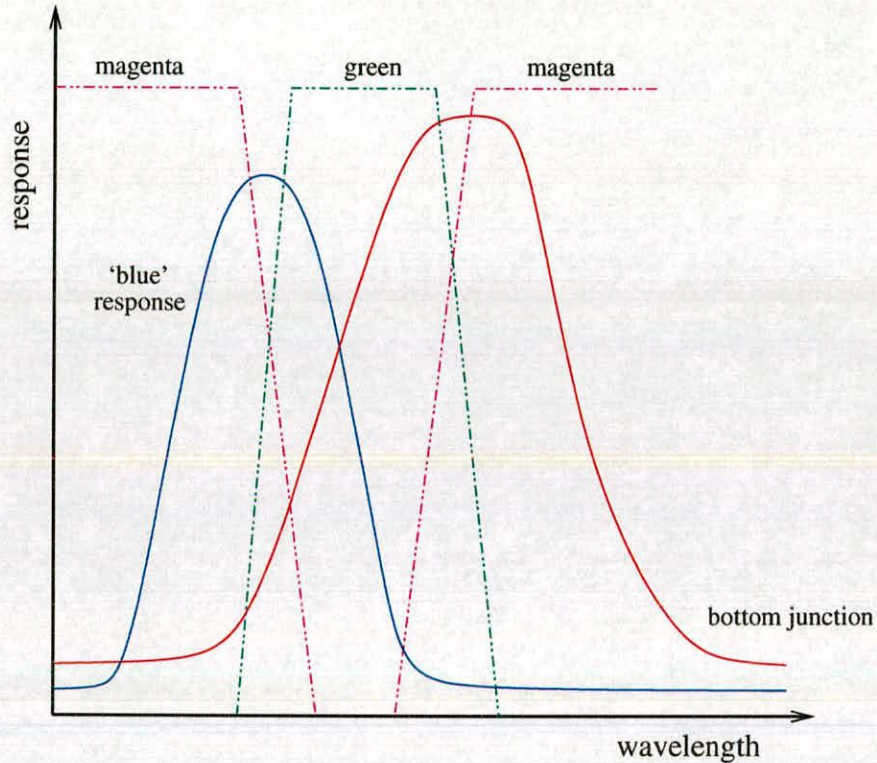


Figure 1.12: *The combination of a two-colour detector with magenta and green filters produces 4 responses.*

Figure 1.12 shows pictorially the combination of a two-colour detector (pixel) with magenta and green filters. This results in 4 colour responses from 2 pixels, and all responses sampled equally in the spatial domain. As four spectral responses are available, more accurate colour reproduction may be achieved with reduced aliasing in the blue and red signals.

1.4.3 Possible benefits and disadvantages

The possible benefits of this approach are:

Equal spatial sampling. In the 2-colour CFA, all colours are sampled at the same spatial frequencies. This should increase the spatial frequencies that can be resolved, relative to the Bayer pattern, and thus reduce the moiré effects.

Colour accuracy. With 4 responses instead of three, there is more information with which to estimate the RGB colour output of the camera during matrixing. This could improve the colour reproduction in the resulting image.

Smaller arrays. By vertically integrating the colour selectivity, smaller arrays for a given resolution may be possible.

On the other hand, there is one major disadvantage. As there are two colour responses in each pixel, more complicated pixel circuitry will be required. This may increase the pixel size (and therefore the total size of the image sensor) and degrade the signal dynamic range and noise performance.

1.5 Project aims

This thesis describes the design and evaluation of an image sensor, in CMOS technology, with the following novel properties:

Two-response photo-diode: a non-standard photo-diode structure is employed which provides two linearly independent responses.

Active-pixel circuitry: Specially designed pixel circuitry is investigated and implemented to allow such a photo-diode structure to be used.

Colour imaging from a 2-colour CFA: Finally the colour image reconstruction is implemented in software from data acquired using two suitably coloured filters.

The general aim of the project is to evaluate the impact of such an approach to the performance of the image sensor, with particular consideration to the following:

Colour accuracy: does the availability of four spectral responses aid in accurately determining the image colours?

Colour aliasing: is colour aliasing in the spatial domain reduced? As the two-colour photo-diode will require more circuitry, it may not be possible to implement a compact pixel such that resolution is not lost overall.

Signal to noise ratio: The noise performance and sensitivity of the resulting sensor should remain competitive with standard approaches.

This project therefore concentrates on the trade-offs inherent in the pixel design itself as ultimately the pixel is the most important factor in the overall image sensor performance.

1.6 Methodologies

A variety of tools and methods were used in this project as it spans the full range of CMOS image sensor design, from the low-level photo-diode response to the high-level colour reconstruction process. The methods used included:

- Device simulation is employed to investigate photo-diode spectral responses as the process parameters are varied.
- Spectral measurements have been performed on test structures. Test equipment was provided through STMicroelectronics.
- A noise model for the pixel has been developed, and is used to evaluate the trade-offs between pixel size and performance.
- Standard analogue integrated circuit design techniques are then used to design a custom image sensor in a CMOS technology.
- Finally, software has been written to implement the colour reconstruction chain using data from the sensor.

1.7 Breakdown of thesis structure

The following chapters describe the background, theory, and results from the design of the image sensor:

Chapter 2: This chapter describes the relevant photo-diode structures and pixel circuitry for using in a multi-colour sensing pixel. The existing literature is reviewed and the advantages of the different approaches are compared.

Chapter 3 describes the device simulation of a two-colour detecting and standard photo-diode implemented in a CMOS process. It evaluates possible process modification that could be made to alter the spectral responses.

Chapter 4: This details spectral and quantum efficiency measurements made on specially fabricated test structures, and the colorimetric accuracy that is obtained with different colour filter configurations.

Chapter 5: The trade-offs between different pixel designs are evaluated by modelling the signal-to-noise ratio. This chapter also describes the design and layout of the pixel array and associated circuitry.

Chapter 6: Low-level results from the prototype image sensor such as SNR, cross-talk, and sensitivity are presented and compared with a standard sensor.

Chapter 7 describes the reconstruction of a colour image from the sensor in software and compares the high-level performance with an equivalent RGB sensor.

Chapter 8 presents the key findings and conclusion of this research. A critical discussion of the advantages and disadvantages of the new approach is given. This chapter also makes recommendations for future work.

Chapter 2

Background

2.1 Introduction

In this chapter, a survey is given of the physics, devices, and pixel circuits relevant to the design of a colour sensing active pixel in a CMOS technology. The physics provides an understanding of the trade-offs between choice of manufacturing technology, device design and complexity, as well as imaging performance. Previously published colour sensitive devices are reviewed. Obviously the device is of little use without an ability to access the results in an image sensor array, so several widely used active pixel circuits are also described.

2.2 Photo-diode physics

2.2.1 Spectral response and sensitivity

The spectral response and sensitivity of silicon photo-diodes has been extensively studied [22][23][24][25][26]. The factors determining the response at a given wavelength can be broadly divided into two:

1. Absorption, reflection and interference effects in the layers above the silicon.
2. Carrier generation and collection in the silicon itself.

In terms of spectral response and quantum efficiency, both can be dramatically affected by the thin film layers making up the dielectric stack above a device [27]. It is possible to make interference filters in this manner to select a given region of the spectrum, or to create anti-reflective coatings to improve the quantum efficiency.

Photon absorption in silicon depends on the photon energy. The variation in the photon flux density through the silicon is given by:

$$I_{opt}(\lambda, x) = I_0(\lambda)e^{-\alpha(\lambda)x} \quad (2.1)$$

where I_{opt} is the photon flux of wavelength λ at depth x , I_0 is the flux at wavelength λ at depth zero, and α is the wavelength (photon energy) dependent absorption co-efficient. Figure 2.1 shows how this co-efficient varies in silicon with photon energy [28][29][30][31].

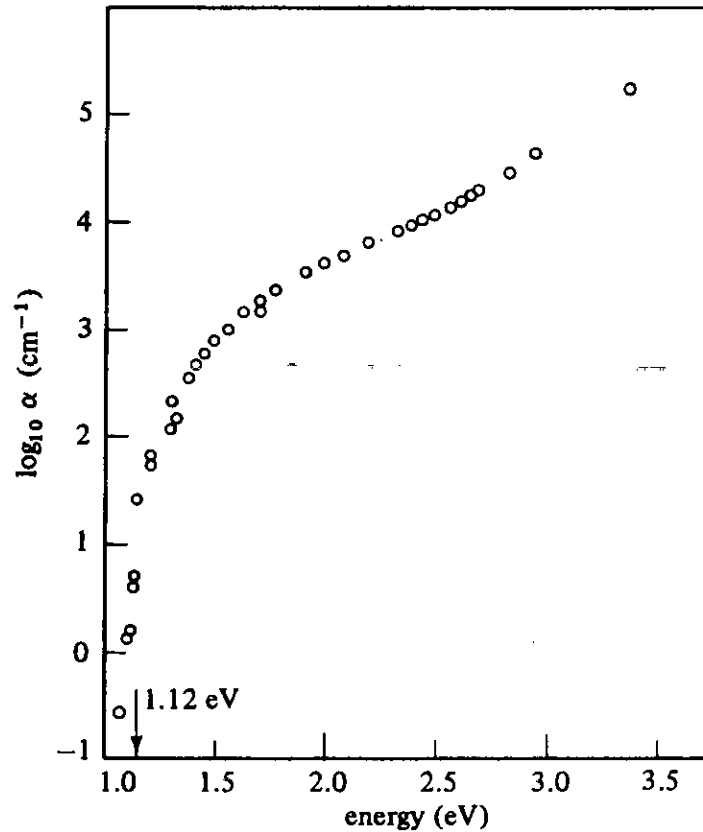


Figure 2.1: Absorption depth in silicon vs. photon energy.

The wavelength dependence of photon absorption in silicon is absolutely key to this work. Photo-current in a photo-diode is made up of two components, the drift current in the depletion region, and the diffusion current outside it [24]:

$$J_{tot} = J_{drift} + J_{diff} \quad (2.2)$$

In the depletion region, the carriers are driven apart by the field, and it is safe to neglect recombination. The drift current can therefore be expressed as [32]:

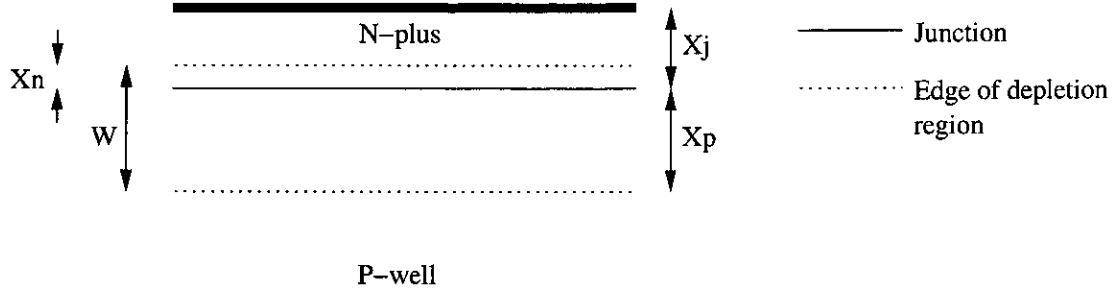


Figure 2.2: Representative cross section of an n^+/p diode.

$$J_{drift} = qI_0 e^{-\alpha(x_j - x_n)} (1 - e^{-\alpha W}) \quad (2.3)$$

If the n^+ region is heavily doped, then $x_n \ll x_p$ and $W = x_p$. Also, if the junction is shallow then $W \gg x_j$. We can simplify Eq. 2.3 as:

$$J_{drift} = qI_0 (1 - e^{-\alpha W}) \quad (2.4)$$

Outside the depletion region (either above or below) the current is caused by diffusion in which carrier mobility and lifetime are crucial. Making the same assumptions as for Eq.2.4 the diffusion current is dominated by the current in the P-well:

$$J_{diff} = qI_0 \frac{\alpha L_n}{1 + \alpha L_n} e^{-\alpha W} + qn_{n0} \frac{D_n}{L_n} \quad (2.5)$$

where L_n is the diffusion length of excess electrons in the P-well, D_n is the diffusion constant, and n_{n0} is the excess equilibrium electron density in the P-well.

If the assumptions above do not hold then the expression for the diffusion current is considerably more complicated [32]. In order to accurately predict device behaviour it is better to employ device simulation as is used in Chapter 3.

However, we can make the following general statements relating to photo-diode response:

- More heavily doped silicon has lower minority carrier lifetime. Photo-generated electron-hole pairs will travel less far in heavily doped regions before recombining. This means that within the bulk silicon, the photo-diode junction profile is highly significant.

- Thus, for example, a heavily doped region at the surface is likely to reduce the blue response but is unlikely to affect red photons. This is the situation when standard n^+/p CMOS diodes are employed as the photo-diode [23].

The depletion region is the most efficient collection region. In the work reported in this thesis this fact is exploited. By having two junctions at different depths in the silicon, two different spectral responses will be obtained due to the spectral dependence of the depth of the photo-generated carriers. Even carriers moving by diffusion are likely to be collected in the nearest depletion region which also contributes to the spectral selectivity.

2.2.2 Dark current

Even when there is no illumination, a reverse biased photo-diode still has a current through it. This current, referred to as *dark current* is thermally generated and has a strong temperature dependence [33]. Naturally, thermally generated carriers in the photo-diode are indistinguishable from those generated by light, so this current sets the lower limit on the photo-currents that can be detected.

Dark current is contributed from three regions:

1. Drift current due to thermal generation in the depletion region and also generation due to defects in the crystalline silicon.
2. Diffusion current due to carriers generated in the bulk silicon (the epi or well). This is both thermal and defect based generation.
3. Current due to generation at the surface (known as surface states) due to process induced defects.

Ion implantation and oxide growth can introduce defects into the silicon at both the surface and to a lesser extent in the bulk. Thus the dark current contribution due to surface states is highly dependent on the manufacturing process. Annealing and modifications to oxidation processes can significantly reduce dark current [34]. The dark current also varies over the array — different pixels will not have the same leakage current. As is discussed in Section 5.3, this introduces a fixed pattern noise into the image. Therefore, not just the mean, but also the variance of the dark current over the array should be minimised.

2.3 Solid-state colour sensors

There are many applications that require accurate and automatic measurement of colour in a short time and this has driven the development of integrated colour sensors. Many sensors have employed a 3-colour filter approach to obtain three independent responses covering the spectrum of interest. This type of sensor will not be described here. An alternative approach is to exploit material properties to produce three or more spectral responses, or to determine the wavelength of incident monochromatic light. This is more relevant to this work (see Section 1.5), as such a sensor eliminates the need for 3-colour filters.

2.3.1 Bulk silicon

2.3.1.1 Single junction

It is possible to vary the spectral response of a single junction photo-diode to a limited degree. This can be done in several ways:

1. By varying ion implantation energies the junction depth can be made deeper or shallower. This alters the depth of the depletion region which is the most efficient collection area for photo-generated charge.
2. In a similar way, changing the doping levels around the junction will vary the depletion region width.
3. Introducing a heavily doped region, either above or below the junction, will reduce the minority carrier lifetime and diffusion length. This means that it will be unlikely that carriers generated in this region will be collected by the photo-diode.

The effect of these changes on photo-diode spectral response is investigated using device simulation in chapter 3. It is also possible to vary the spectral response of a single junction by varying the bias voltage across it as detailed in section 2.3.2.

2.3.1.2 Triple junction structures

One of the most obvious approaches to realise a colour sensing pixel in bulk silicon is simply to have three junctions on top of each other. This can be achieved with a large amount of

control over the doping and junction depths using selective epitaxial growth. Bartek [35] *et. al.* fabricated and measured, and Mohajerzadeh *et. al.* [36] used process and device simulation to model, the spectral response of such a structure.

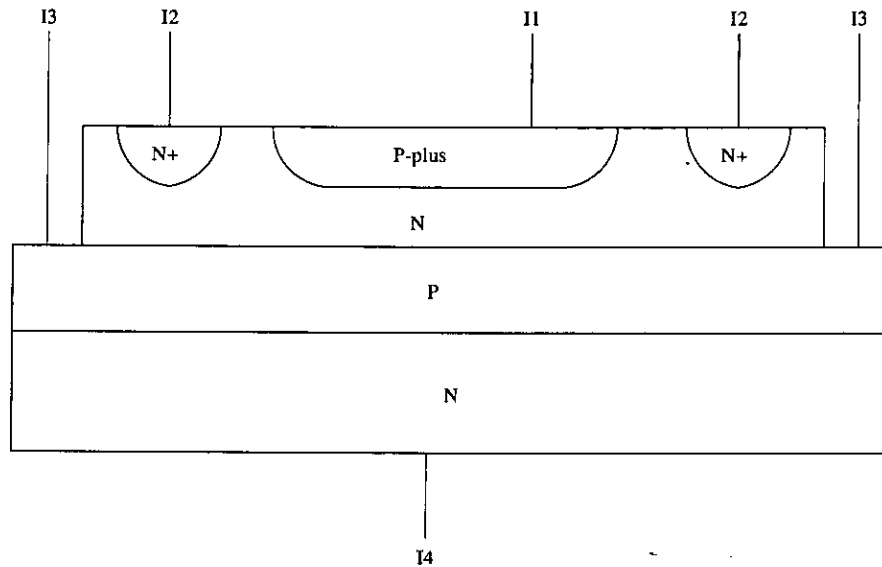


Figure 2.3: Triple junction structure using selective epitaxial growth.

In both cases, three independent spectral responses (photo-currents) were obtained. Mohajerzadah found that in his case a simple linear transformation was required to produce three curves representing RGB. Bartek's device was more complicated — extra lightly doped regions were introduced to tailor the depth of the depletion regions and enhance the spectral selectivity. This gave usable RGB curves. However, neither group presented colour matching information in terms of the CIE colour triangle, so it is hard to say whether good colour reproduction would be obtained.

Selective epitaxial growth is not normally employed in CMOS processes, so the devices above cannot be implemented easily in an image sensor. Recently, triple-well CMOS processes have become available. Normally the extra well is used for isolation purposes but it can be used to form a photo-diode. A possible way of implementing the three junction structure using standard implants in a triple-well process is shown in Figure 2.4. Despite the seeming simplicity of this idea, it was only recently patented for use in an image sensor (rather than a single colour sensor) [37] and it seems no actual working arrays or CMOS pixel results have been reported. Another group based in France has implemented and published results of a single triple junction structure implemented in a BiCMOS technology for use as a colour detector [38], and another group in a CMOS/CCD technology [39].

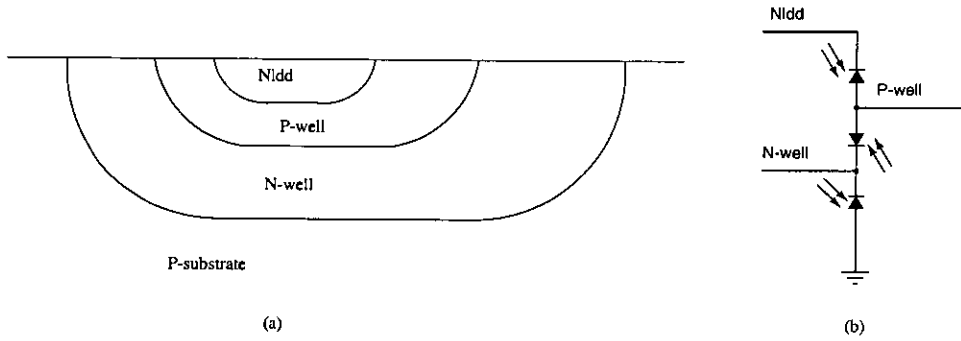


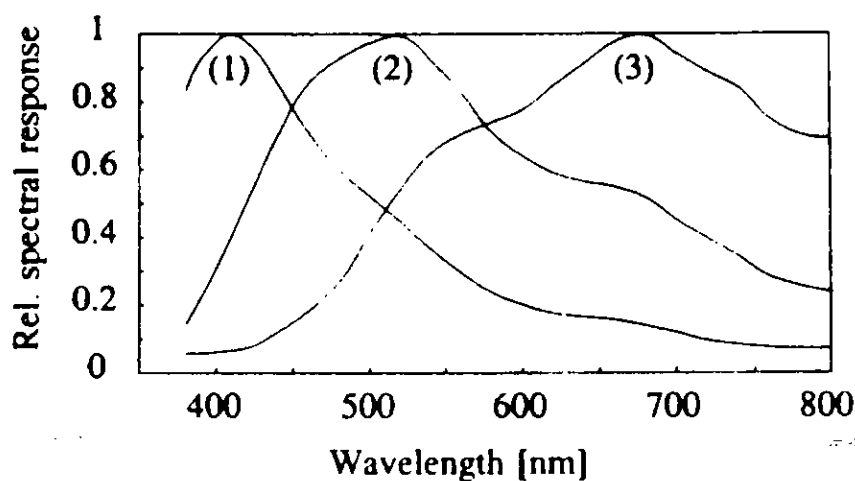
Figure 2.4: (a) Triple junction structure implemented in a triple well CMOS process and (b) equivalent circuit.

The three photo-junctions at different depths in the silicon will have linearly independent spectral responses, therefore a two dimensional array of such pixels should be sufficient for colour imaging. The pixel will certainly require more space due to the well spacings required to prevent punch-through and the extra transistors that will be needed for the pixel. During this project no triple-well process was available so it is not known whether this pixel will consume more or less area than 3 standard pixels. The light collecting area must be restricted to the area of the *Nlidd* region to ensure the spectral selectivity between the junctions. This will reduce the light collecting area, but the use of microlenses above the pixel may mitigate against this.

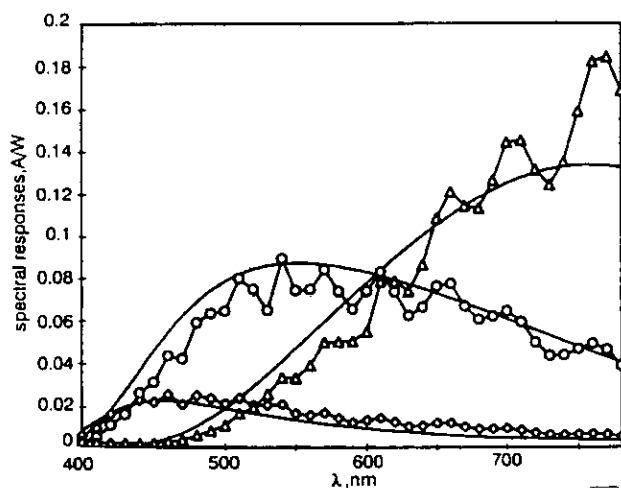
Unfortunately, it is very unlikely that an optimised set of spectral responses like Bartek's (Fig 2.5a) will be obtained from this pixel as the junction depths are optimised for CMOS device operation rather than optical response. This was certainly the case with the BiCMOS version of this structure (Fig 2.5b). Therefore one would expect a linear transformation would be required with large non-diagonal coefficients which will degrade the image sensor signal-to-noise ratio. Acceptable colorimetric accuracy could be obtained after a linear transformation was performed on the BiCMOS and CMOS/CCD structure responses.

2.3.1.3 Double junction structures

A double junction structure can be more easily integrated in a standard CMOS technology (Fig. 2.6) [40][41][42][43][44]. This device provides two spectral responses which are sufficient to resolve a single narrow-band colour but not for imaging. Once again, metal shielding is required to ensure that incident light travels only through the spectrally selective part of the structure.



(a)



(b)

Figure 2.5: Triple junction structure responses (a) from Bartek et. al. (1)-(3) top, middle and bottom junction responses respectively and (b) from Chouikha et al. \diamond : top junction, \circ : middle, \triangle : bottom, —: simulation.

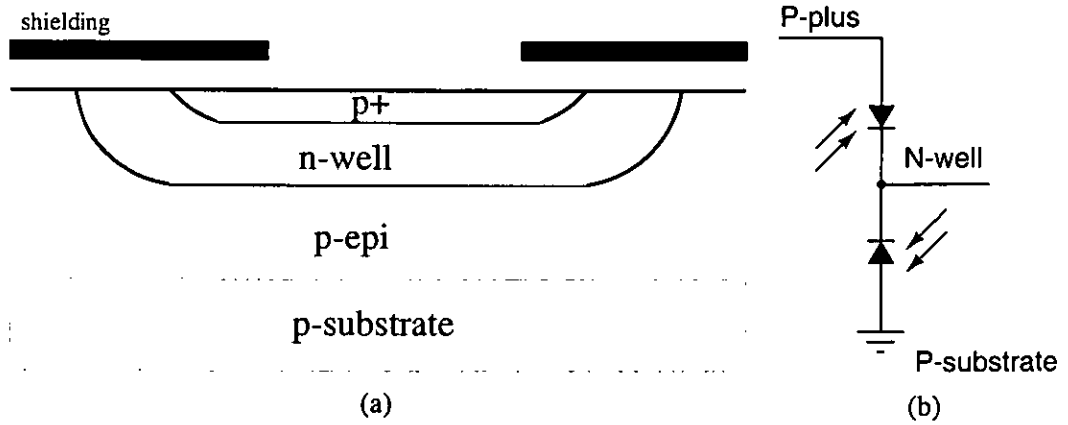


Figure 2.6: (a) Double junction structure implemented in a CMOS process and (b) equivalent circuit.

This structure has been employed with op-amp style integrating and logarithmic read out circuits to make a simple colour sensor for monochromatic light. In this application, the ratio of the photo-responses is used to determine the incident wavelength. To date, nobody has attempted to use this structure in an image sensor. In order to sense colours (rather than single wavelength) a method of obtaining a third spectral response is required. Simpson *et. al.* investigated the use of standard CMOS polysilicon and oxide layers to make a spectrally selective filter to provide more responses. It is also possible to add special interference filter layers above the structure to achieve many more responses [45].

2.3.2 Bias voltage based

The width of the space-charge region in a pn junction is a function of the applied bias voltage. For an abrupt pn junction this width is given by [46]:

$$x_d = \left(\frac{2\epsilon_s}{q} \left(\frac{1}{N_a} + \frac{1}{N_d} \right) (\phi_i - V_a) \right)^{1/2} \quad (2.6)$$

where ϵ_s is the permittivity of silicon, q is the electronic charge, N_a and N_d are the P and N doping levels, ϕ_i is the junction built in voltage, and V_a is the applied bias across the junction. By varying the bias across the junction V_a , the depth of the depletion region can be varied which changes the spectral response. A simple structure that uses this property is shown in Figure 2.7 [47].

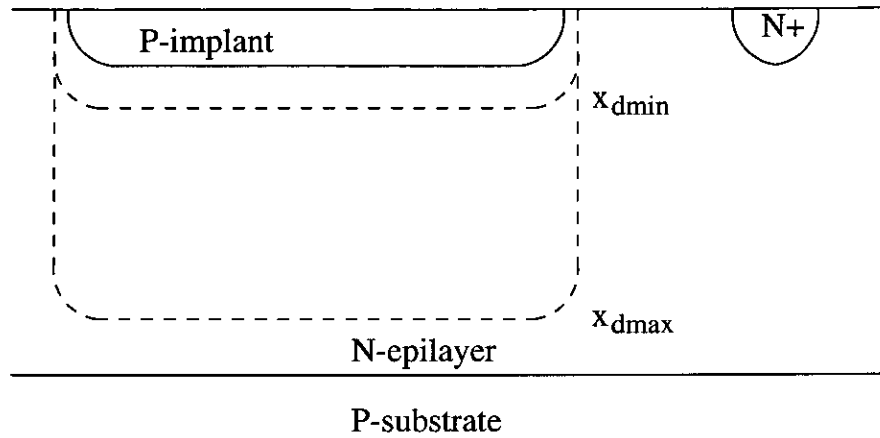


Figure 2.7: *Colour sensing structure employing depletion width modulation after Wolfenbuttel.*

The device operates in a similar manner to a JFET. The voltage on the the p^+ region is controlled to adjust the depletion width. A fact that may not be obvious from the figure is that the substrate potential is also controlled to minimise the diffusion current from photo-generated charge outside the depletion region. In this way the signal current from the sensor is collected solely from the space-charge region.

Wolfenbuttel has published several papers describing integrated colour sensors using this device [47][48][49]. However, this sensor was, as yet, unable give good colour selection over all areas of the CIE colour triangle, in particular the blue, green, and purple regions of operation.

Regarding the suitability of this structure for use in an active pixel, the requirement for multiple voltage steps is a disadvantage. Such a sensor would require multiple integration steps at each bias point, and a frame memory of some description to store each pixel's result at each voltage. This is a major disadvantage for a two-dimensional image sensing array.

2.3.3 Thin film

Amorphous silicon (a-Si) technology has been employed for some time in solar cells, and large area image sensors such as in fax machines and document scanners [50][51]. Recently, there has been interest in using amorphous silicon and other thin film technologies for imagers and colour detectors.

The use of amorphous silicon offers some advantages over standard silicon processing:

Cost: For large areas such as in solar cells, it is cheaper.

Sensitivity: Over the visible spectrum, a-Si has better absorption, increasing the quantum efficiency.

Layer thickness control: Similar to the use of selective epitaxial growth, very thin layers can be formed with a good degree of accuracy relative to ion implanted or diffused junctions.

Band-gap engineering: By varying the composition of the deposited material the band-gap can be altered. This can be done by introducing germanium or varying the hydrogen content of the layer, for example. Varying the band-gap will change the photon absorption characteristics of the layer, which can be used to tune the spectral response.

On top of CMOS: CMOS circuits can be coated on top with a-Si. This allows active circuitry to be integrated *underneath* the photo-sensitive region. This means that more pixel circuitry can be implemented without compromised pixel fill-factor. [52]

The beauty of the a-Si on CMOS approach is that the optical performance can be optimised without affecting transistor performance. This allows a very small geometry process to be used in the underlying silicon without the photo-diode performance reduction that would result if a CMOS photo-diode were to be used [53][54][55].

Amorphous silicon has been used to make vertically integrated colour detectors and image sensors by employing both the vertically stacked junction and depletion width modulation techniques.

2.3.3.1 Bias voltage based

Figure 2.8 shows a device which was used in a colour image sensor by Sommer *et. al.* [56].

At zero reverse bias, the first region (labelled blue) is active (as the depletion region extends throughout) and the short wavelength generated carriers are collected near the surface. At -1.5 V the green region is also active (depleted), and at -5V the whole device is sensitive. Therefore, three independent responses are obtained. It is worth noting at this stage that the diffusion length of carriers in a-Si is much less than in crystalline silicon, thus the diffusion current contribution from the non-active regions is negligible.

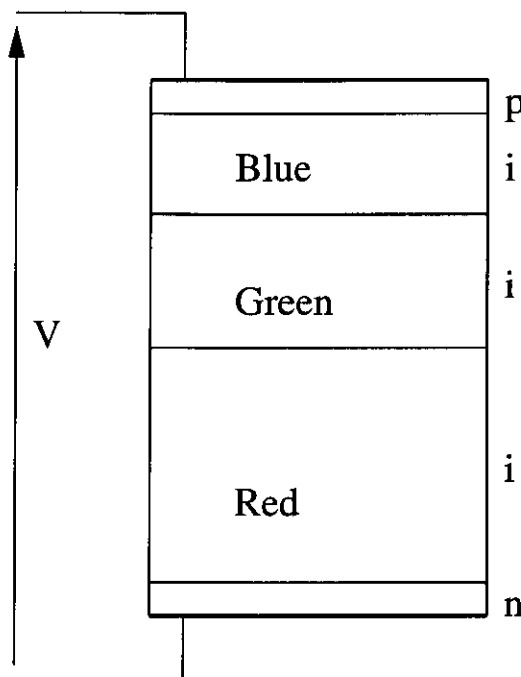


Figure 2.8: *Amorphous colour sensing structure employing depletion width modulation after Sommer.*

By using an on-top of CMOS amorphous detector, more circuitry could be implemented underneath. This allowed the three colour signals to be stored before being read out. In total, 16 transistors and a precision poly-poly capacitor were implemented underneath the photo-diode in a $0.8\ \mu\text{m}$ technology, which would not have been possible if the photo-diode was implemented in the CMOS process.

The colorimetric accuracy of the sensor was not as good in CCD or CMOS sensor using a CFA and more work is required to improve the spectral selectivity and colour processing algorithms. However, for a first attempt, it was a significant achievement. Other similar structures have also been reported recently with comparable performance [57][58][58].

2.3.3.2 Multi-junction based

Many papers have been published on vertically stacked junctions implemented in amorphous silicon e.g. [59][60][61][62][63]. Similarly to epitaxial growth, far more flexibility is possible with a-Si than in the standard CMOS process. Not only can the layer thicknesses and doping be varied, it is also possible to alter the band gaps of each layer individually by introducing impurities. Examples of such colour detectors include *pin-nip-pin*, *pinip-pinip-pinip* and *pin-*

pinip structures. Many other variations are easily implemented. Figure 2.9 shows the structure of two amorphous colour detectors implemented by Knipp *et. al.*

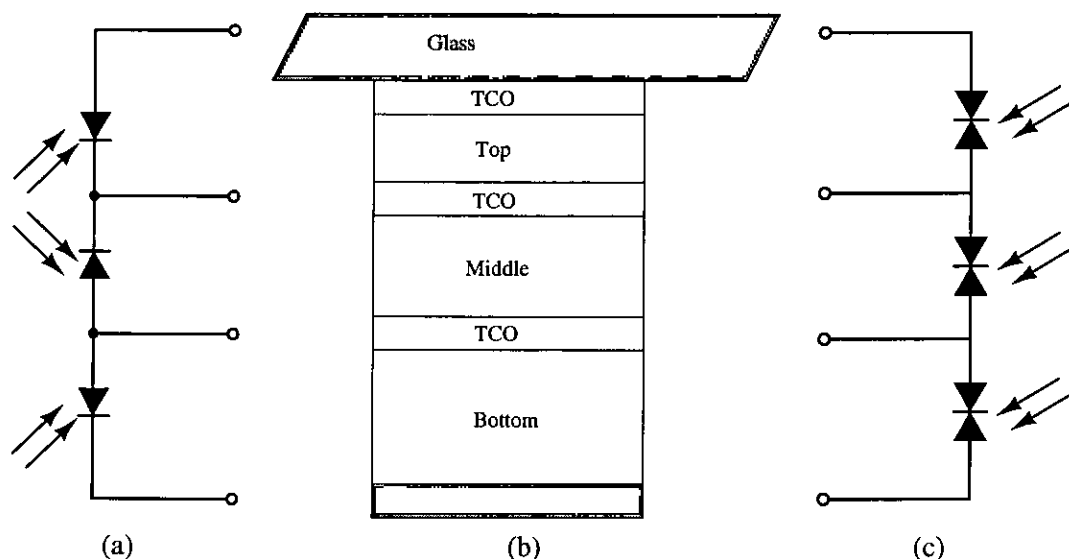


Figure 2.9: Three layer colour detector after Knipp. (a) *pin-nip-pin* circuit (b) 3 layer photo-detector structure (c) *pinip-pinip-pinip* equivalent circuit. Both circuits can be implemented by altering the layers in the structure.

The detector is formed from three regions of a-Si:H separated by transparent conductive oxide (TCO). The device structure shown in Fig. 2.9a provides three independent responses, while that shown in Fig. 2.9c can provide six. However, to get six responses, the bias voltages across the *pinip* layers must be switched.

The optical band-gaps of the layers were altered by Knipp to enhance the spectral selectivity, with the band-gap decreasing with increasing depth into the structure. This reduces the long wavelength absorption nearer the surface as the incident photons lack the necessary energy to be absorbed. As can be seen from Figure 2.10, reasonable spectral separation was obtained.

In a further paper [64], the colorimetric accuracy of the 3- and 6-colour detectors was evaluated after polynomial regression. The 3-channel sensor had reasonable performance (better than a triple-junction device implemented in crystalline silicon), but it was still worse than a commercial colour scanner device. However, the six channel device had excellent colour discrimination. A disadvantage of the six colour approach is that it requires two voltages and hence two integration periods – this is certainly possible with CMOS circuitry integrated under the detector to store each result. A more serious problem is the transient response time of the back-to-back diode configuration when the bias is switched as one of the diodes must be

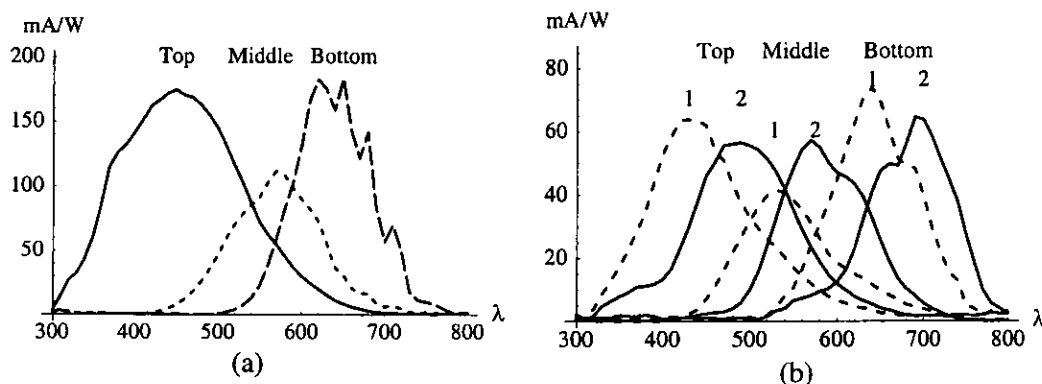


Figure 2.10: Spectral responses of Knipp's (a) three- and (b) six- colour detector.

discharged by the photo-current.

As yet, an image sensor has not been implemented with multi-junction a-Si detectors on CMOS. One difficulty is likely to be contacting the upper two layers to the electronics underneath, which will reduce the fill-factor and increase the manufacturing complexity.

2.3.3.3 Polymer technology

Recently there has been interest in the optoelectronic properties of semiconducting polymers, particularly for displays. It is also possible to use polymers for image sensing [65]. The multi-layer colour sensing approach can also be implemented in a similar way to amorphous technology [66][67]. At the moment, this technology is quite immature and the materials are still being researched.

2.3.4 Summary

The key properties of the colour sensing elements reviewed in this section are summarised in Table 2.1.

It can be seen that only two are compatible with standard CMOS process technology — a key factor if the sensor is to be implemented in such a process. The single junction approach requires a frame store for each pixel large enough to store the colour responses, while the double junction requires a means of generating a third response. By combining the double junction structure with a suitable CFA, a third response with good colour separation should be obtainable.

Device	Number of responses	Standard CMOS?	Comments
Single junction using depletion width modulation	Equal to number of voltage steps	Yes	Requires memory for each pixel. Colour separation poor. Can be small.
CMOS double junction	2	Yes	Requires a means to produce third response. Takes more area than single junction.
Crystalline silicon triple junction	3	No	For good colour separation selective epi process required. Larger area than single or double junction.
a-Si single junction	Equal to number of voltage steps	No	Colour separation not ideal. Requires memory, but allows circuitry underneath. Special fabrication process.
a-Si multiple junction	3 or greater	No	Only single element detectors implemented to date.

Table 2.1: *Summary of colour sensing elements*

The thin film approach is promising, but is really beyond the scope of this project as it requires non-standard manufacturing technology. For this reason, the double junction structure is preferable.

2.4 CMOS pixel circuits

A vast number of CMOS compatible pixel circuits have been proposed and evaluated. Naturally, industry has converged over time towards a few key pixel types. However, as this work is primarily concerned with implementing a colour sensing pixel using a double junction structure, this section concentrates on the relevant circuits. More comprehensive reviews of other pixel types are available elsewhere [68].

The purpose of a pixel is to convert the signal from the photo-detector into a form that can be read out by the addressing circuitry. The photo-detectors described earlier in this chapter produce a photo-current in response to incident light. The pixel circuitry can use this photo-current in the following ways:

Current mode: The photo-current of the detector can be mirrored and read out or read out directly. However, the photo-currents are very small which makes this approach difficult

without introducing mismatch or noise, and hence it will not be covered here.

Charge integration and voltage read out: By accumulating the photo-current on a suitably sized capacitor a voltage is produced. The integration period can be controlled to provide exposure control and keep the resulting voltage at a usable level that can be easily read-out, and to improve the range of light levels that the pixel can be operated in. This is the most common approach in commercial CMOS image sensors.

Charge integration and sensing: The photo-current is integrated on a capacitor over an integration period, and the amount of charge is then sensed by the read out circuitry directly. As the amount of charge is tiny, this can be problematic.

‘Resistive’ current-to-voltage conversion: A resistive load can be used to convert the photo-current into a measurable voltage which can then be read. However, as the photo-currents are tiny, a very large resistance is required to produce a reasonable voltage. This resistance must also be well-matched between pixels to avoid the introduction of large gain offsets.

In the following sub-sections, pixels which employ the last three techniques are described.

2.4.1 1-transistor pixel

The simplest CMOS pixel is the 1-transistor (1-T) or *passive* pixel [69][5][70]. The term passive is used as the pixel contains no amplification or buffering. It consists of a single transistor connected at one end to a bit-line (shared between a column of pixels) and a photo-diode at the other (Fig. 2.11).

To operate the pixel, the access transistor is first pulsed to reset the photo-diode to V_{rt} (the reset voltage). During an integration period, the photo-diode collects generated charge. To read the pixel, the access transistor is again turned on and the amount of charge needed to move the photo-diode back to V_{rt} is sensed by an amplifier in the column. This read therefore destroys the pixel value.

As only a single transistor is required the fill-factor (in terms of photo-diode area) can be maximised. A large voltage swing on the photo-diode along with a larger capacitance can be achieved, giving a larger saturation charge for a given pixel size than competing pixels.

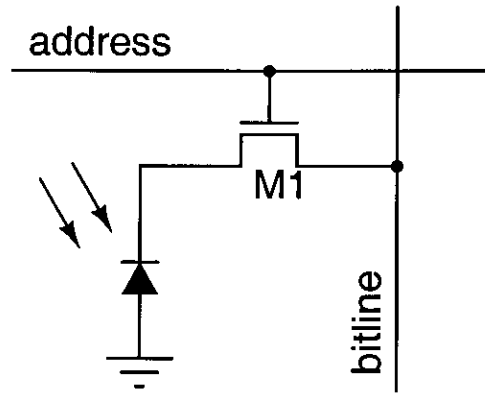


Figure 2.11: 1-T pixel circuit.

However, for large arrays, the readout of this pixel requires a very small photo-diode charge to be sensed on a large bit-line capacitance which can cause considerable problems. Another problem is that the bit-lines themselves can collect photo-generated charge comparable with the photo-diode charge.

2.4.2 3-transistor pixel

This pixel includes a buffer transistor (M1) to isolate the photo-diode from the bit-line. It is operated as follows:

- The photo-diode is reset to voltage V_{rt} by turning on M2.
- Over a suitable integration period, photo-generated charge is accumulated on the photo-diode, discharging it from the reset voltage.
- To read the pixel value after integration, M3 is turned on and the photo-diode voltage is buffered through M1 which forms part of a source follower circuit. This voltage is stored on a capacitor in the column, or digitally.
- The pixel is the reset and in the same manner the reset value is stored on a capacitor in the column. The difference between the after integration and the reset values is the pixel result.

The subtraction of the reset value from the pixel value after integration removes the threshold voltage of M1 from the result. This technique is known as *correlated double sampling* (CDS).

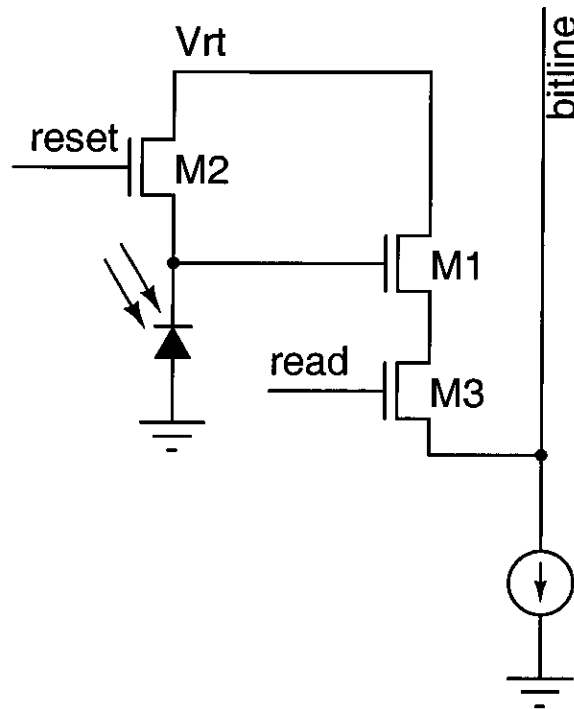


Figure 2.12: 3-T pixel circuit.

Without CDS, mismatches in the threshold of M1 would appear in the image as a fixed pattern noise source.

During the reset of the photo-diode, kTC noise (the band-limited thermal noise of M2) is sampled onto the photo-diode capacitance. This contributes noise during CDS with a value (in electrons) of:

$$\sqrt{2} \frac{\sqrt{kTC}}{q} \quad (2.7)$$

The $\sqrt{2}$ in Eq. 2.7 is due to the fact that the pixel is reset twice during the CDS process. Thus two amounts of uncorrelated kTC noise are added.

Reading from this pixel is non-destructive. Therefore various techniques have been proposed to increase the dynamic range by using multiple integration times [71].

2.4.3 3-transistor cell with cascode

By adding an extra transistor the charge to voltage conversion gain of the 3-T pixel can be increased. An increase in conversion gain can be desirable, as it reduces the noise contribution from the readout circuitry. The transistor M4 (see Fig. 2.13) buffers the photo-diode capacitance from the capacitance at the gate of M1. A suitable voltage must be applied to the gate of M4 to hold the photo-diode at a reverse biased voltage a V_{GS} below. The photo-generated charge is now integrated on the capacitance at the gate of M1 which does not include the photo-diode. Thus, the conversion gain is increased.

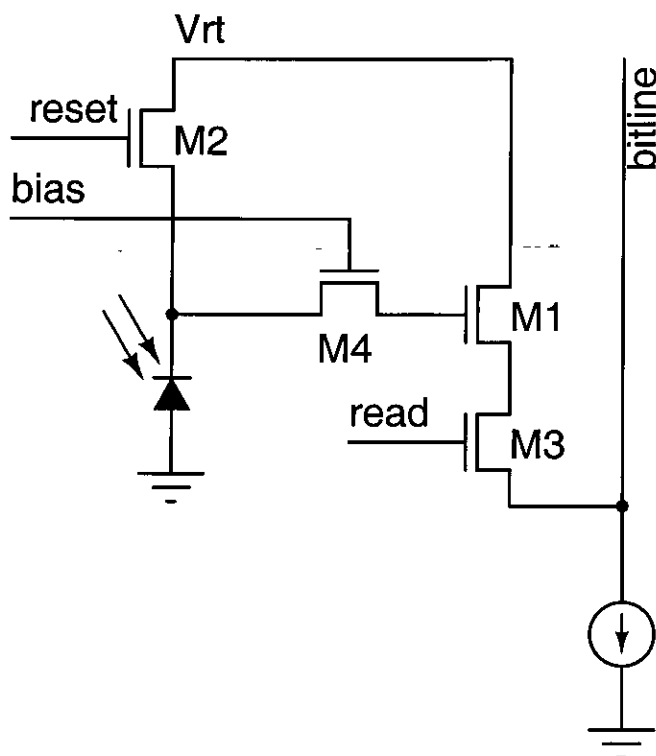


Figure 2.13: 3-T pixel with cascode transistor to increase the conversion gain.

An obvious disadvantage of this circuit is that an extra transistor is required. Additionally, *lag* is also introduced, as a step in photo-current must first adjust the V_{GS} of M4 by charging the photo-diode capacitance before any photo-current is integrated on the sense node.

2.4.4 4-transistor pixel

The 4-transistor (4-T) cell [72][73] can be thought of as a single element CCD image sensor combined with a 3-T pixel (Fig. 2.14). The photo-diode is used to collect photo-generated

charge in a potential well. The collection region is isolated from a sense capacitance by a transfer gate (M1).

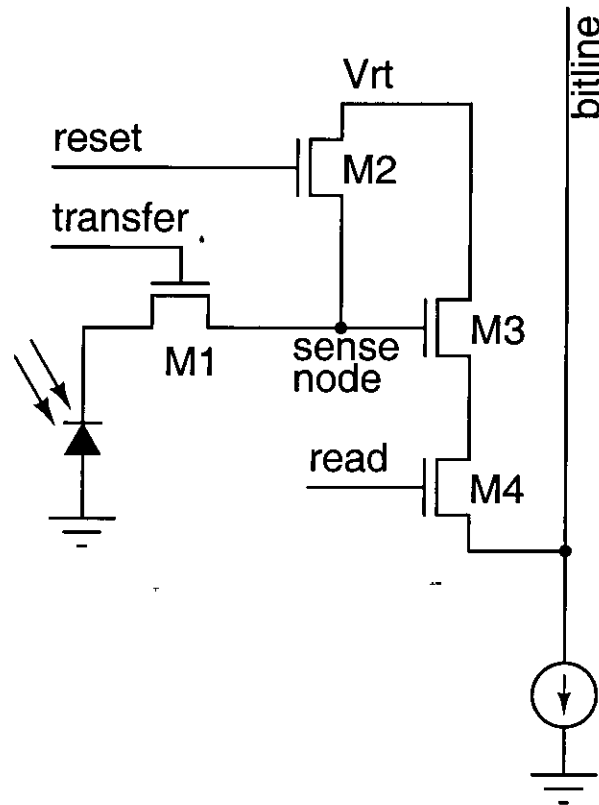


Figure 2.14: 4-T pixel circuit.

The operation of this pixel is as follows:

- The photo-diode is reset by turning on the reset transistor (M2) and the transfer gate (M1).
- The transfer gate is switched off, and integrated charge is stored in the photo-diode.
- After a suitable integration period, the sense capacitance is released from reset and the pixel output value at this moment is stored.
- The transfer gate is turned on, and all the photo-generated charge flows onto the sense capacitance, producing a voltage difference. The output of the pixel is then stored.
- The two stored pixel values are subtracted from each other to remove any offsets in the pixel source follower and also *any reset noise present on the sense capacitance*. Thus this pixel does not suffer from kTC noise like the 1-T and 3-T cells.

The design of this pixel requires a specially tailored photo-diode with a pinned surface region (usually p-type). This is because the photo-diode must be designed such that all mobile (photo-generated) charge is removed during the read or reset sequences. This ensures that the image sensor will not suffer from *lag* [74], and that there is no uncertainty in the charge transfer from the photo-diode to the sense capacitance. If there is no charge remaining in the photo-diode then there can be no kTC noise contributed from the transfer through M1. It is better to think of this device, not as a transistor, but rather as a single element CCD. To get this behaviour, the design of the photo-diode is critical. In general this has required extra masks and implants during manufacturing. The pinning layer can also reduce dark current due to surface states, in fact this was the original motivation for its introduction in CCDs.

The full well capacity of this pixel type is often lower than for a 1-T or 3-T pixel, as the sense capacitance takes up some of the area of the pixel, and must be designed such that, for its allowed voltage swing (set by the requirement for the photo-diode to fully deplete), it has a larger charge capacity than the photo-diode.

The performance benefit from the removal of kTC noise is considerable, especially under low light conditions, and several large companies have adopted this pixel (or variants) in their CMOS image sensors [75][76][77][78]. Notably, this photo-diode structure is also very commonly used in CCD image sensors [79][80].

It is also possible to replace the photo-diode with a photo-gate [81][7][82] under which the photo-charge is collected in a similar manner. However, as incident photons must go through a polysilicon layer, the blue response is severely reduced.

2.4.5 Logarithmic pixel

Photo-diode photo-current is linear over more than 5 orders of magnitude of light intensity. To exploit this for high dynamic range imaging, a pixel with a logarithmic response can be used and many sensors employing this technique have been proposed [83][84][85]. In the sub-threshold region of operation, the drain source current of a MOS transistor has an exponential dependence on V_{GS} [86]:

$$I_{DS} = \frac{W}{L} I_{D0} e^{\frac{V_{GS}}{nU_T}} \left(1 - e^{\frac{-V_{DS}}{U_T}} \right) \quad (2.8)$$

where n is the sub-threshold slope factor and U_T is the thermal voltage $\frac{kT}{q}$. This is for fixed V_{SB} which may not be the case, but this is a small effect and in this analysis the body effect will be neglected.

A pixel with logarithmic response is shown in Figure 2.15.

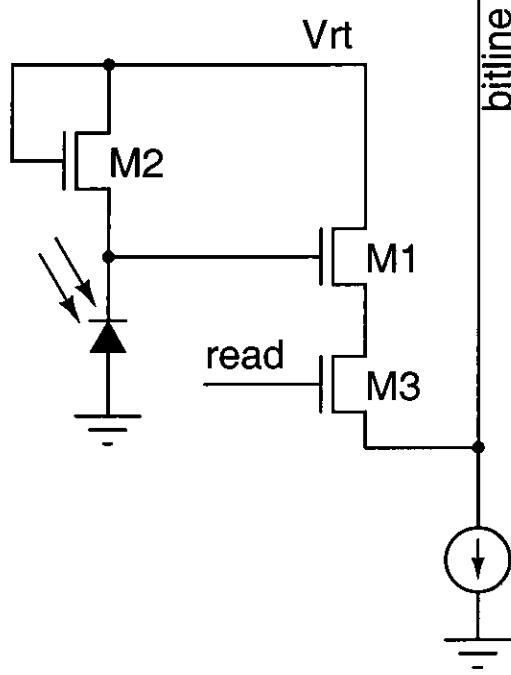


Figure 2.15: Log pixel circuit.

The pixel photo-diode varies from fA to nA depending on the incident light intensity. This is not enough to move a MOS transistor out of the sub-threshold region of operation. Under steady-state conditions, the photo-diode current through transistor M2 moves the photo-diode voltage to:

$$V_{PD} = V_{rt} - nU_T \ln \left(\frac{L}{W} \frac{I_{DS}}{I_{DO} \left(1 - e^{-\frac{V_{DS}}{U_T}} \right)} \right) \quad (2.9)$$

From equation 2.9 we can see that V_{PD} has a logarithmic dependence on photo-current. The photo-diode voltage is buffered through M1 which forms half of a source follower circuit and read out through a bit-line..

While the logarithmic pixel has a huge dynamic range, more than 5 orders of magnitude, it

suffers from three major problems:

1. The voltage swing on the photo-diode is of the order of 50 mV/decade of light intensity which is quite small.
2. The fixed pattern noise contribution from pixel transistor offsets is of the same order as the voltage swing. As the photo-diode is not reset standard CDS cannot be used. This renders any raw images unusable. By storing and subtracting the pixel offsets the FPN can be reduced to $< 2\%$ [87] which is still too high for consumer use but may be suitable for industrial applications. However, this requires a frame store which is an additional system cost. Alternatively, by adding extra transistors to the pixel, it is possible to inject a reference current into the load transistor and remove the offsets [88][89], but this increases the pixel complexity and size.
3. Finally, this pixel also suffers from lag. For example, if a photo-current changes from a large value to a small one in a step, the photo-diode capacitance must be charged up by the sub-threshold transistor M2. If the current then rises slightly, the small photo-diode current must discharge the photo-diode capacitance. This means that at low light levels there could be considerable (~ 1 s) delay before the pixel voltage settles.

The reader will no doubt have realised that the pixel circuitry shown in Figure 2.15 is very similar to the standard 3-T pixel. It is therefore possible to implement a sensor in which both log and linear modes of operation are available [90].

2.4.6 Summary of pixel circuits

Table 2.2 shows the main advantages and disadvantages of the pixel types reviewed above. For single photo-junction sensors the 4-T pixel provides the best balance of fill-factor, noise performance, and lag free operation. However, it requires a pinned photo-diode which means it cannot be used with any of the colour detectors described in this chapter. The 1-T pixel and log pixels suffer from their poor FPN performance. The log and 3-T with cascode pixels suffer from lag which is a problem. It therefore seems likely that the best choice for use in conjunction with a colour sensing element will be a development of the 3-T pixel. In chapter 5, such pixel circuits are investigated.

Pixel type	Fill-factor	FPN performance	Temporal noise performance	Lag?
1-T	Best	Poor	$\sqrt{2kTC}$ + output stage	No
3-T	Medium	Good	$\sqrt{2kTC}$ + output stage	No
3-T with cascode	Low	Good	$\sqrt{2kTC}$ + reduced output stage noise due to better conversion gain	Yes
4-T with pinned photo-diode	Low	Good	No kTC + reduced output stage noise due to better conversion gain	No
Logarithmic	Medium	Poor	\sqrt{kTC} + output stage	Yes

Table 2.2: *Summary of pixel circuits*

2.5 Conclusion

This chapter has shown that many people have exploited the physical properties of silicon to perform colour detection. The colorimetric accuracy of crystalline silicon colour detectors has reached an acceptable level after colour matrixing is performed, though this matrixing process can considerably degrade the SNR (see section 1.3). Epitaxial growth and amorphous silicon have been used to produce more complex devices with improved performance, but this has required more complex manufacturing with an associated cost.

It is clear from the literature that there remains scope for implementation of a colour image sensor which combines the ability of silicon to sense colour with a suitable colour filter array to improve the colorimetric accuracy. Active pixel circuitry can provide the link between the discrete colour detector and the image sensor readout circuitry. In the following chapters, such an approach is investigated.

Chapter 3

TCAD modelling of photo-diode structures

3.1 Introduction

The use of Technology Computer Aided Design (TCAD) has become widespread in the semiconductor manufacturing industry [91][92][93]. As an alternative to running physical splits on real silicon wafers, it can provide a faster and more cost effective method of evaluating semiconductor device performance after process changes. In this chapter, device simulation tools are employed to investigate the effect of manufacturing changes on photo-diode response.

In particular, this chapter details changes that can easily be made to both the standard n^+/p_{well} and double junction structures' spectral responses and sensitivities. The changes investigated were to the epitaxial layer thickness, junction depths, and doping levels.

3.2 TCAD methodology

3.2.1 Simulator limitations

The simulator tool used was MEDICITM from Avant!. It is a 2-dimensional device simulator originally based on Stanford University's PISCES.

MEDICI uses non-linear iteration methods to solve the partial differential equations governing the electrical behaviour of semiconductors (Poisson's equation, the continuity equations, carrier energy balance equations, and the lattice heat equation) [94]. The simulator incorporates various mobility, recombination, band-gap, and tunnelling models as well as an advanced application module for modelling optoelectronic devices.

This simulation tool, though powerful, is not without its limitations for the modelling of photo-diodes. Some of the issues encountered during this simulation work were:

Simulation mesh: Accurate device simulation requires that the simulation mesh is adequately specified. As the simulation time is proportional to the number of mesh points squared one does not usually want too many nodes. Unfortunately, an adequate node count is not easy to specify, being dependent on the device and the type of simulation. One methodology (the one adopted here) is to gradually increase the mesh resolution until the difference in the simulation results becomes negligible.

Simulation parameters: The simulation tool is merely solving a set of coupled equations. It is up to the user to provide meaningful coefficients for these equations. In particular (as has been discussed in Section 2.2) minority carrier lifetimes and diffusion lengths are very important for photo-diode operation. Unfortunately these parameters are dependent on factors such as wafer contamination, defects introduced during processing, and annealing treatments applied. These parameters are not easy to measure without fabricating special test structures. They are also liable to vary from one equipment set to another and indeed from batch to batch. Therefore, in this case the default parameters have been used. While this may not produce simulation results precisely matching reality, it still allows the investigation of the main process parameters affecting photo-diode performance, which is the main purpose of this investigation.

Process data: Of equal importance is the structure data that is input to the device simulator. Unfortunately, semiconductor manufacturing companies guard this information very closely. It has been possible to obtain some process simulation results from industrial contacts and this has been used wherever possible in the simulations. Both $0.5\ \mu m$ and $0.35\ \mu m$ process data has been obtained.

Optical modelling limitations: The MEDICI optical advanced application module has been used in this analysis. This module can be used to model photo-generation in the silicon caused by incident photons. While it does permit ray tracing of incident beams through the dielectric stack it does not model the constructive and destructive interference. This can be plainly seen in the simulation results, where the large periodic fluctuations in quantum efficiency observed in real measurements are not present. The software *does* model the wavelength dependence of photon absorption in silicon, which is the most important aspect of the simulation in this case. More advanced modelling of the dielectric stack has not been done in this work.

Dark current modelling limitations: Studies have shown that most of the dark current in CMOS

compatible photo-diodes is perimeter and surface dominated [53]. This leakage is caused by the increased stress due to the local oxidation, and by defects at the surface in the silicon-oxide interface (such as dangling bonds). While surface recombination can be modelled using a surface recombination velocity parameter one must still know the correct value to get meaningful results. To determine the surface recombination test structures must be fabricated. It is the author's opinion that, as reality is usually more accurate than simulation, once this parameter has been measured on a test structure there is little point in simulating it! Additionally, the effects of stress caused by LOCOS on generation and recombination are not modelled in any commercial TCAD tool-set, at present.

Even leakage caused by bulk generation is difficult to model as the currents produced are of the same order as the noise in the numerical techniques caused by finite precision arithmetic. Though methods have been proposed [95] to estimate this, they are at best an estimate due to the inexact nature of the lifetime parameters used.

3.2.2 Experimental procedure

Three different methods were used to define the device structure:

- *2-D simulation results:* A collaborating foundry kindly agreed to create process simulation cross-sections from layout files. Only the standard n^+/p_{well} pixel structure was simulated using a $0.5\ \mu m$ process recipe. The simulations were performed using a calibrated 2-D process simulator. These results were then read into the device simulator. The simulation mesh was redefined, as usually the mesh created during process simulation is not ideal for device modelling.

This method allows a realistic device structure to be used. However it is more difficult to change the structure data without access to the process simulation tool. One of the things it was possible to change was the epitaxial layer thickness and type. It was also possible to simulate the cross-talk between neighbouring pixels, by duplicating the structure.

- *1-D doping profiles:* These were obtained for both $0.5\ \mu m$ and $0.35\ \mu m$ technologies. The structure was created inside the device simulator by reading the profiles into designated device regions. The lateral diffusion of the impurities was approximated by a Gaussian tail-off. Because of this, this method is less accurate in the lateral dimension

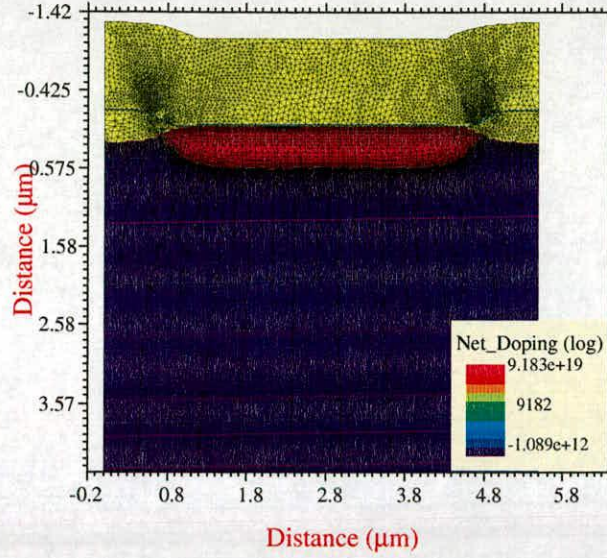


Figure 3.1: Cross sectional view of the n^+/p_{well} photo-diode

than the first method described above. However, it allows the device dimensions to be defined inside the device simulator.

- *Analytical profiles:* For greatest flexibility, doping levels can be defined analytically inside the device simulator. This was the approach used to create the $0.5\ \mu m$ double junction structure and for the optimisation simulations. This gave complete freedom to alter the junction depths and doping levels of the device. While it is not as accurate as either method defined above, being able to alter the structure easily is a great aid to understanding the device dependencies on structure and process.

3.3 Standard diode results and experiments

3.3.1 Base case

Figure 3.1 shows a simulated n^+/p_{well} photo-diode in cross section. The red region is n-type, and the purple region p-type, while insulators are shown in yellow. It can be seen that there is no epitaxial layer in this cross section; the device has been grown on a lightly doped substrate.

This structure was produced from calibrated 2-D process simulations and read into the device simulator. The simulated spectral response of this photo-diode is shown in Figure 3.2. It can be seen that the magnitude of the response varies linearly with the incident power as expected.

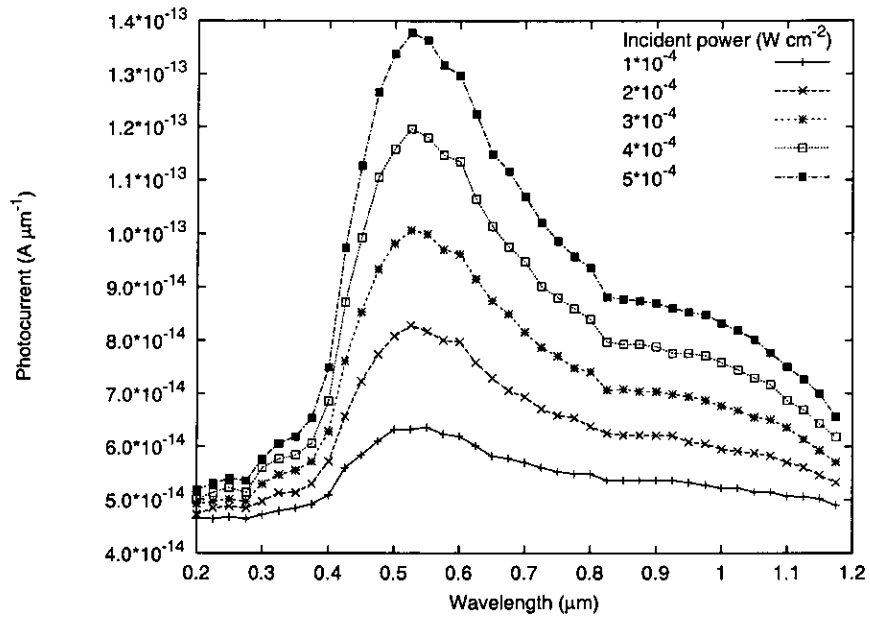


Figure 3.2: Spectral response of the n^+/p_{well} photo-diode.

3.3.2 Effect of epitaxial layer

During semiconductor manufacture it is relatively easy to alter the starting silicon material. In particular the epitaxial layer thickness can be varied — wafer suppliers offer a range of substrates and many fabrication plants have their own epi reactors.

If an epitaxial layer is grown on a heavily doped substrate the presence of this region of high doping can effect spectral response in two ways:

1. *Lifetime*: The lifetime of minority carriers in this heavily doped region will be much shorter than in the epilayer, therefore carriers generated in this region are unlikely to be collected by the photo-diode.
2. *Potential barrier*: If the heavily doped region is p-type, it will result in a potential barrier which should prevent minority carriers in the epilayer moving downwards — thus increasing the chance of the carrier being collected by the photo-diode. If the region is n-type another junction is present under the photo-diode which will collect carriers near it.

Figure 3.3 shows, in cross section, the doping levels of the n^+/p diode with 4 μm epi and heavily doped substrate. A variety of substrate doping levels and epi thicknesses were simulated

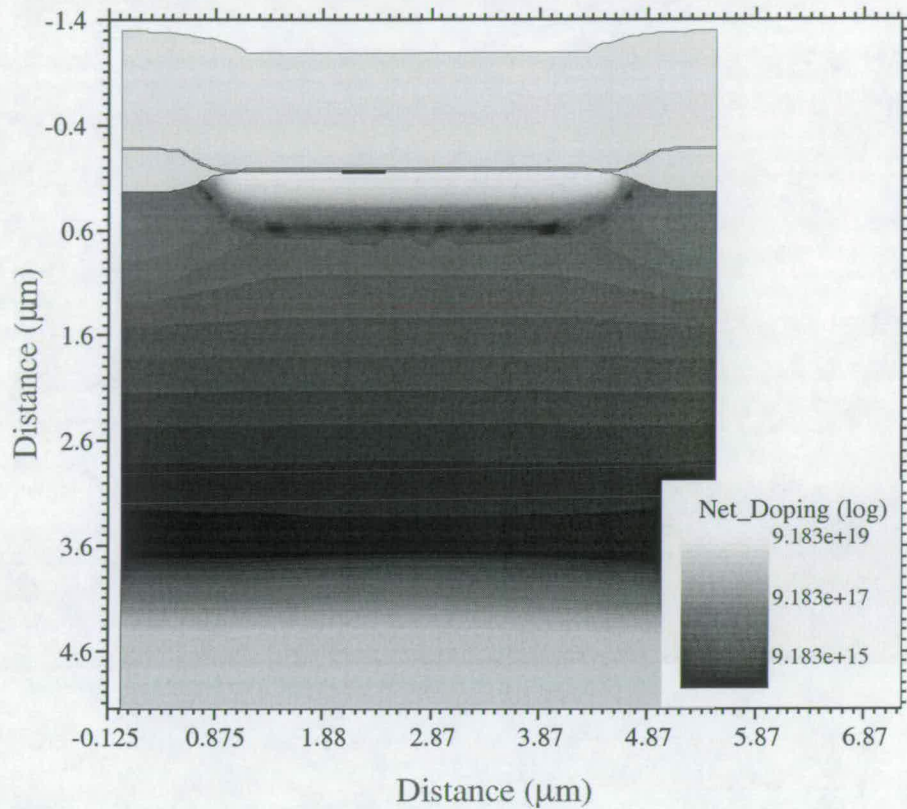


Figure 3.3: Photo-diode with 4 μm epilayer and heavily doped substrate.

and as expected, it was found that the greatest effect on the spectral response occurred with the thinnest epi and the heaviest doping. A structure was also created with a heavily doped n-type substrate.

Figure 3.4 shows the variations in spectral response. The response with a P^{++} substrate is improved over the visible spectrum — this is attributed to the potential barrier caused by the heavily doped substrate (Fig. 3.5). This is an important result as it suggests thinning the epilayer may improve the quantum efficiency.

The response with an n-type substrate is also interesting, as the infra-red response has been decreased dramatically. For everyday image sensors this part of the response must be eliminated by a special IR filter at considerable extra cost. It is possible to further reduce the IR response by reducing the epi thickness or by biasing the n-type substrate to extend the depletion region further into the epi. However, it is likely that having an n-type substrate under active circuitry would cause problems with latch up. Thinning the epi is likely to exacerbate this.

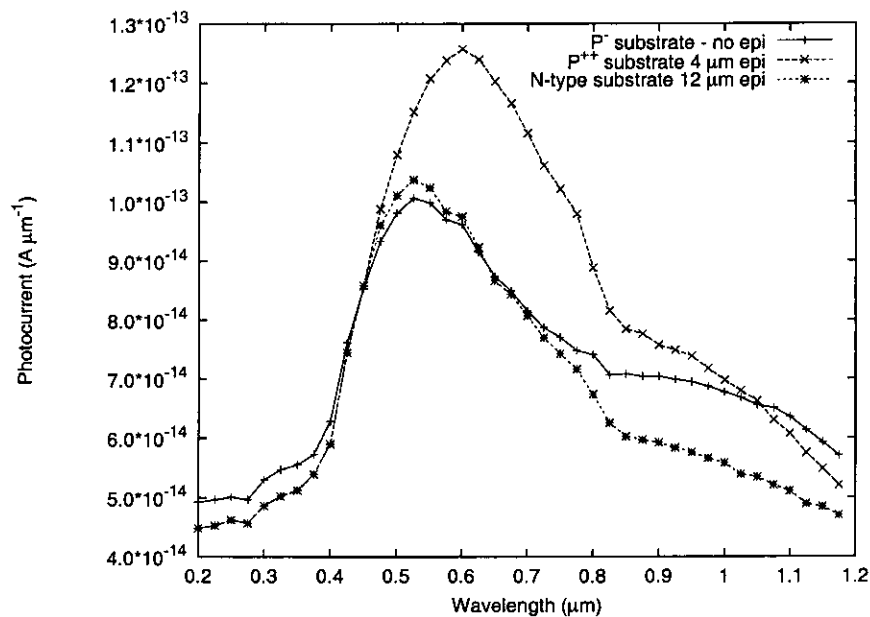


Figure 3.4: Spectral response with varying epilayer thickness and substrate.

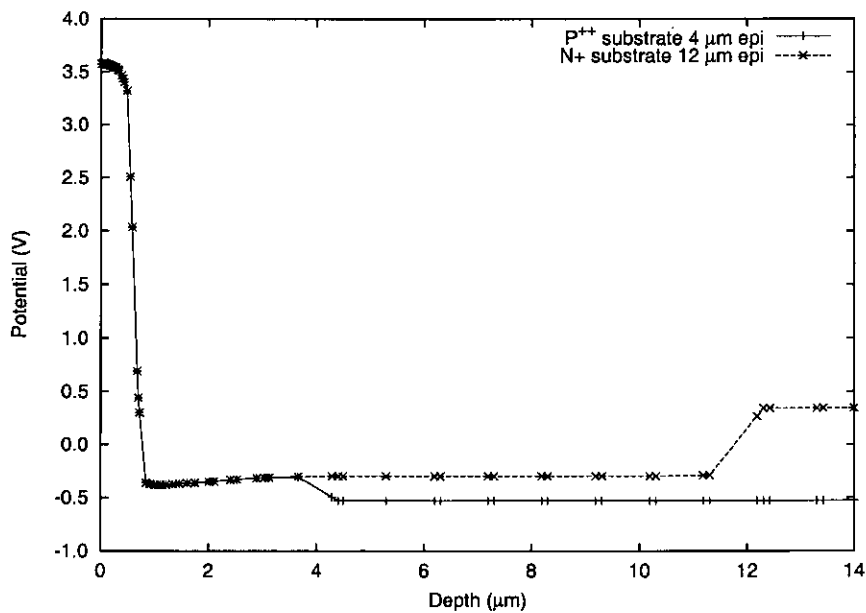


Figure 3.5: Potential profile vertically through the structure.

3.3.3 Cross-talk

By placing two identical structures side by side in the simulation and illuminating one of them, it is possible to simulate the photo-current cross-talk between pixels. However, determining cross-talk in a real pixel is a 3-dimensional problem — the cross-talk depends on small potential barriers caused by P-wells due to pixel transistors. Therefore results from a 2D simulation provide, at best, only a crude estimate.

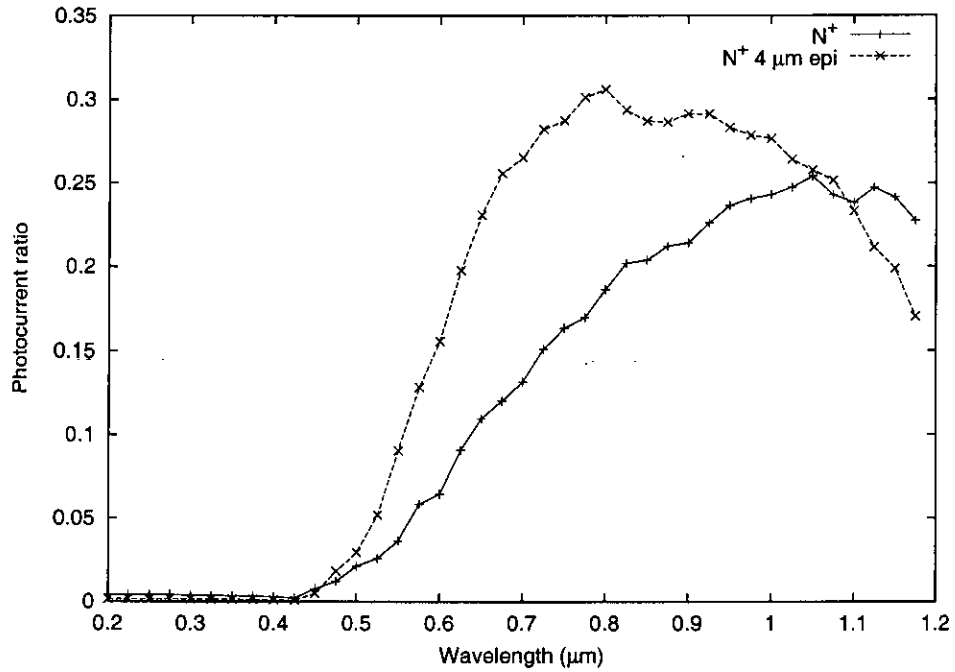


Figure 3.6: *Simulated cross-talk of the standard pixel.*

The cross-talk (ratio of the photo-current of the dark pixel to the illuminated pixel) of the n^+/p_{well} pixel is given for both the base (labelled N+) and 4 μm epi thickness cases (Fig. 3.6). The gap between the pixels was approximately 2 μm . It can be seen that thinning the epi results in an increased cross-talk between pixels in the simulation.

3.4 Double junction preliminary results

A double junction structure was created using analytical doping profiles matched as closely as possible to 0.5 μm spreading resistance profile results (Fig. 3.7). The illumination was restricted such that incident photons went through all three regions of the p-n-p structure — no photons were incident on parts of the structure where the N-well was uncovered by P^{++} . The



spectral response is shown in Figure 3.8 along with that from a device created using $0.35\ \mu\text{m}$ process simulation doping profiles (no exact $0.5\ \mu\text{m}$ information from process simulation was available). The n_{well} was biased at 2V and the p^+ at 1V, so both junctions were reverse biased. It should be noted that responses are those of the P-substrate/N-well junction and the n^+/p_{well} junction currents rather than the P^+ and N-well terminal currents. The terminal current though the N-well is actually the sum of the two junction currents. In a real pixel it would be necessary to subtract the P^+ current from the N-well to get these two responses.

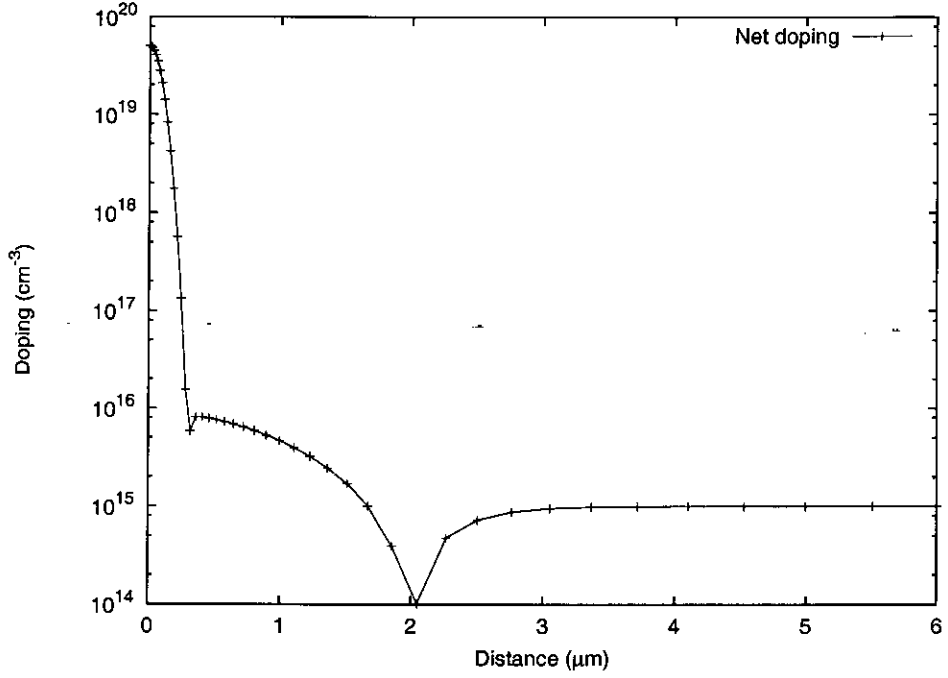


Figure 3.7: Doping profile of the defined DJ structure.

The cross-talk between two side by side DJ structures was also simulated using the $0.35\ \mu\text{m}$ data to get an estimate of the likely magnitude. The ratio of the photo-diode terminal currents is given below for a gap of $2\ \mu\text{m}$ between the two structures.

It is clear that there is no detectable cross-talk between the p^+ regions as is to be expected. With the N-well regions there is some cross-talk but it is lower than for the standard n^+/p_{well} diode.

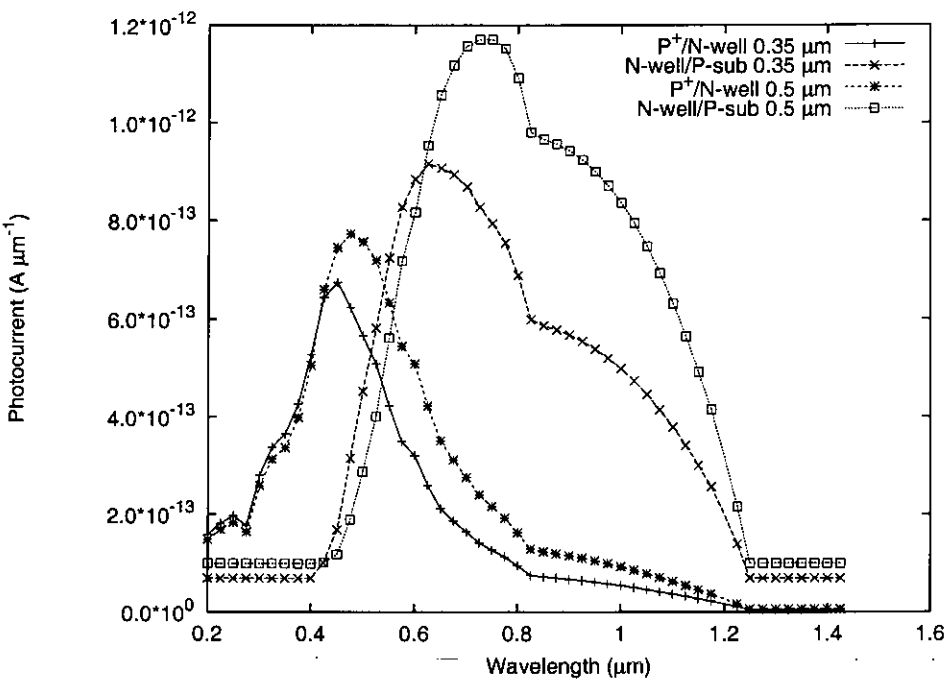


Figure 3.8: Simulated spectral response of the DJ structure.

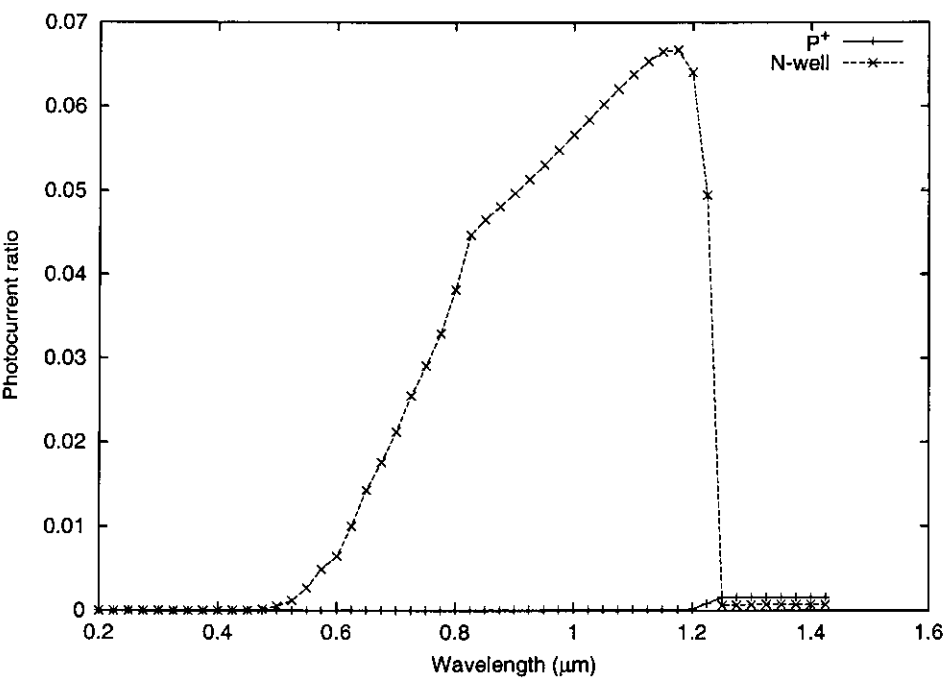


Figure 3.9: Ratio of photo-current cross-talk between two DJ photo-diode structures.

3.5 DJ optimisation

3.5.1 Experimental design

The junction depths and doping profiles of the DJ structure were varied in a statistically designed experiment. The control parameters in this experiment are shown in Table 3.1. These are consistent with the ranges that would be available during manufacturing.

Control factor	Min. value	Max. value
p^+/n_{well} junction depth	$0.2 \mu m$	$0.6 \mu m$
$n_{well}/p_{substrate}$ junction depth	$1.5 \mu m$	$2.5 \mu m$
p^+ peak doping	$5 \times 10^{17} \text{ cm}^{-3}$	$1 \times 10^{19} \text{ cm}^{-3}$
n_{well} doping	$3 \times 10^{16} \text{ cm}^{-3}$	$2 \times 10^{17} \text{ cm}^{-3}$
Substrate doping	$1 \times 10^{15} \text{ cm}^{-3}$	$9 \times 10^{15} \text{ cm}^{-3}$

Table 3.1: Control factors in the DJ experiment

The control factors were varied in a CCF experimental design [96] consisting of 77 splits. A quadratic polynomial model was fitted to the results. This model accounted for 98% of the variation in the responses.

3.5.2 Analysis of main effects

Significance testing was performed on the results of the experiment to determine the dominant control factors. Figures 3.10 and 3.11 show the results of this analysis.

It is clear that parameters affecting lifetime in the two photo-generation regions make the greatest difference to the response. For the $n_{well}/p_{substrate}$ response, the most important factors are the epilayer thickness and the epi doping — this controls the width of the depletion layer between the n-well and epi and also the lifetime of photo-generated charge. As most of the $n_{well}/p_{substrate}$ depletion width extends into the more lightly doped region changing the other parameters does not have a large effect.

Likewise, a similar picture emerges for the p^+/n_{well} response. The n_{well} doping level is the most significant factor affecting this p^+/n_{well} photo-current though in general it is not as easy to vary this response. Punch-through from the p^+ region to the epi layer (when the two depletion regions touch) sets the limit on the lowest N-well doping that can be used. Figures 3.12 and 3.13 show the variation in the terminal currents as the most significant control factors are varied.

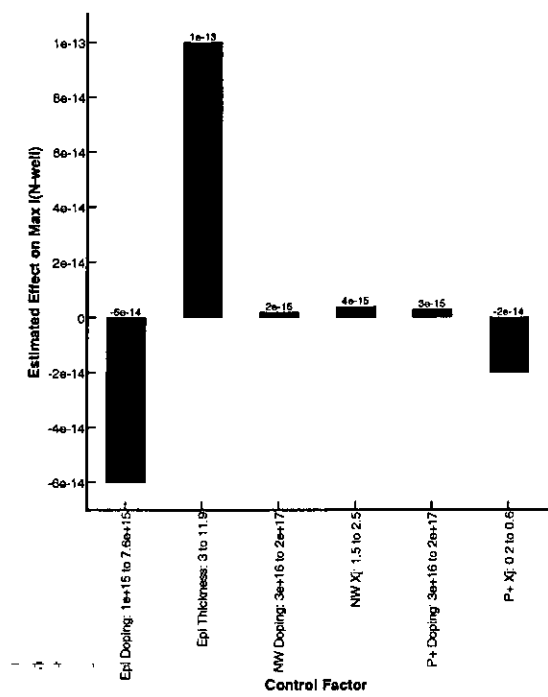


Figure 3.10: Main effects on the $n_{well}/p_{substrate}$ peak response.

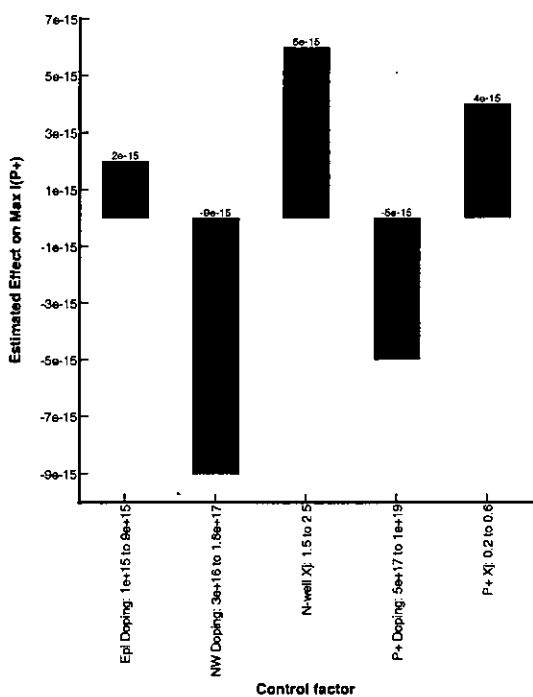


Figure 3.11: Main effects on the p^+/n_{well} peak response.

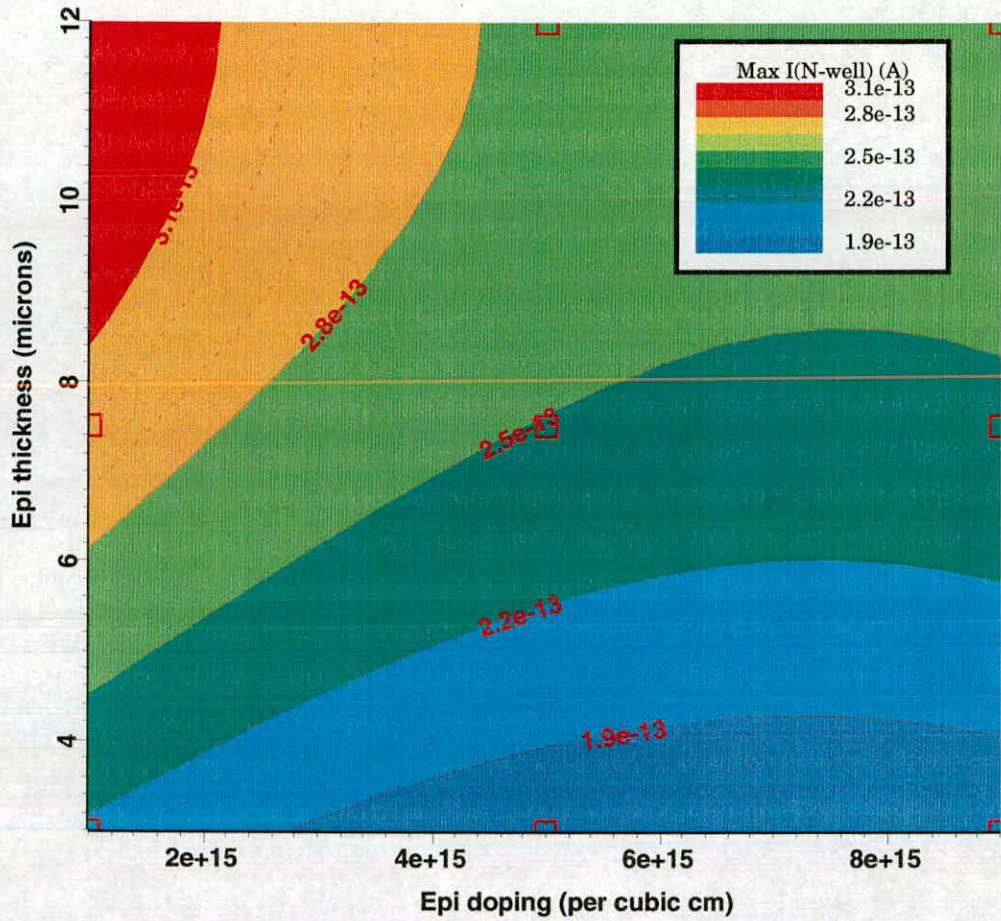


Figure 3.12: Contour plot showing variation in $n_{\text{well}}/p_{\text{substrate}}$ photo-current with varying epi doping and thickness. Fixed factors: $P+$ doping = $5e18 \text{ cm}^{-3}$, $P+$ $X_j = 0.2 \text{ }\mu\text{m}$, $N\text{-well } X_j = 2 \text{ }\mu\text{m}$, $N\text{-well doping} = 1e17 \text{ cm}^{-3}$.

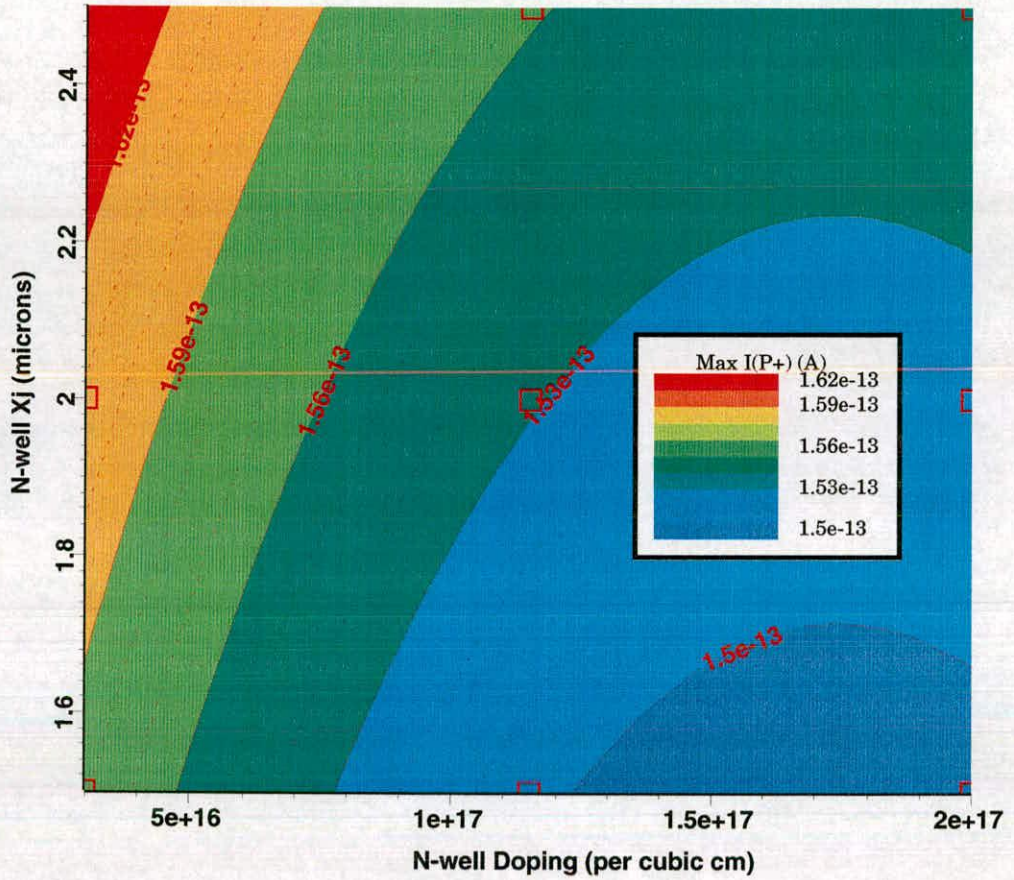


Figure 3.13: Contour plot showing variation in p^+/n_{well} photo-current with varying N-well doping and junction depth. Fixed factors: P^+ doping = $5e18 \text{ cm}^{-3}$, $P^+ X_j = 0.2 \text{ } \mu\text{m}$, epi thickness = $7.5 \text{ } \mu\text{m}$, epi doping = $5e15 \text{ cm}^{-3}$.

3.5.3 Optimisation

The polynomial model can be used to predict responses within the experimental design space and for optimisation. An equal response from the two junctions would simplify the pixel design and the further processing required. A composite response was defined as:

$$CR = \frac{I_{p+}}{I_{n-well}} \quad (3.1)$$

where CR is the ratio of the p^+/n_{well} photo-current to the $n_{well}/p_{substrate}$ photo-current. By searching the design space such that $CR \simeq 1$ the two responses can be matched. A second criteria of maximising the p^+/n_{well} response ensures that sensitivity is kept as high as possible. A confirmation run was performed to confirm that the parameters extracted from the model resulted in the correct responses. Figure 3.14 shows that such an optimisation is indeed possible.

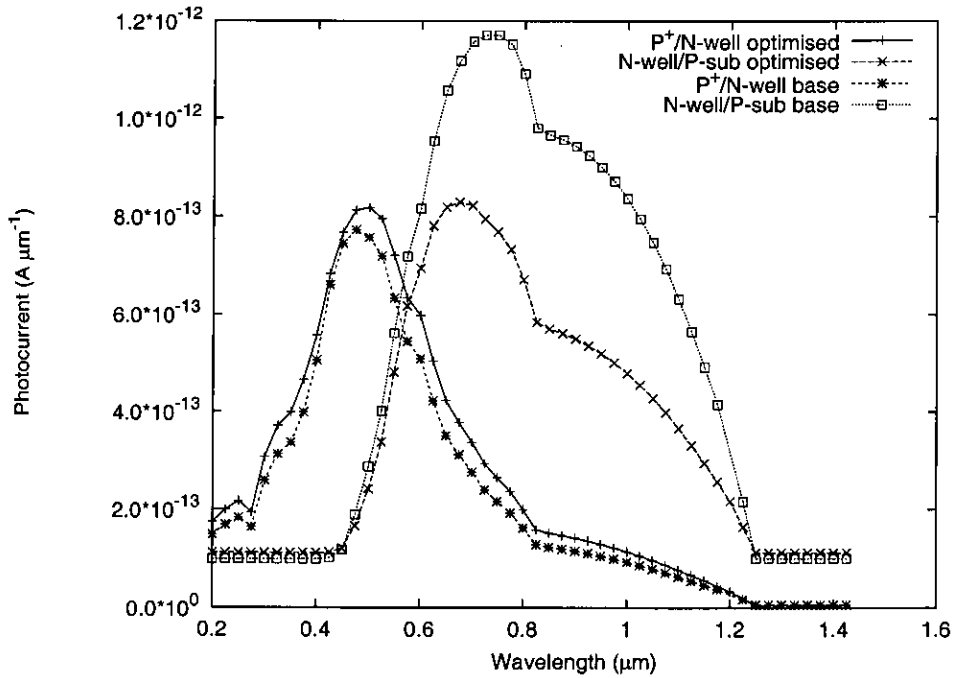


Figure 3.14: *DJ response after optimisation.*

To match the two responses the $n_{well}/p_{substrate}$ sensitivity has been reduced while the p^+/n_{well} has only slightly increased. In fact, this analysis has shown that it is far easier to reduce a response than to increase it — all that needs to be done is to reduce the minority carrier lifetimes and depletion widths by introducing more dopant. Increasing the response means reducing the doping levels and widening the resulting depletion regions as is done in $p-i-n$ photo-diodes. In

the DJ device this is not easy to do as punch through sets a lower bound on the doping levels.

By reducing the response of the N-well/P-sub junction the overall sensitivity of the image sensor would be lower, resulting in decreased imaging performance at low light levels.

3.6 Conclusion

This chapter has shown that the spectral response of both standard photo-diodes and of the DJ structure can be modified by changing the doping levels and junction depths inside the device. These changes are relatively easy to make during manufacturing but many would impact transistor and other device performance. The addition of extra masks and process steps limited to the photo-diode alone would allow such changes to be made without compromising transistor operation but would obviously increase manufacturing cost.

One important change that can easily be made is the epi thickness and simulations suggest that this may be a way of increasing the quantum efficiency of the standard pixel..

Modelling of the double junction structure shows that the two junction responses can be changed significantly but it has been found easier to decrease the responses than to increase them. In the context of the DJ structure this means that it is probably undesirable to alter the structure to match the two responses — therefore a more complicated readout circuit may be required. More positively, cross-talk performance in the DJ structure is superior to the standard pixel. In particular, there is no cross-talk between p^+/n_{well} junctions. It is possible that this pixel output could therefore be used to improve image sharpness.

Chapter 4

Quantum efficiency measurements

4.1 Introduction

In order to assess the suitability of the double junction structure for colour imaging, spectral measurements have been performed. In this chapter the measurement methods and results are presented along with a comparison with standard single junction photo-diode measurements.¹

4.2 Test structure design

Care was taken with the design of the QE measurements to reduce the effect of carriers generated outside the photo-diode active area and to reduce measurement noise:

- To reduce the amount of charge collected from outside the active diode area N-well guard rings $50\ \mu m$ wide were placed around the diode. Metal 2 was also used as a light shield above the perimeter of the photo-diode and guard rings. During measurement, the guard rings are biased at 3.3V to ensure stray photo-generated charge cannot be collected by the photo-diode. To verify correct operation measurements with and without the surrounding area blacked off from the incident light were compared. There was no difference between the two measurements — verifying that the guard rings were working.
- Pixel photo-currents are very small due to the tiny photo-diode area. In this work large area photo-diodes were used to provide a measurable signal in the pA-nA range depending on the light intensity and wavelength. The exposed diode active area was 400 by 400 μm

Figure 4.1 shows the design of the test structure.

¹The author would like to thank the Sensor Product Engineering and Technology groups of STMicroelectronics for assistance and useful discussions. Particularly Berend Meijer, Elaine Paris and Lindsay Grant. Thanks also to Clive Brown for test structure layout.

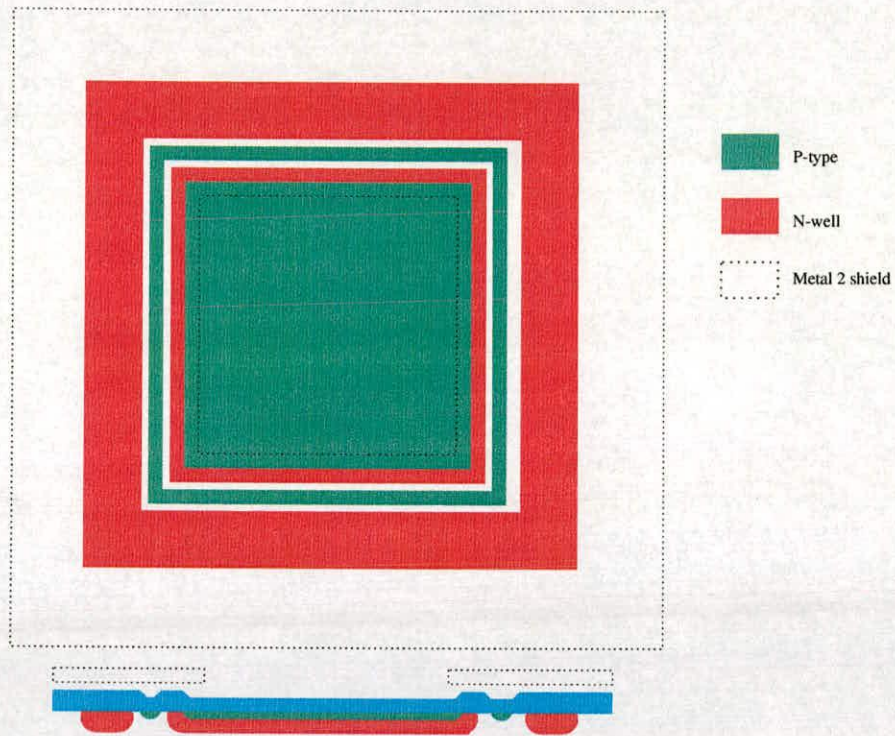


Figure 4.1: *Quantum efficiency measurement structure*

4.3 Measurement setup

The measurement setup consisted of the following:

1. A tungsten light-source powered from a low noise DC supply to avoid flicker.
2. This light source was fed through a calibrated monochromator to produce a narrow band beam of light. This monochromator was under computer control via an IEEE488 bus.
3. This beam of light illuminated either the photo-diode under test, or a calibrated radiometric photo-diode sensor with which the incident power at each measured wavelength could be measured.
4. The photo-diode or radiometric sensor were connected to the optometer, which in the case of the test photo-diodes recorded the current, or for the radiometric head the incident power in Wm^{-2} . The optometer was also controlled via the IEEE488 bus.
5. The whole setup was placed under infra-red and visible wavelength absorbing cloth to ensure only light from the monochromator illuminated the test device.

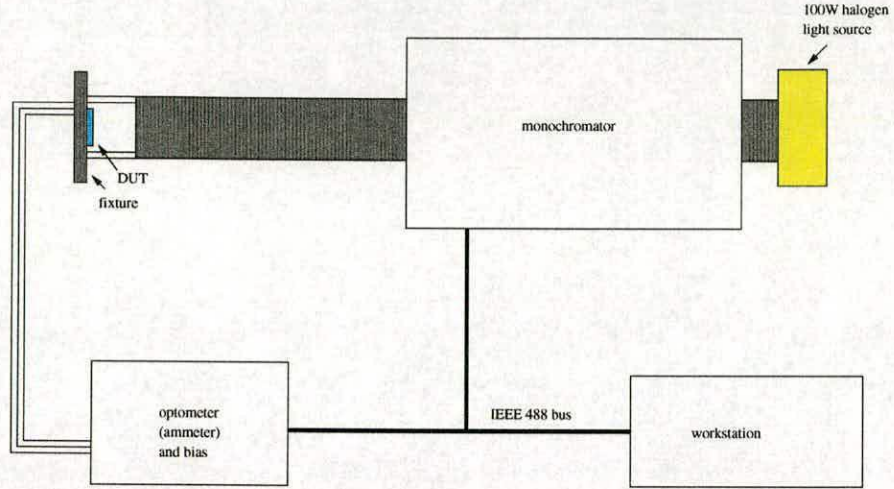


Figure 4.2: Quantum efficiency measurement setup

To produce a quantum efficiency curve, the wavelength was swept under computer control from 350 to 1050 nm with the spectral bandwidth at each step of 10nm. The light source is quite weak below 400 nm and data below this wavelength are less reliable. An average of 9 measurements was taken at each wavelength to reduce noise, but even so, at short wavelengths the data should be treated with scepticism as they could easily be affected by diode leakage, or external light entering the system.

To convert the measurements into quantum efficiency, the photo-current must be divided by the number of incident photons per second using the following equation:

$$QE = \frac{I_{PD} h \nu}{q A_{PD} P_{OPT}} \quad (4.1)$$

where I_{PD} is the measured photo-diode current, $h \nu$ is the energy of a single photon at the wavelength of the illumination (h being Plank's constant and ν being the photon frequency), A_{PD} is the exposed photo-diode area, q is the electronic charge, and P_{opt} is the incident optical power at the measurement wavelength in $W m^{-2}$.

4.4 Unfiltered results

First the raw results from the test structures without colour filters are presented. Measurements were made in two standard CMOS technologies, 0.35 μm and 0.5 μm .

4.4.1 0.35 μm technology

To provide a basis for comparison of the double junction quantum efficiency, the quantum efficiency of a standard N^+/P_{well} diode was measured (Fig. 4.3). The peak of the curve is around 500 nm, which is in the green region of the visible spectrum. In the violet and blue (400-500 nm) parts of the spectrum the response is much weaker, which will reduce the signal and hence image quality for blue pixels. Also, there is still a significant QE into the infra-red, which must be removed for consumer image sensors by using an infra-red blocking filter. The jagged peaks and troughs of the response are due to interference filter effects in the dielectric stack above the silicon, which is composed of multiple layers of different materials with various refractive indices.

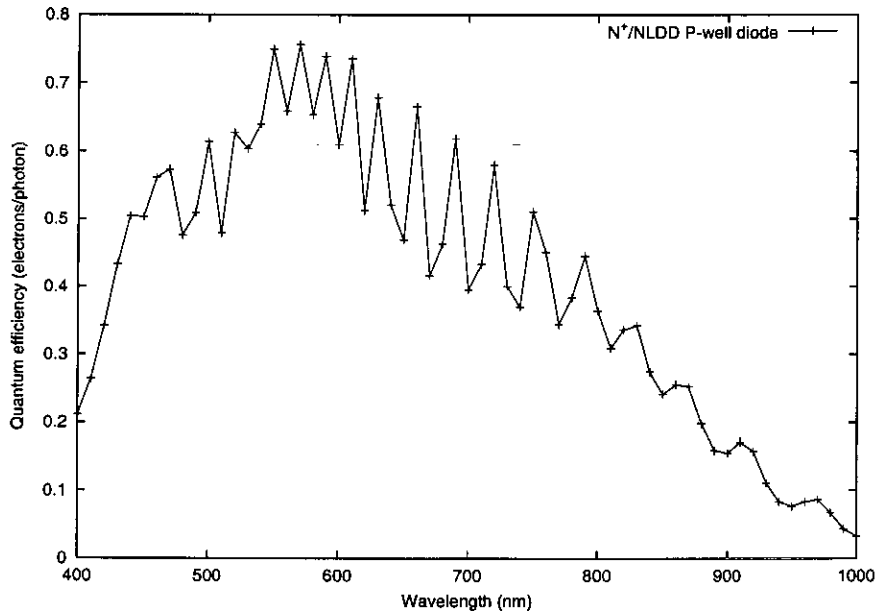


Figure 4.3: Quantum efficiency of a standard n^+/p_{well} diode.

Two variants of double junction structure were measured in this technology. The first used both the P^+ and PLDD implants to form the surface P-type region, the second used only the P^+ . A reverse bias of 3V was applied to both junctions during measurement. It can be seen in Figures 4.4-4.5 that there is no significant difference in the response between the two variants. The peak QE in both cases occurs for the N-well responses at around 550 nm. The QE is slightly lower than that of a standard n^+/p_{well} device, presumably as some of the light is absorbed instead by the P^+ layer. The p^+/n_{well} response has a much lower peak QE of around 40% which occurs at 450 nm. It is not a surprise that the p^+/n_{well} response is lower, as the junction is much more heavily doped and also shallower. Regarding the simulation results of

Chapter 3, there are some differences between the peaks and widths of the two responses. This is not really a surprise, as the simulations were carried out with default model coefficients, which clearly do not match the process parameters exactly. The effect of the dielectric stack is also not modelled in the simulation.

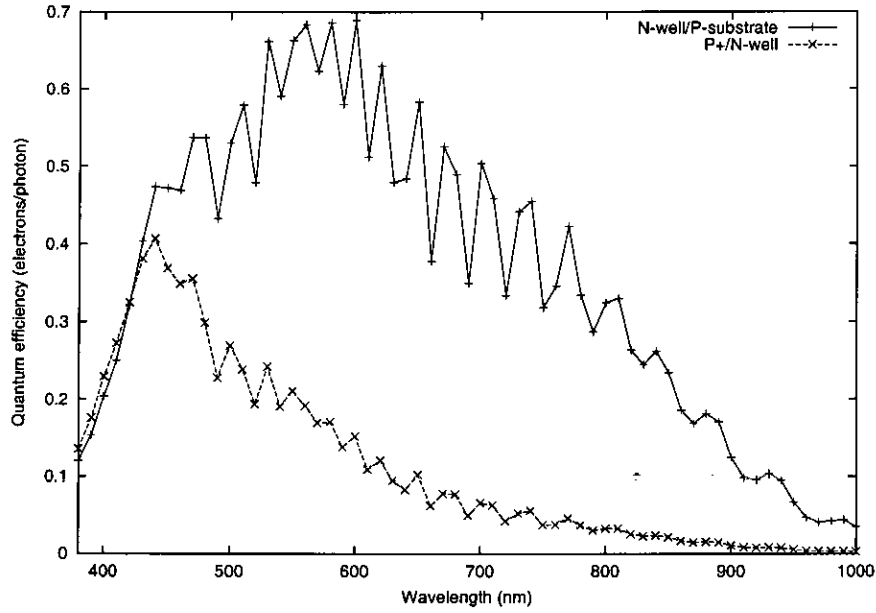


Figure 4.4: Quantum efficiency of a double junction structure implemented using P+/PLDD/N-well implants.

To emphasise the spectral selectivity of the two different responses, they have been normalised (Fig. 4.6). The spectral selectivity of the two junctions is much more apparent, though there is a considerable overlap which is not ideal. To compare with the TCAD simulations of Chapter 3, Figure 4.7 shows the measured and simulated normalised quantum efficiencies.

4.4.2 0.5 μm technology

Due to silicon availability, only one test diode was implemented in 0.5 μm technology. The structure used was unfortunately an earlier revision, and did not include guard rings. Incident light collection from outside the diode was prevented by manually masking off the silicon — leaving a central area of the diode exposed. Unfortunately, this meant that the exact dimensions of the exposed area was not known. Therefore, only normalised responses are shown (Fig. 4.8).

The responses are fairly similar to those obtained in 0.35 μm technology, though the $n_{\text{well}}/p_{\text{substrate}}$ response peaks at around 700 nm rather than 550 nm. This can be attributed to the deeper

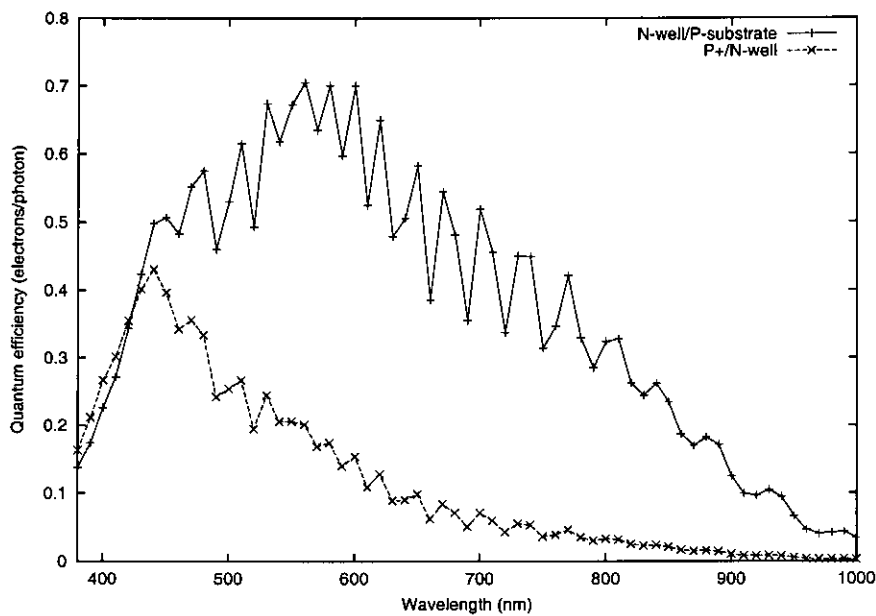


Figure 4.5: Quantum efficiency of a double junction structure implemented using P+/N-well implants.

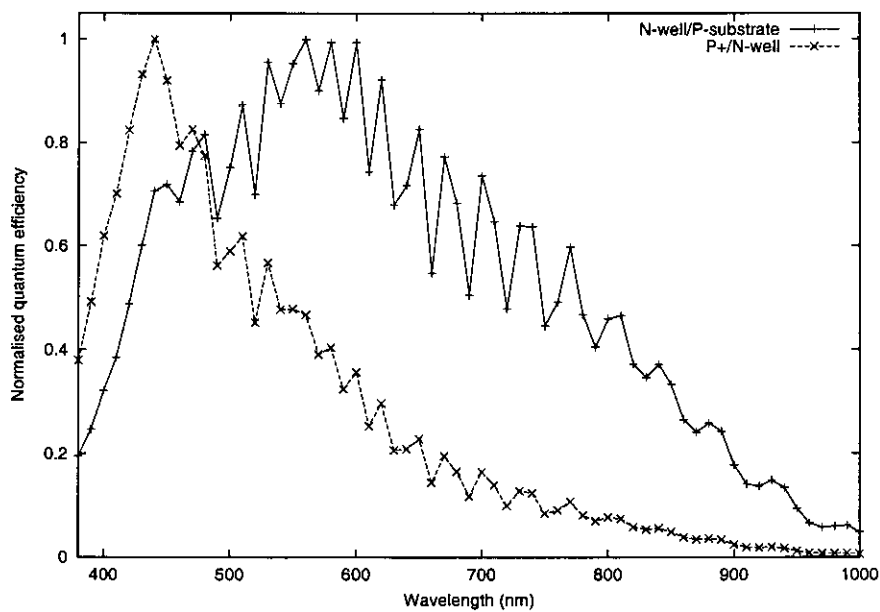


Figure 4.6: Normalised quantum efficiency of the P+/N-well test diode.

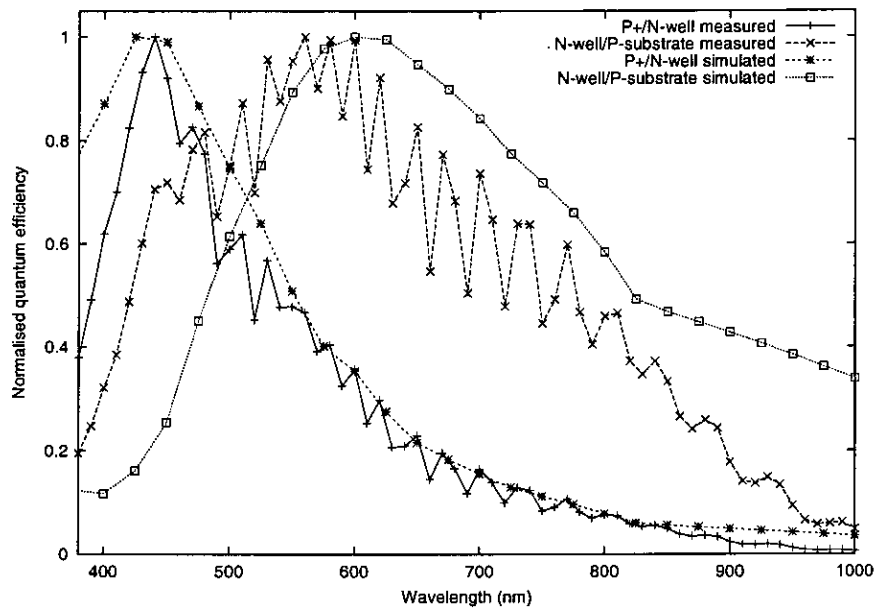


Figure 4.7: Comparison of simulated and measured normalised quantum efficiency.

junction depths of the larger geometry process (a similar result was observed in the device simulations). The peak of the top junction is in roughly the same place, 450 nm, as in the 0.35 μm results. However, if we compare the relative responses of the the two junctions at 550 nm which is the center of the visible spectrum, the responses overlap more, which suggests that the smaller geometry technology will have better spectral selectivity.

4.5 Results with filters

It is clear that to obtain enough responses for colour imaging, colour filters must be combined with the double junction structure. The spectral response was measured with magenta, green, cyan and yellow filters. It can be seen from Figures 4.9-4.10 that there are many combinations of filters which provide three or more responses with reasonable separation.

From an intuitive viewpoint, the set of responses which differ most seem likely to give the best performance. It can be seen for example in Figure 4.9 that the two green pixel responses are very similar — therefore not much information is gained by combining the two junction responses with a green filter. However, with a wider bandwidth colour filter such as cyan or yellow, significantly different responses from the two junctions are obtained which should result in improved colour discrimination. The comparison of colorimetric accuracy for different filter

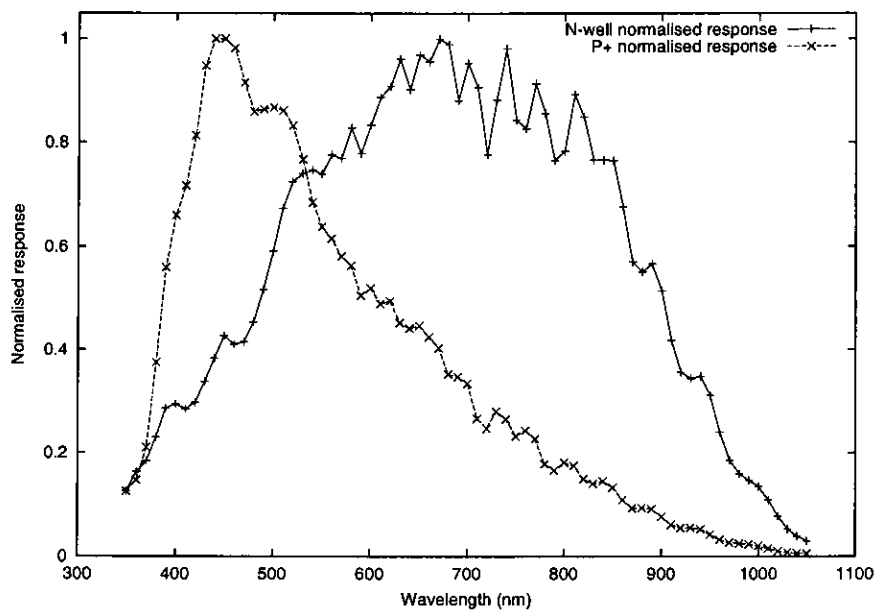


Figure 4.8: Normalised responses of the double junction structure implemented in 0.5 micron technology.

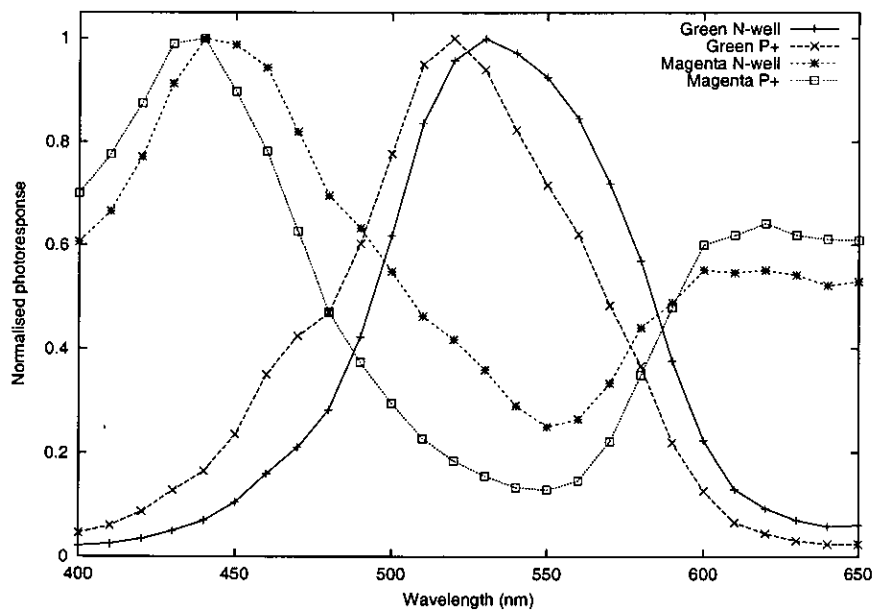


Figure 4.9: Normalised response with green and magenta filters.

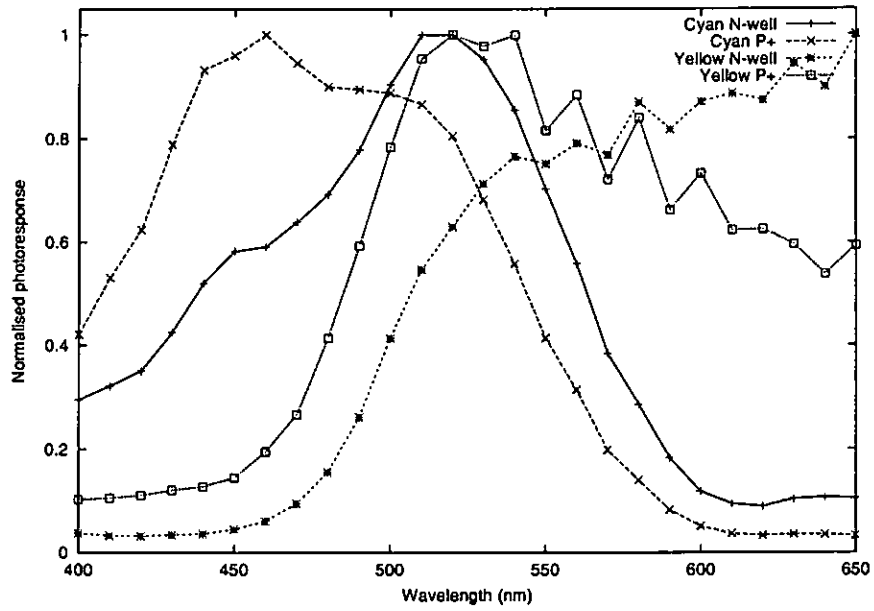


Figure 4.10: *Normalised response with cyan and yellow filters.*

combinations is given in Chapter 7. The use of wider bandwidth colour filters also has the advantage of increasing the sensitivity of the sensor, as more light is allowed through to the photo-diode.

4.6 Conclusion

This chapter has shown that the combination of the double junction structure with colour filters does indeed result in a sufficient number of spectral responses. It should be possible therefore, to use this structure with a reduced colour filter set in an image sensor. In the next chapter, the design of such a sensor is discussed.

Chapter 5

Sensor design

5.1 Introduction

In order to properly evaluate the performance of a double junction based image sensor such a sensor must be implemented and tested. In this chapter, the design of a DJ sensor is described. This can be split into two main sections - the design and layout of a single DJ active pixel, and the readout electronics necessary to pass the pixel signals to the outside world.

5.2 Double junction active pixel circuits

While operational amplifier based readout circuits can easily be made for a double junction photo-diode [42], the silicon area required prohibits the use of such circuits for imaging arrays. Instead, circuits with only a few transistors must be used, such as in the standard 3-transistor active pixel used in many CMOS image sensors today.

An obvious approach for a multi-junction pixel would be to use a logarithmic pixel. This approach has already been used in a linear array [42]. However, this approach suffers from the well known drawbacks of log pixels as described in section 2.4.5. In this work, as in most image sensors, integrating pixels are preferred due to their improved performance in typical imaging applications. Two suitable circuits have been devised for the DJ structure which attempt to minimise component count and hence pixel area.

5.2.1 Six transistor pixel

The first such circuit, shown in Figure 5.1, combines the DJ with two 3-transistor cells. The pixel is operated in a three step process as follows:

1. *Reset* is set high, charging V_{pN} to V_{rtn} and V_{pP} to V_{rtp} . When *reset* is released the integration period begins. kTC noise will be present at both nodes that were reset.

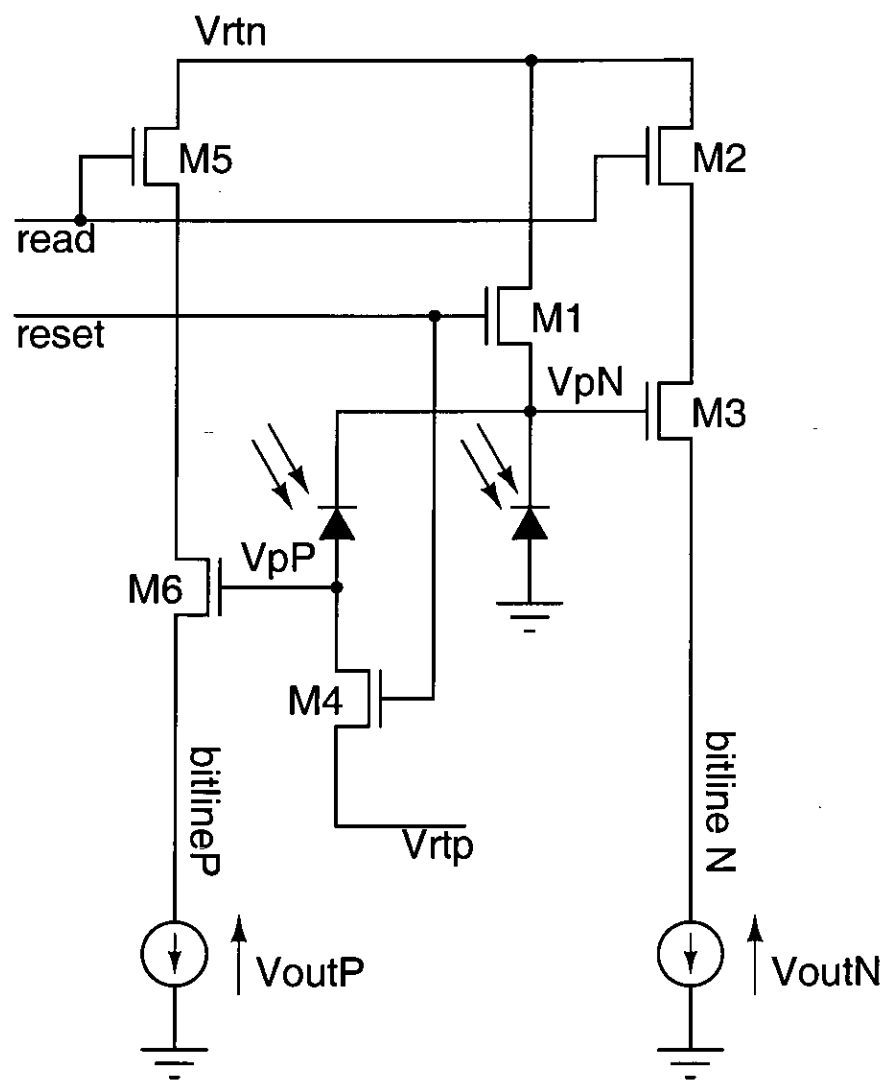


Figure 5.1: Six transistor active pixel circuit.

2. The photo-current through the p^+/n_{well} junction is integrated on the capacitance at V_{pP} and the photo-current in both junctions is integrated on V_{pN} . This causes V_{pP} to ramp up relative to V_{pN} and V_{pN} to ramp down relative to ground.
3. After a suitable integration period *read* is set high and the two integrated voltages are buffered through the source follower transistors M3 and M6 onto their respective bit-lines. The signals V_{outP} and V_{outN} may then be sampled by the columns and read out as required.

The process then repeats.

An ELDO simulation of the pixel operation is shown in Figure 5.2.

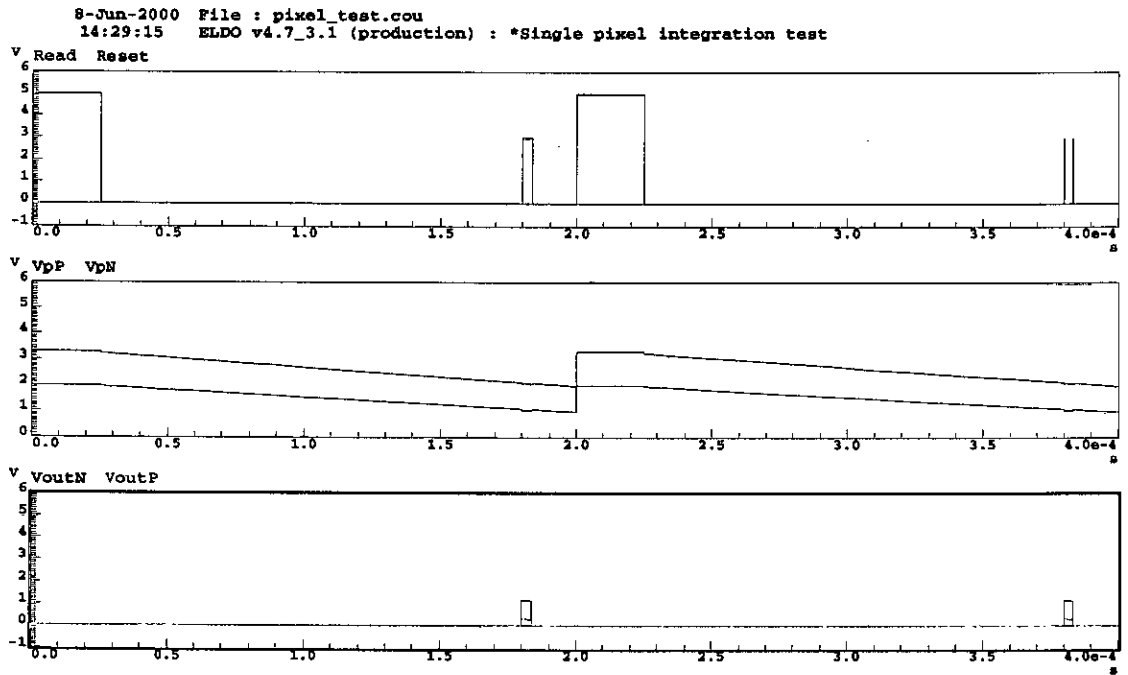


Figure 5.2: Operation of the six transistor active pixel circuit.

Several things about this pixel's operation should be noted:

- Neither the photo-currents integrated at each node nor the capacitance at each node are equal. Therefore the voltage after integration at V_{pN} will be:

$$V_{pN} = V_{rtn} - \frac{Q_{P+/Nwell} + Q_{Nwell/substrate}}{C_{VpN}} \quad (5.1)$$

where $Q_{P+/Nwell}$ and $Q_{Nwell/substrate}$ are the integrated photo-generated charges and

C_{VpN} is the capacitance on node VpN . This does not take into account the non-linearity of this capacitance which has a weak voltage dependence, or the reset noise.

In contrast the final voltage at VpP is:

$$VpP = VpN - VrtN - VrtP + \frac{Q_{P+/Nwell}}{C_{VpP}} \quad (5.2)$$

where C_{VpP} is the capacitance on node VpP .

This means that further processing must be done to recover the individual photo-charges that were integrated. Also the voltage on VpP is subject to twice the kTC noise of VpN .

- The voltage swing of VpP is limited, as both photo-diodes must remain reverse biased. If too long an integration time is chosen, or if the values of $VrtN$ and $VrtP$ are too close together, the two integrating nodes will collide and the device will begin to operate as a parasitic bipolar transistor. Thus these values must be chosen with care.
- An advantage of this pixel is that it requires only nMOS transistors and therefore lends itself easily to compact layout.

5.2.2 Eight transistor pixel

This active pixel topology attempts to hold the two photo-diode terminals at a constant potential by using common gate buffer transistors M1 and M5. M5 holds VpP at $V_{biasP} + V_{GSM5}$ and M1 holds VpN at $V_{biasN} - V_{GSM1}$ as long as both transistors are in saturation. The photo-currents are buffered through these two transistors and can be integrated on VbP and VnN . The reset-integrate-read cycle is identical to the 6-transistor pixel. However there are some key differences in operation:

- The reset voltage of VbP can be ground as a pMOS source follower is used to buffer the signal onto the bit-line.
- The integrating capacitances do not include the photo-diodes due to the common-gate buffer transistors. Therefore the voltage VbN can be expressed as:

$$VbN = Vrt - \frac{Q_{P+/Nwell} + Q_{Nwell/substrate}}{C_{VbN}} \quad (5.3)$$

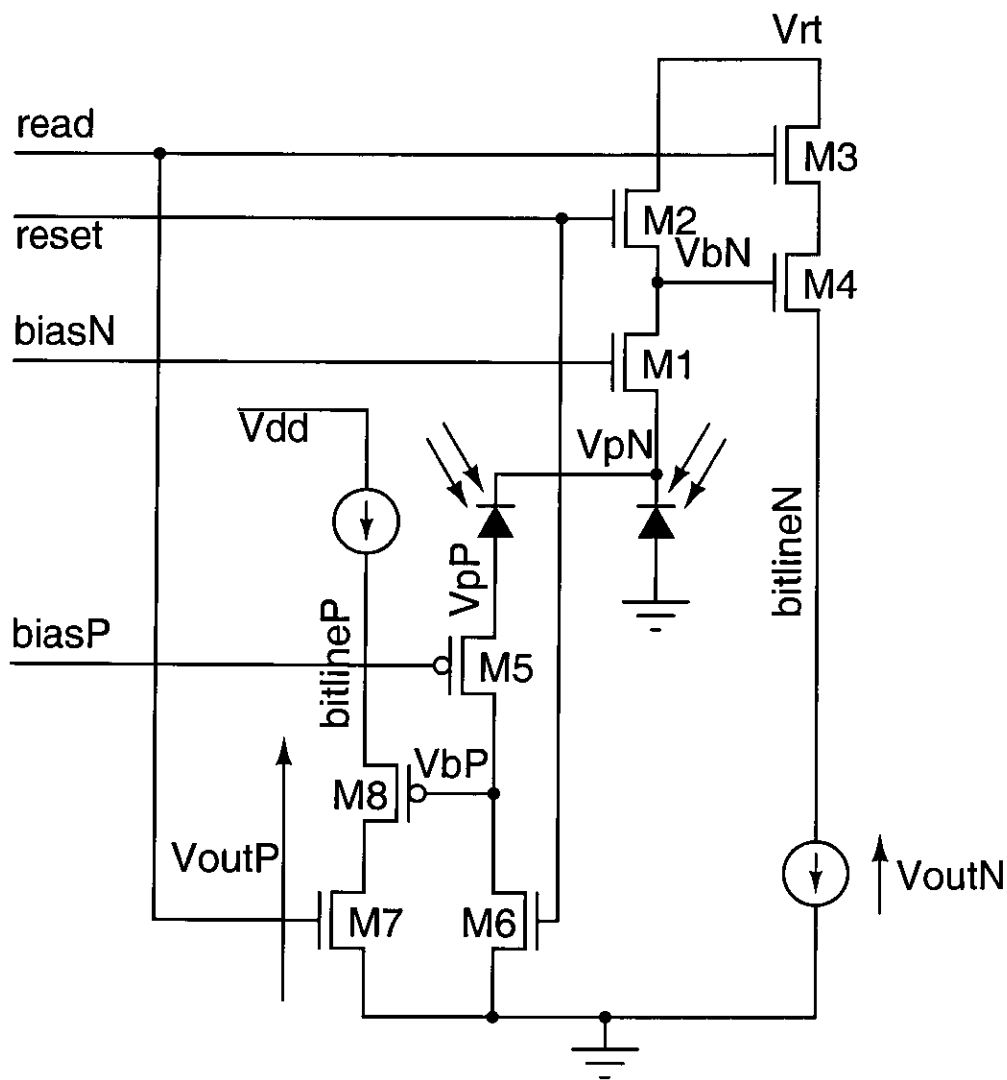


Figure 5.3: Eight transistor active pixel circuit.

where C_{VbN} is the capacitance on node VbN . Likewise, VbP is given by:

$$VbN = \frac{Q_{P+/Nwell}}{C_{VbP}} \quad (5.4)$$

where C_{VbP} is the capacitance at node VbP . Unlike the 6 transistor pixel, the voltage VbP is not dependent on VbN — this should simplify the signal processing. Additionally, the two ramp rates can be independently adjusted by varying the integrating capacitances (by changing the gate areas of M4 and M8). The \sqrt{kTC} noise charge caused by the reset of these nodes will also be smaller than in the 6T pixel, as the photo-diode capacitance is not included. This fact also increases the conversion gain of the pixel, which could aid readout at lower light levels. However, similarly to the 3T pixel with cascode transistor discussed in Section 2.4.3, this also introduces *lag*.

- The voltage swing of the two integrating nodes is limited in a different way, not because the junctions must be kept reverse biased, but by the requirement to keep M1 and M5 in saturation.

A very large disadvantage of this circuit is that it uses both pMOS and nMOS transistors, making compact layout very difficult. As will be seen in Section 5.4 the design rules enforce a large distance between N-wells. In section 5.4 the layout of both these pixels is investigated and compared.

5.3 Pixel noise analysis

It is best when analysing pixel noise performance to use the electron as the unit rather than the more usual unit of voltage. This is due to the fact the the input signal is photo-generated charge. Sources of noise after the pixel can be referred back and converted to charge for comparison with the input.

5.3.1 Factors limiting the signal

Saturation charge: In most active pixel circuits the photo-current is integrated on a capacitor.

The maximum photo-generated charge that can be collected is limited by the capacitance and the pixel voltage swing according to the very well known:

$$Q_{sat} = C_{pix} * V_{swing} \quad (5.5)$$

At high light levels this means that some of the incident light is wasted - limiting the peak SNR. In this analysis quantities are quoted in electrons by dividing Q_{sat} by the electronic charge q :

$$N_{sat} = \frac{Q_{sat}}{q} \quad (5.6)$$

This gives a saturation charge of $30000e^-$ with a 5 fF photo-diode capacitance and a 1 V swing, for example.

Quantum efficiency: The quantum efficiency of the photo-diode controls what proportion of the incident light is converted and collected by the photo-diode. A higher QE will improve the SNR up until the point that the saturation charge is reached. QE is clearly wavelength and photo-diode dependent. Therefore the overall number of electrons collected by the photo-diode before saturation is given by:

$$N_{int} = \frac{Q_{int}}{q} = \int_{\lambda_{start}}^{\lambda_{end}} n(\lambda)QE(\lambda)d\lambda \quad (5.7)$$

where λ_{start} and λ_{end} mark the beginning and end of the spectrum of the incident light, $n(\lambda)$ is the total number of photons incident onto the pixel at each wavelength, and $QE(\lambda)$ is the quantum efficiency at each wavelength.

Fill factor: The fill-factor is the proportion of the pixel area that is dedicated to the collection of incident light. This is not necessarily the same as the *photo-diode area* as micro-lenses can be added above the pixel to improve the effective light collection area. Also, charge generated in the silicon outside the photo-diode area may still diffuse to the photo-diode and be collected.

Pixel area: The area of the pixel combined with its QE and fill factor determines how much charge is integrated for a given incident photon flux. A bigger pixel will therefore produce a bigger signal with an improved SNR.

5.3.2 Sources of noise in active pixels

There are several sources of noise in active pixels:

Photon shot noise: The incident light on a pixel arrives in packets. Experimentally, the number of photons arriving in an observation window has been found to be Poisson distributed, with a variance equal to the mean arrival rate, and thus the photo-generated charge is subject to shot noise of value:

$$N_{\text{photon-shot}} = \sqrt{\frac{Q_{\text{int}}}{q}} \quad (5.8)$$

where Q_{int} is the integrated photo-current. This is the absolute minimum theoretical noise at a given light level, and means that even with no other sources of noise there will still be noise present in an image. In fact, at moderate to high light levels, this noise should dominate in a properly designed image sensor.

Reset noise: The reset of the pixel capacitance samples the transistor thermal noise. This noise depends only on the size of the capacitor. In a 3-transistor pixel this noise is not eliminated by correlated double sampling. In this analysis, we express all noise sources as charge and the reset noise in electrons given simply by:

$$N_{\text{reset}} = \frac{\sqrt{kTC}}{q} \quad (5.9)$$

where C is the capacitance being reset (usually the photo-diode). This noise is also often referred to as kTC noise. If correlated double sampling is used during read-out to remove the pixel offsets, two separate reset noises will be added.

Dark current: The dark current in a pixel generates noise that must be split into two categories: fixed and time varying. The fixed noise comes from the fact that the dark current is not constant across the pixel array — it therefore adds constant offsets to each pixel according to the exposure time. Fixed pattern noise is particularly noticeable in video (rather than still) applications. It can be expressed as:

$$N_{\text{dark-fpn}} = \frac{\sigma_{Q_{\text{dark}}}}{q} \quad (5.10)$$

where $\sigma_{Q_{dark}}$ is the standard deviation of the integrated dark current over the pixel array at a given temperature and exposure time. The second noise source is the shot noise caused by the dark current given in electrons by:

$$N_{dark-shot} = \sqrt{\frac{Q_{dark}}{q}} \quad (5.11)$$

where Q_{dark} is the integrated dark current charge.

Source follower thermal noise: This is the thermal noise of the source follower integrated over the output bandwidth referred back to the pixel. In this analysis a bandwidth of 1 MHz. has been assumed. The bandwidth is quite low, as the in-pixel source follower usually has to drive large sample and hold capacitors in the column. In actuality this noise source is very small and could reasonably be neglected. Increasing the source follower bias current reduces this noise component but increases power consumption.

There is also flicker noise present in the source follower – this too can be neglected if correlated double sampling is used as the slow moving noise voltage is cancelled.

5.3.3 Signal to noise ratio

Given the quantities from the previous two sections, the overall signal to noise ratio can be calculated:

$$SNR(dB) = 20 \log \frac{N_{int}}{\sqrt{N_{photon-shot}^2 + N_{dark-shot}^2 + N_{dark-fpn}^2 + 2N_{reset}^2}} \quad (5.12)$$

Time-varying and fixed noise sources in image sensors are often treated separately as the assumption is often made that the fixed offsets in a system can be cancelled. However, in truth this is often not the case without a large additional cost. To cancel the dark current offset for example, requires a frame store the same size as the pixel array and a shutter.

In a still image, FPN is indistinguishable from the temporal noise sources, so in this analysis they are lumped together as an RMS sum. In video applications, more weight should be given to the fixed noise sources, as the eye is better at perceiving fixed offsets in an image due to its

natural averaging action.

In an image sensor, noise is also contributed from the readout circuitry. Sample and hold capacitors that are used for CDS will contribute kTC noise, A-D conversion will add quantisation noise, analogue gain will add thermally generated noise in the amplifier. In a well designed sensor, these noise sources should be small compared to the those in the pixel but they will still degrade the SNR at low light levels. These noise sources are not modelled in this analysis as the purpose of this section is to evaluate the pixel performance alone.

5.3.4 Results of analysis

Using the equations above the the SNR at various light levels can be calculated as the pixel parameters are varied. Industry generally quotes SNR with the noise calculated at half of the signal level — a form of spec-man-ship used to increase the numbers by just under 3 dB. Despite this, this measure has been used here as it is prevalent in the real world. This modifies equation 5.12 to:

$$SNR_{dB} = 20 \log \frac{N_{int}}{\sqrt{\frac{N_{photon-shot}^2}{2} + N_{dark-shot}^2 + N_{dark-fpn}^2 + 2N_{reset}^2}} \quad (5.13)$$

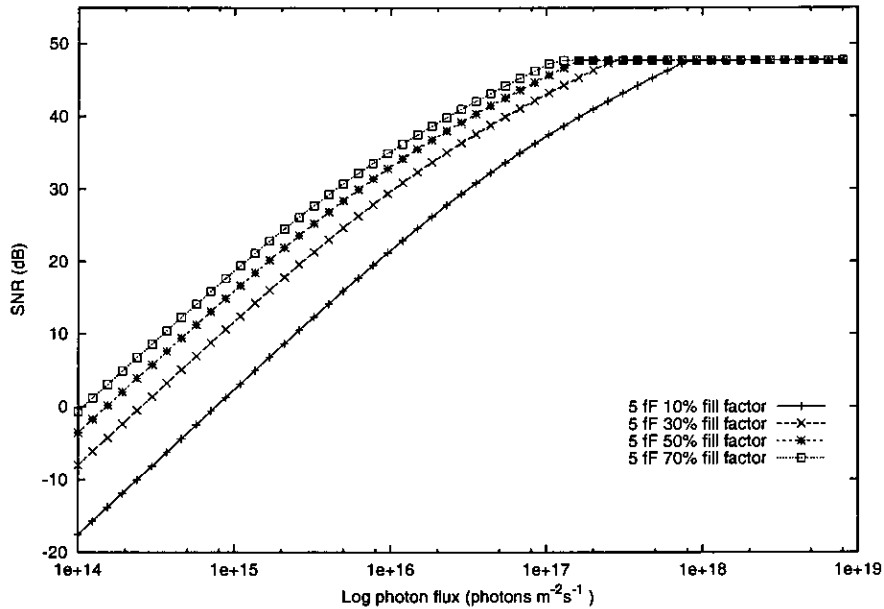


Figure 5.4: Calculated SNR at 50% noise vs. photon flux for a 5 fF pixel.

Figure 5.4 shows how noise performance (and hence image quality) varies as the pixel-fill factor improves. The curves were calculated for a 5 fF pixel capacitance with a dark current of 100 pA cm^{-2} . A $6.8 \text{ }\mu\text{m}$ pixel pitch was used for the 3T cell. This dark current and pixel size is comparable to that reached by commercial CMOS imager developers such as in [73]. It can be seen that increasing the fill-factor is a sure way of improving performance. However, this does not necessitate improving the photo-diode fill-factor — it can be achieved by using micro-lenses.

At low light levels, the pixel kTC noise can become more significant. Reducing the capacitance reduces this noise source and improves low light performance at the expense of reduced saturation charge. The lost saturation charge can be recovered by increasing the pixel voltage swing, either by increasing the power supply voltage or by using low V_T transistors in the pixel.

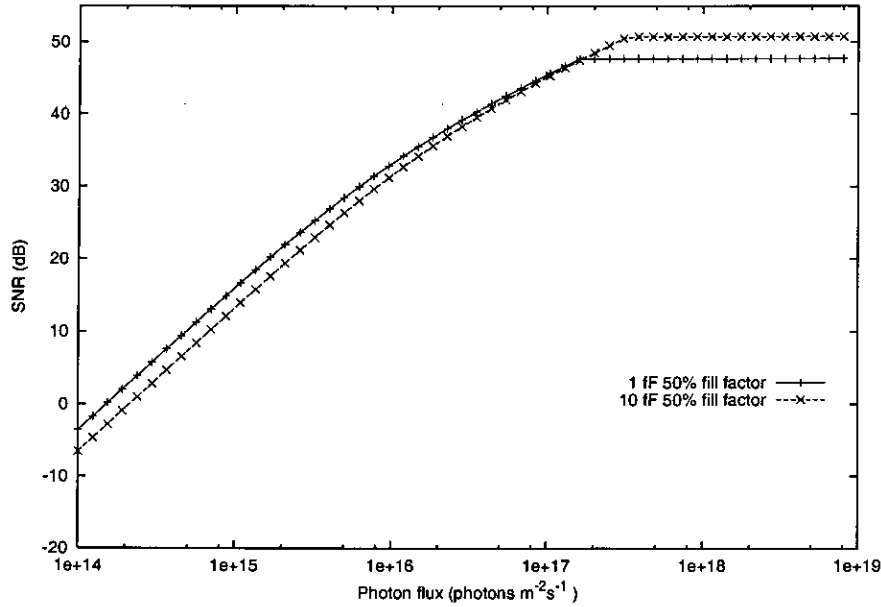


Figure 5.5: *Calculated SNR at 50% noise vs. pixel capacitance.*

So, for a 3 transistor pixel with low dark current, a large voltage swing and a small pixel capacitance with high fill-factor micro-lenses should be optimum. It will give good low light performance and a high SNR at saturation. Of course, other technological improvements, such as moving to a 4 transistor pixel with a pinned photo-diode can also improve performance. Producing a pinned DJ structure is impossible however, which rules out this approach in this project. Figure 5.6 shows a more complete picture of the incremental gains that can be made through modification to pixel design and technology improvements.

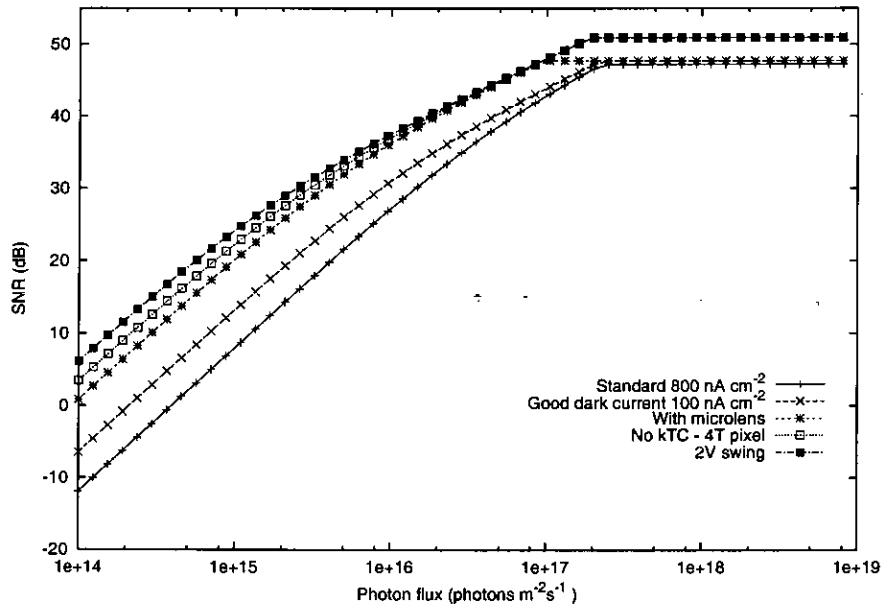


Figure 5.6: Calculated SNR at 50% noise vs. pixel generation. Starting with a $5f$ pixel with 30% fill-factor and 800 nA cm^{-2} dark current, process improvements result in a 100 nA cm^{-2} dark current, the microlenses are added to increase the light-collecting area to 70%. Next, a 4T pixel is used to eliminate kTC noise, and finally the voltage swing is doubled to 2V to improve peak SNR.

The DJ pixel is larger and hence with the addition of micro-lenses can collect more light than a smaller 3-transistor pixel. Figure 5.7 shows the calculated SNR for a DJ pixel. The theoretical maximum for a noise-less 6.8 μm pixel with 100% fill-factor is also given. (A 6.8 μm pixel occupies exactly half the area of a 9.6 μm double junction, which therefore results in the same number of spectral samples per unit area.) The SNR in this case is limited by the shot noise only, and exhibits a slope of 10 dB per decade of light intensity due to the square root relationship between shot noise and incident photons. In this calculation p^+/n_{well} and $n_{\text{well}}/p_{\text{substrate}}$ capacitances of 10 fF and 8fF respectively were used. Dark current density was kept the same for all photo-diodes as was the micro-lens fill-factor of 70%. In fact, it is likely that a better micro-lens fill-factor would be achieved with the larger pixel size as this factor is limited by the minimum space between micro-lenses. The $n_{\text{well}}/p_{\text{substrate}}$ QE was set at 65% and the p^+/n_{well} QE at 40%, compared with the 3T cell value of 75% (see chapter 4). The voltage swing for the p^+/n_{well} and $n_{\text{well}}/p_{\text{substrate}}$ junctions was 0.5V and 1V respectively.

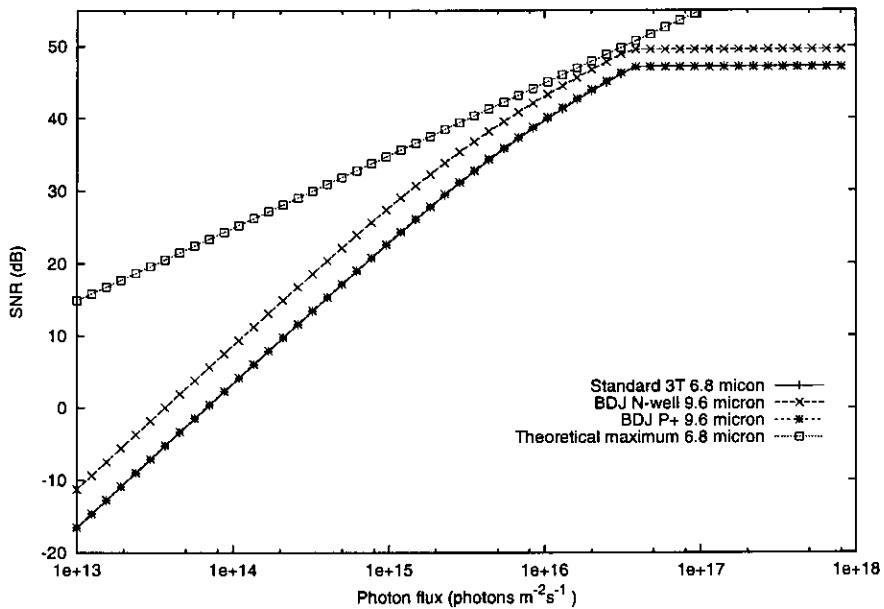


Figure 5.7: Calculated SNR at 50% noise for DJ and 3T cells. At some light levels the $n_{\text{well}}/p_{\text{substrate}}$ DJ SNR is very close to the absolute maximum possible at 6.8 microns due to its larger light collecting area and at all light levels is better than the standard 5fF 3T cell. Note the the 6.8 μm 3T and 9.6 μm DJ p^+/n_{well} curves are overlaid.

The 3-transistor pixel does not perform as well as the $n_{\text{well}}/p_{\text{substrate}}$ DJ photo-diode in this analysis, purely because of the larger light collecting area of the double junction pixel. The p^+/n_{well} results are very similar. This is despite having a higher kTC noise component and

much lower quantum efficiency in the p^+/n_{well} photo-diode.

5.4 Pixel layout

5.4.1 6-T pixel

A pixel pitch of $9.6\ \mu m$ was chosen to maintain compatibility with existing designs. The $9.6\ \mu m$ pixel allows a column readout cell size of $4.8\ \mu m$ to be used, as two signals are obtained from each pixel. The minimum practical column width for this manufacturing process is $4.6\ \mu m$, set by the pitch of two transistors side by side. Figure 5.8 shows a pixel laid out to this dimension.

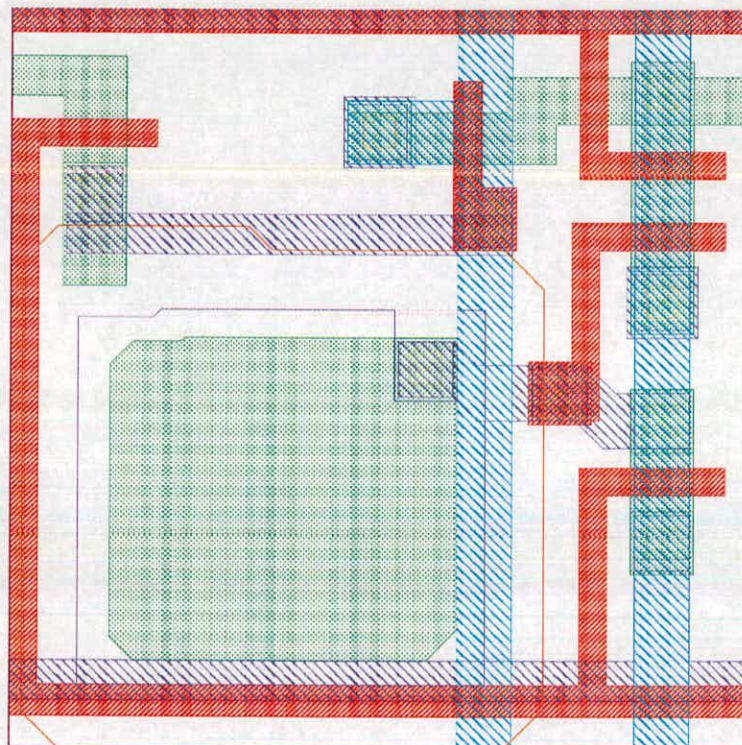


Figure 5.8: Layout of the 9.6 by 9.6 micron pixel

Legitimate questions may of course be asked about the suitability of this pixel pitch given the $0.35\ \mu m$ process used. When designing an active pixel, a small pitch is desirable, as long as it does not compromise the active area and noise performance too much. Figure 5.9 shows the relationship between the pixel size and the maximum achievable fill-factor when limited only by the N-well and active spacing design rules for the chosen technology. This does not take into

account the transistors required to make the pixel function, but it can be seen from the figure that the achieved fill-factor is 61.5% of the maximum at the chosen pitch.

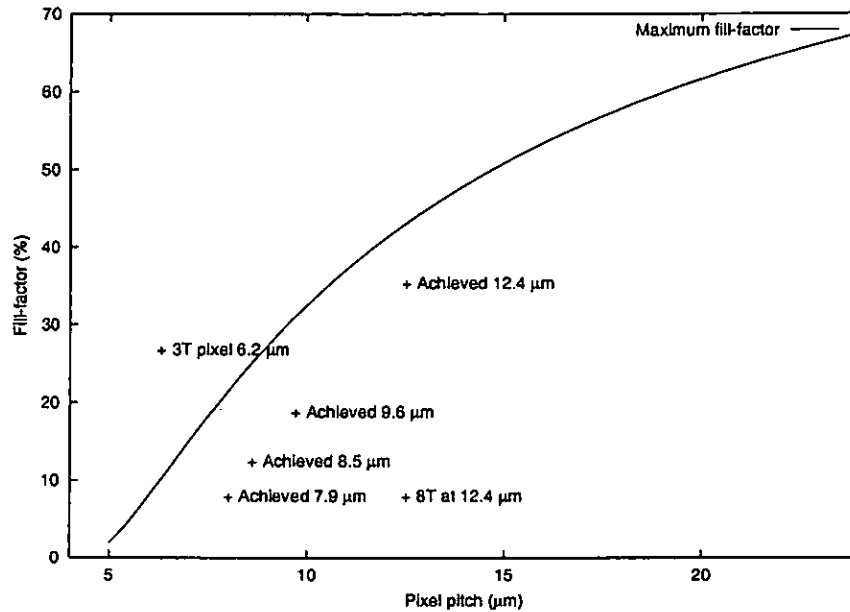


Figure 5.9: Maximum fill-factor vs. pixel pitch for the chosen 0.35 micron technology. The achieved fill-factor for 12.4, 9.6, 8.5 and 7.9 micron 6T pixels is also shown. A 3T active pixel naturally achieves a better fill factor as less transistors are required. The fill-factor of the 8T 12.4 micron cell is very poor.

However, the analysis of Section 5.3 has shown that what really matters to pixel performance is not fill-factor but the total light collecting area. If micro-lenses are used, then the photo-diode active area does not determine the light collecting area. There is, therefore, a case to be made for choosing the photo-diode area to achieve the desired *capacitance* and so saturation charge and reset noise. The active area limit as the pixel pitch is varied is given in Figure 5.10. The active-area of the DJ pixel is slightly larger than that of a 6.2μm 3T cell.

Referring to the pixel layout shown in Figure 5.8, the photo-diode (p^+) active area is 17.3 μm^2 which is 19% of the total area. If micro-lenses were used the optical fill-factor would be increased significantly.

Several other pixel layouts are shown in Figures 5.11-5.13. At a pitch of 12.4 μm all the transistors can be laid out in a strip, which results in an elegant layout with a high fill-factor of 35.5% (an active area of 56 μm^2 which is 83 % of the maximum). The pixel pitch is too large for higher resolution arrays, however. As the pixel pitch decreases the transistors must be laid out in an L-shape, which dramatically reduces the possible fill-factor. It can be seen that, as the

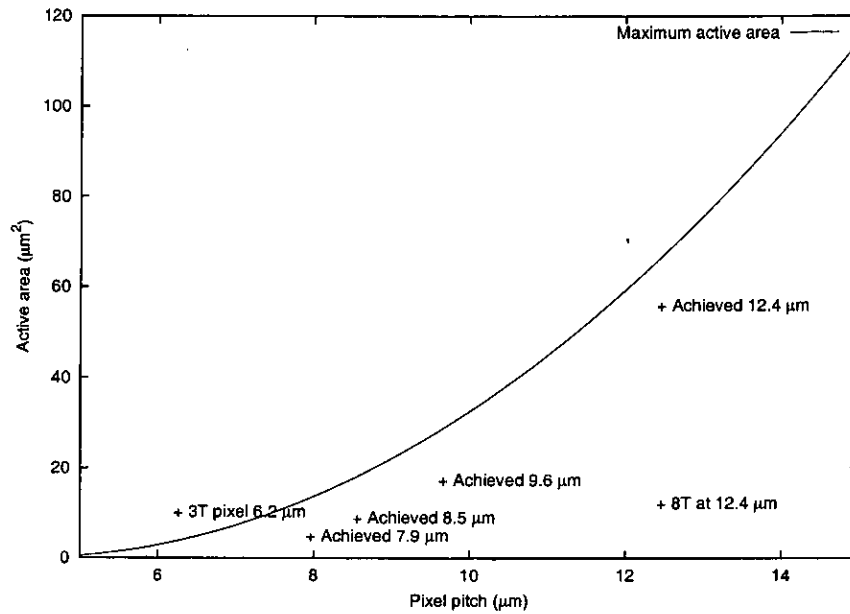


Figure 5.10: Maximum active-area vs. pixel pitch for the chosen 0.35 micron technology. Four double junction pixels are also shown along with a 3T cell. It can be seen that the active areas of the 3T cell and the 9.6 micron double junction cell are comparable.

pitch decreases towards $7.9 \mu m$, the active area and fill-factor start to decrease rapidly. It seems that a reasonable compromise is around the $9 \mu m$ mark.

5.4.2 8-T pixel

It was stated in Section 5.2.2 that the layout of the eight transistor pixel was likely to be too large. Figure 5.14 shows the layout of this pixel at a $12.4 \mu m$ pitch. It can be seen that the fill-factor and active-area of this pixel relative to the 6-T one is very poor (Fig. 5.9-5.10).

The requirement for pMOS transistors in the 8-T pixel means that two extra n_{well} to p^+ spacings are required. This dramatically reduces the area of the photo-diode — in this case it is only $12.2 \mu m^2$. Even if this were acceptable, the pixel pitch of $12.4 \mu m$ is too large for reasonably sized arrays. There is not much scope for reducing the pixel pitch and maintaining a usable active area without process optimisation to reduce the N-well spacings in the pixel.

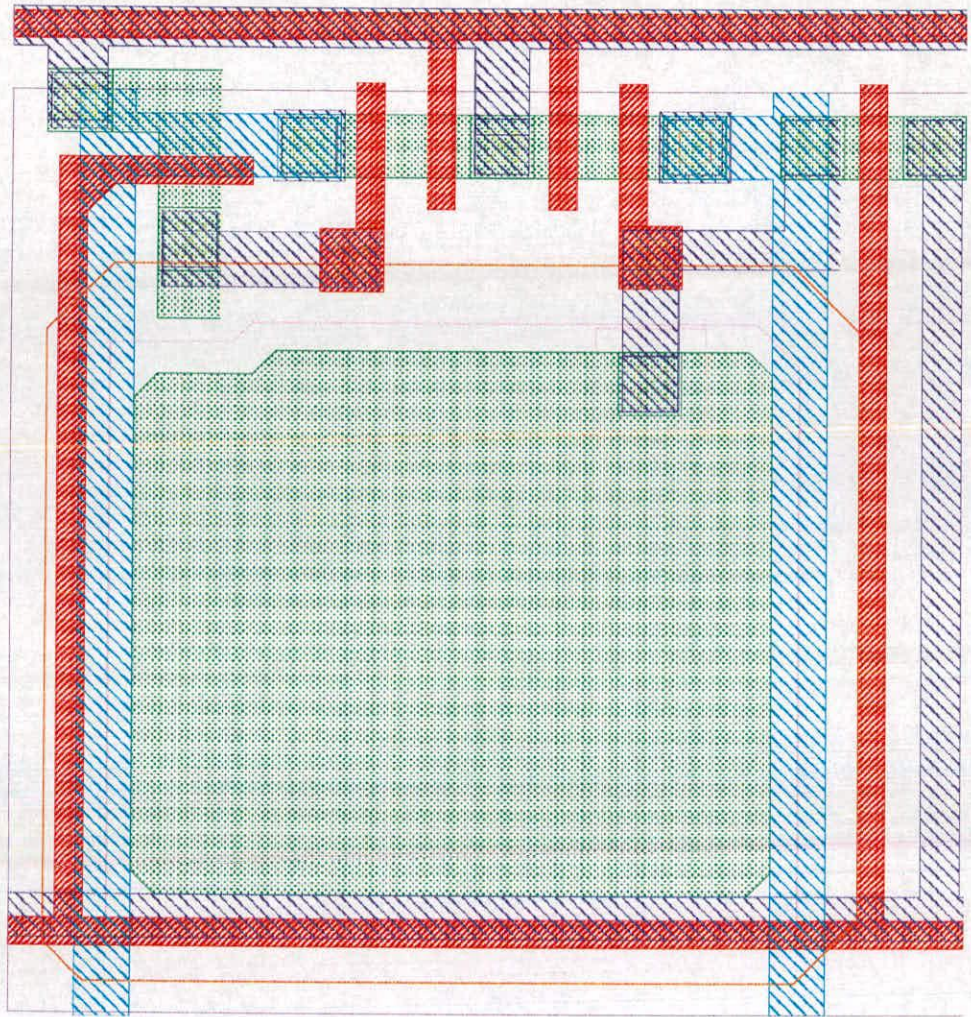


Figure 5.11: *Layout of the 12.4 by 12.4 micron pixel.*

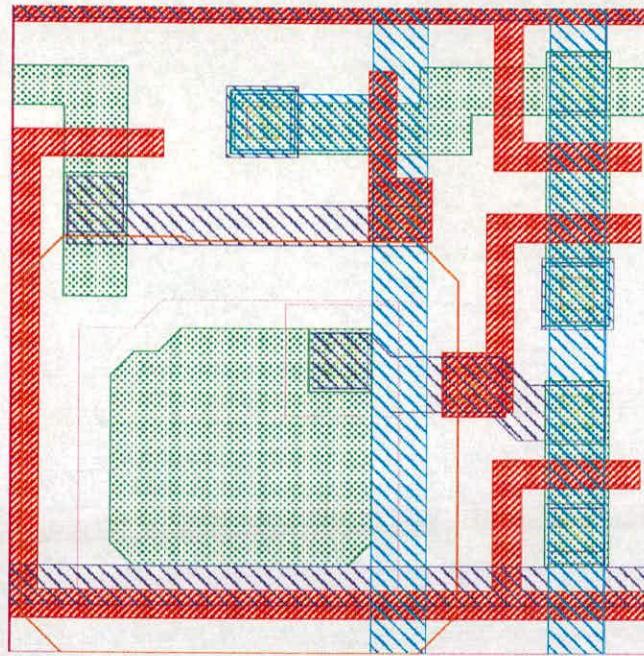


Figure 5.12: *Layout of the 8.5 by 8.5 micron pixel*

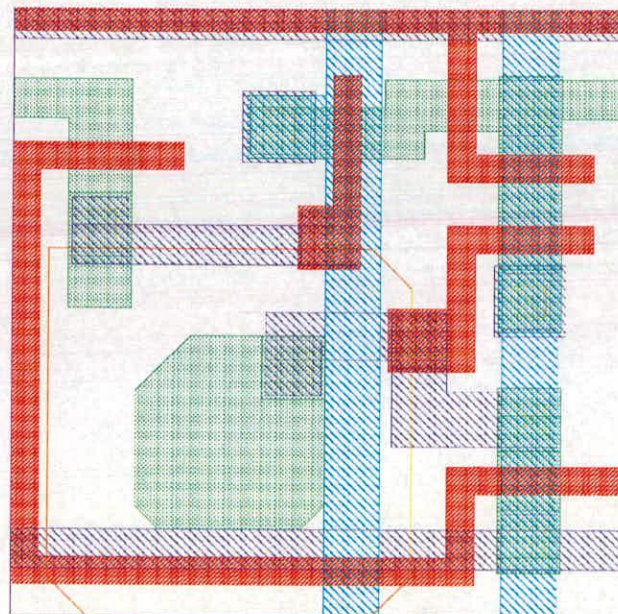


Figure 5.13: *Layout of the 7.9 by 7.9 micron pixel*

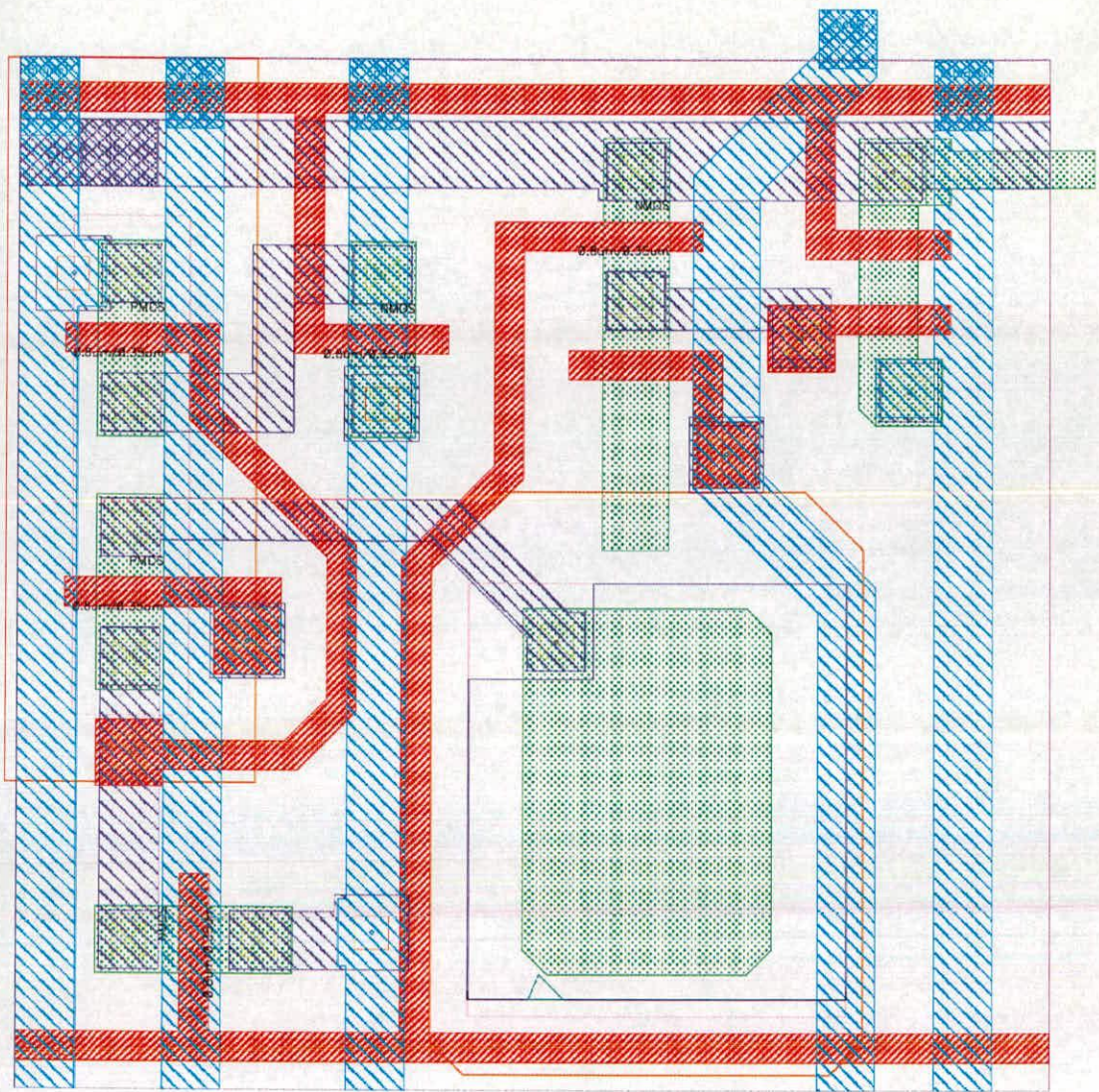


Figure 5.14: Layout of the 8-T pixel.

5.5 Sensor overview

The sensor was based closely on an existing STMicroelectronics research device intended primarily to test pixel variants ¹. Compatibility with existing test boards and software was maintained. The high level sensor architecture is shown in Figure 5.15. It is very similar to many analogue readout active pixel image sensors.

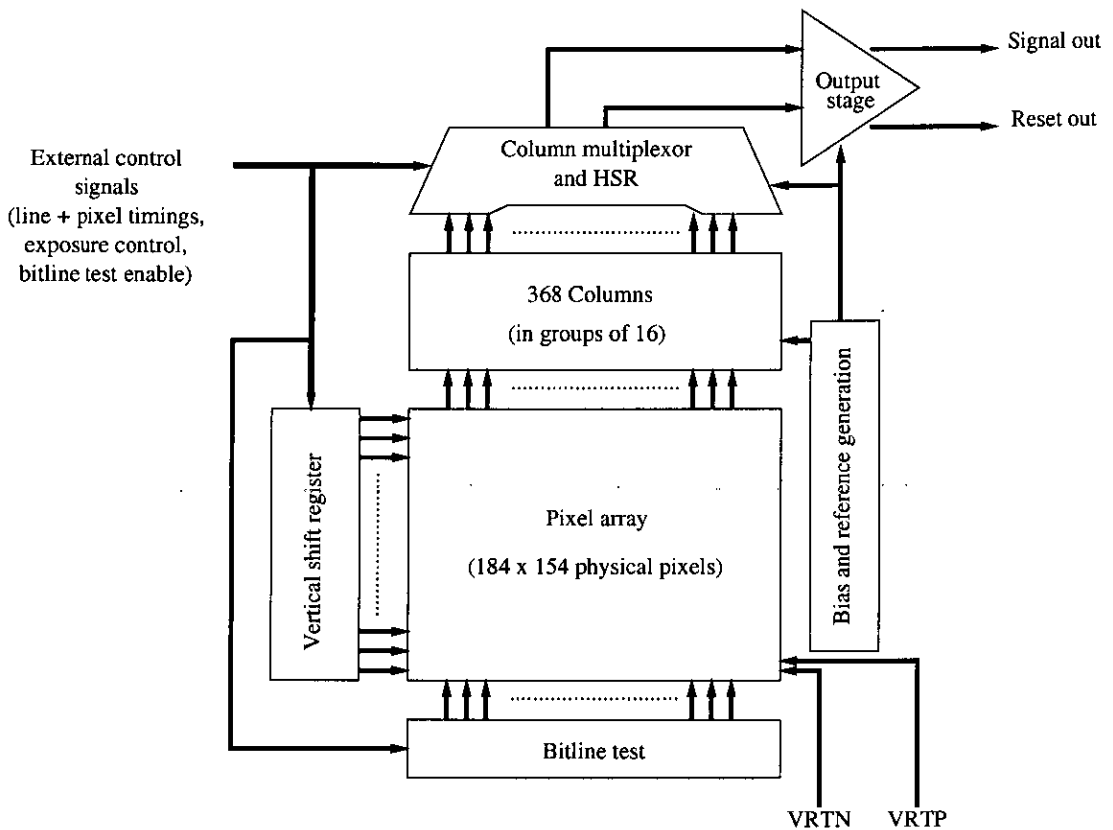


Figure 5.15: Overview of DJ sensor architecture.

Key elements of the sensor are:

Vertical shift register: This controls the reset and read signals to each row of pixels. The externally supplied line timings are used to clock this shift register and control the exposure (integration time) of each pixel. The length of the integration period is set by the space (in rows) between the reset and read pulses as they travel up the shift register.

¹The author would like to acknowledge and thank the design team that worked on the original version of this device — Toby Bailey, Drew Holmes, Dave Poyner, Clive Brown and Lindsay Grant. The information on the sensor architecture and design in this chapter is not meant to be a claim of original work. It is included for a complete description of the whole project.

Horizontal shift register: This controls the multiplexing of each of the stored column signals in turn onto the final output bus.

Column sample and hold and buffer: Each row of pixels is sampled at read and reset time onto two storage capacitors per column (Fig. 5.16). The timing of the sample-and-hold is controlled from outside the device, again with the external line timings. The sampled signals are then buffered onto a horizontal bus, and then finally off-chip.

Output stage: Both the reset and read value for each column are driven off chip using two matched source followers.

Bit-line test circuitry: The bit-line test circuitry clamps the alternate bit-lines to white and black levels. This allows the output signal chain to be tested independently from the pixel array.

5.5.1 Output signal chain

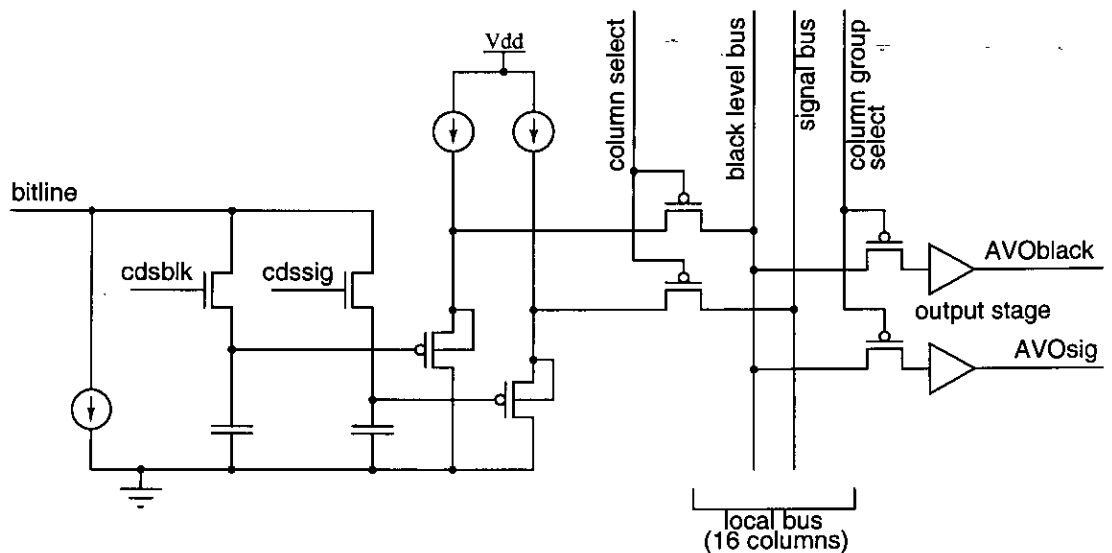


Figure 5.16: Schematic of the column and output stage structure.

It can be seen in Figure 5.16 that the signal from the photo-diode to the output passes through three source-follower stages: the in-pixel source follower (only the current source is shown in the figure), an in-column pMOS source follower, and the output buffer that drives the signals off-chip (which is also a source follower). Each of these source-followers has a gain of less than unity and also a non-linear component [97] which means that, when referring output data back to the pixel photo-diode, this must be corrected for.

Multiple source followers are required, as the load capacitance increases through the signal chain. The load that the column source follower has to drive is reduced by the use of a local bus which splits the columns across the array into groups of sixteen. This means that the column source follower only sees a load of sixteen columns plus the group select switches and output bus instead of that of the total of all the columns. For the interested reader, this approach is described in detail by Loinaz [7].

5.5.2 Verification

A thorough verification of the design was performed. To reduce processing time, a reduced array size of 32×16 was used in the system simulation (from schematics). Despite this, to simulate the readout of a complete frame with Eldo took approximately 3 days of processor time on a Sun Ultra 60 workstation.

As it was therefore impossible to simulate the full image sensor, the physical layout had to be carefully validated by LVS (automatically comparing the layout with the full-sized schematics). A complete design rule check was also run on the final mask data.

5.6 Conclusions

This chapter has analysed the trade-offs to be made in the design of a double junction active pixel. One of the major trade-offs is between pixel size and the ease of reading and controlling the integration of the pixels. Although the 8T cell has the benefits of increased conversion gain and easier read-out due to the two independent output voltages, for most array sizes, the cell size would be far too large, due to the extra N-wells required.

By adopting the 6-transistor pixel, the cell area can be minimised and a respectable active area achieved. A more stringent control over exposure must be enforced however to prevent the photo-junction voltages from colliding.

Noise analysis has shown that (with micro-lenses) the larger double junction pixel has good performance relative to the standard pixel due mainly to the larger light collecting area.

Finally, the architecture and design of a simple image sensor employing the 6-transistor pixel was described. A micro-graph of the chip is shown in Figure 5.17. Devices assembled from

the first silicon functioned as expected, thanks most probably to a rigorous verification of the design.

In the next chapter, the test methodology and results from the prototype sensor are presented.

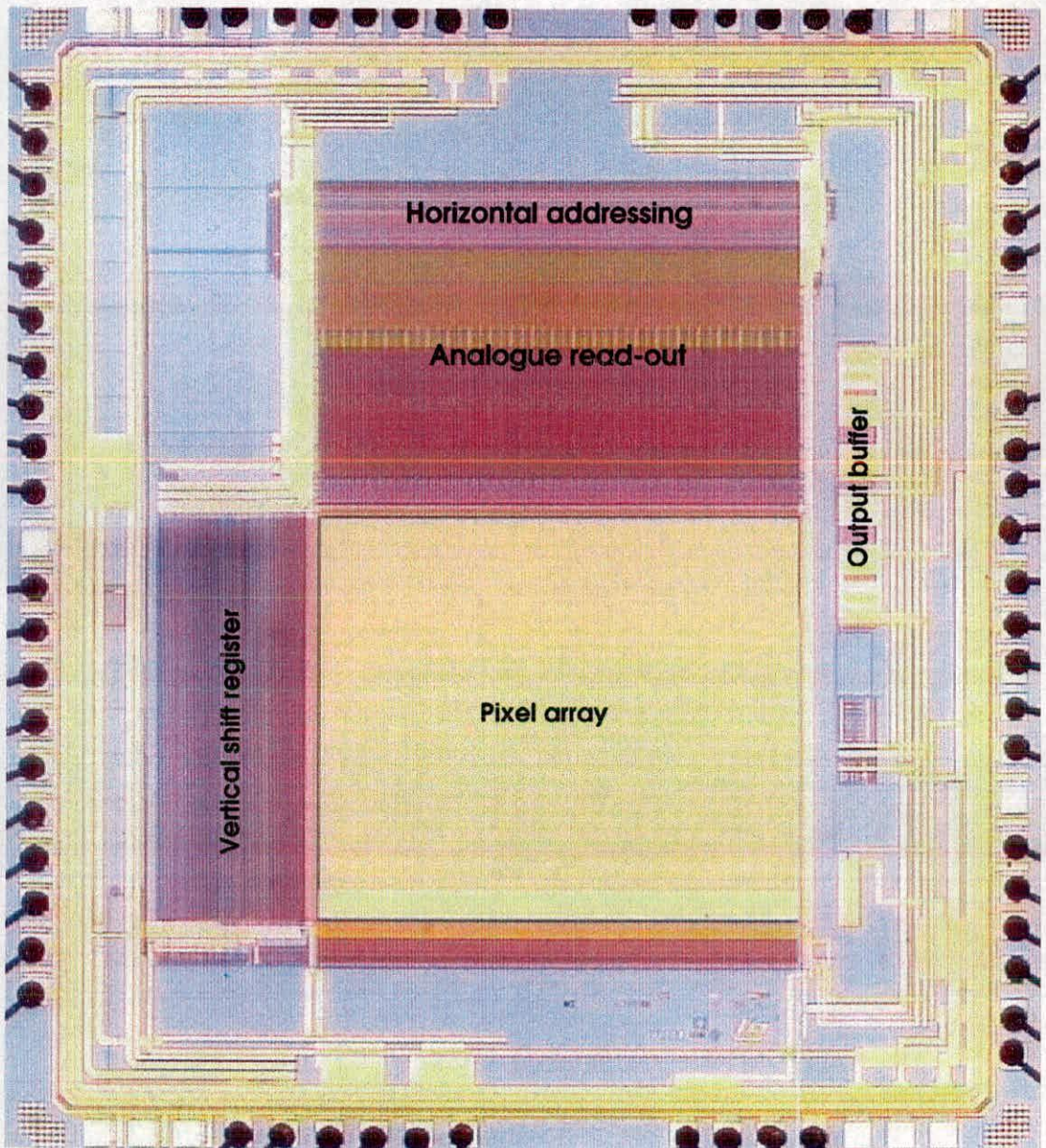


Figure 5.17: *Micro-graph of the image sensor.*

Chapter 6

Sensor characterisation

6.1 Introduction

In the previous chapter, the design of a double junction active pixel image sensor was described. The low-level noise performance, sensitivity, and cross-talk of the sensor determine the ultimate image quality that can be obtained. In this section the methodology for the measurement of these parameters and the results of the measurements are given.

6.2 Noise as a measurement tool

The noise in an image can be used to determine many parameters including full-well capacity and conversion gain. The theory and methodology has been described in [98][99] but will be briefly reviewed here.

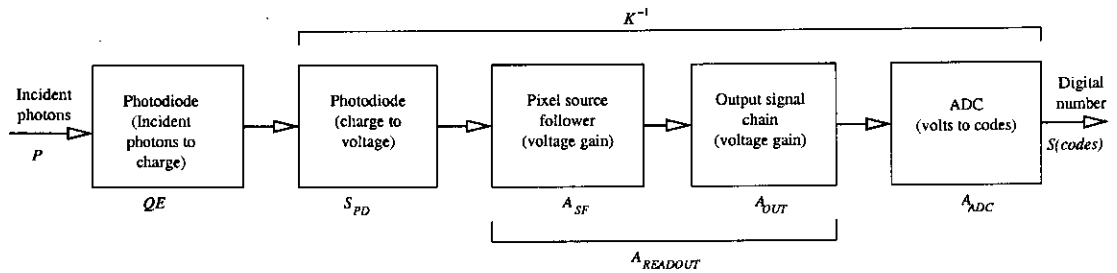


Figure 6.1: Diagram of the signal chain of a camera system from incident photons to digital output.

For a given number of photons P per pixel the signal output from the analogue-to-digital converter will be:

$$S(\text{codes}) = P \times QE \times K^{-1} \quad (6.1)$$

where QE is the quantum efficiency of the pixel, and K is the inverse conversion gain from the photo-diode to the output of the ADC (in e^-/code). This is shown pictorially in Figure 6.1. If

the image sensor noise is partitioned between signal dependent, and signal independent noise, the total noise σ_i^2 in the image can be expressed as:

$$\sigma_i^2(\text{codes}) = \left(\frac{\sigma_{PQE}}{K}\right)^2 + \sigma_R^2(\text{codes}) \quad (6.2)$$

where σ_R^2 is the read noise of the sensor (the temporal noise floor), and σ_{PQE} is the photon shot noise in the pixel. The two noise variances are independent of each other. The term $\left(\frac{\sigma_{PQE}}{K}\right)^2$ is the photon shot noise multiplied by the gain from the photo-diode to the ADC, and σ_R^2 is all the other noise sources of the sensor (reset noise, read-out noise, dark current noise) which are independent of the light level. As $\sigma_{PQE}^2 = KS(\text{codes})$ due to photon shot noise statistics, the constant K can therefore be written as:

$$K = \frac{S(\text{codes})}{\sigma_i^2(\text{codes}) - \sigma_R^2(\text{codes})} \quad (6.3)$$

By determining the constant K , many pixel and sensor parameters can be inferred. It can be seen from the above figure that:

$$K = (S_{PD} \times A_{SF} \times A_{OUT} \times A_{ADC})^{-1} = (S_{PD} \times A_{READOUT} \times A_{ADC})^{-1} \quad (6.4)$$

Thus, if A_{SF} , A_{OUT} and A_{ADC} are known the conversion gain of the pixel photo-diode can be determined. This gives the photo-diode capacitance (S_{PD}^{-1}). Graphically, if the image noise is plotted against the image mean *on a log-log scale*, a graph such as is shown in Figure 6.2 is the result. Janesick *et. al.* called this plot a photon-transfer curve. The slope of the photon shot noise when plotted as a log-log is 1/2:

$$\sigma_{PQE}^2 = KS(\text{codes}) \quad (6.5)$$

$$\Rightarrow \sigma_{PQE} = \sqrt{KS(\text{codes})} \quad (6.6)$$

$$\Rightarrow \log(\sigma_{PQE}) = \frac{1}{2} \log(KS(\text{codes})) \quad (6.7)$$

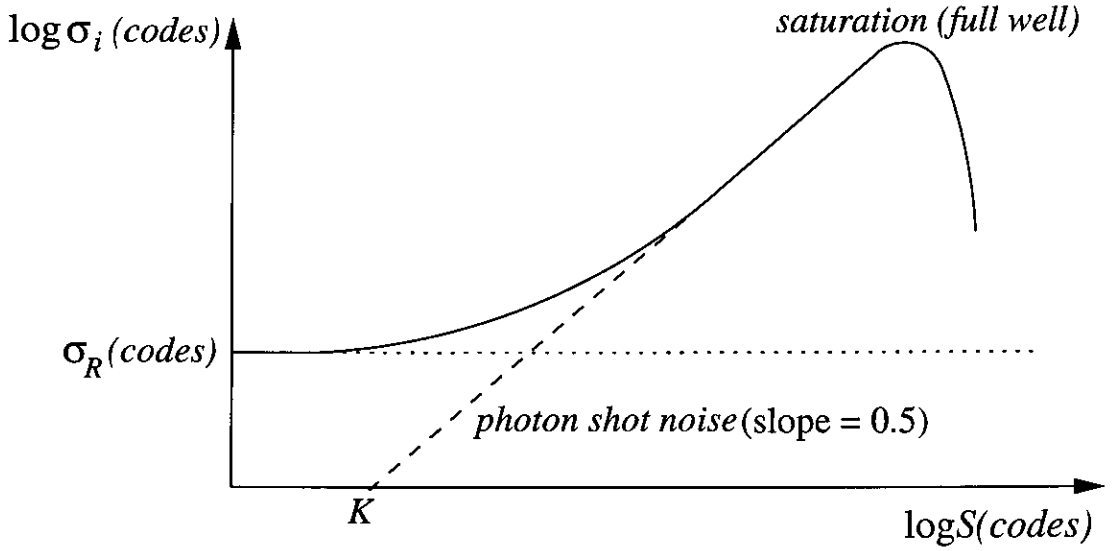


Figure 6.2: Photon-transfer curve of an image sensor.

This provides a simple graphical method with which to evaluate both the constant K and also the saturation signal of the sensor. To get K , a straight line is fitted to the sloped part of the photon-transfer curve, this is where:

$$\left(\frac{\sigma_{PQE}}{K}\right)^2 = \frac{S(\text{codes})}{K} \gg \sigma_R^2 \quad (6.8)$$

i.e. where the shot noise is dominating. The intersection of the shot-noise line with the X-axis occurs at:

$$\sqrt{\frac{S(\text{codes})}{K}} = 1 \quad (6.9)$$

as the Y-axis uses a log scale. Re-arranging Eq. 6.9 gives:

$$K = S(\text{codes}) \quad (6.10)$$

which shows that K can be determined using the straight line fitting method. However, the line must be fitted to a part of the curve where the shot noise in the image is much greater than the noise floor, which may not always be the case. In this work, the use of equation 6.2 to evaluate K directly is therefore preferred.

6.2.1 Photon-transfer curve of the double junction sensor

In the case of the double junction image sensor evaluated here, the pixel produces two outputs and so there are two distinct photon-transfer curves to be measured. The voltage readout from the p^+/n_{well} photo-diode is referred to the $n_{well}/p_{substrate}$ voltage (see section 5.2.1). Therefore, to recover the actual p^+/n_{well} value, this output value is digitally subtracted from the $n_{well}/p_{substrate}$.

During test an unexpected behaviour was observed in the p^+/n_{well} photon-transfer curve. When the mean signal increases beyond a certain threshold, the noise of the p^+/n_{well} output increases suddenly towards that of the $n_{well}/p_{substrate}$. The most probable explanation for this is that the p^+/n_{well} diode is no longer properly reverse biased and begins to simply follow the $n_{well}/p_{substrate}$ diode. The device may also be suffering from a parasitic bipolar action as the two junctions are no longer reverse biased.

6.3 Charge collection

6.3.1 Conversion gain

Conversion gain is determined by the photo-diode capacitance and the output signal chain, resulting in the overall transfer function factor K^{-1} (codes/ e^-). A photon-transfer curve was used to determine this for each output of the pixel.

To do this, the temporal noise for increasing illumination was determined by subtracting two frames taken under identical conditions and then computing the variance of the result. This variance was then divided by two to give the image noise at each illumination. These values were then plotted against the image mean. To ensure that the illumination was uniform and to avoid edge effects in the pixel array, a central section of the pixel array was used to compute the statistics and a diffused light source was used.

Figure 6.3 shows the photon-transfer curves for the sensor. K was determined using eq. 6.2 for each data point, and the values averaged in the valid region (well below saturation) to give a final value of $26 e^-/\text{code}$ and $38 e^-/\text{code}$ for the $n_{well}/p_{substrate}$ and p^+/n_{well} outputs respectively. For the p^+/n_{well} output, the value of K was quite difficult to determine, due to the sudden increase in the noise level at higher light levels. To work round this problem, the value of K was calculated where the slope of the shot noise characteristic was close to the

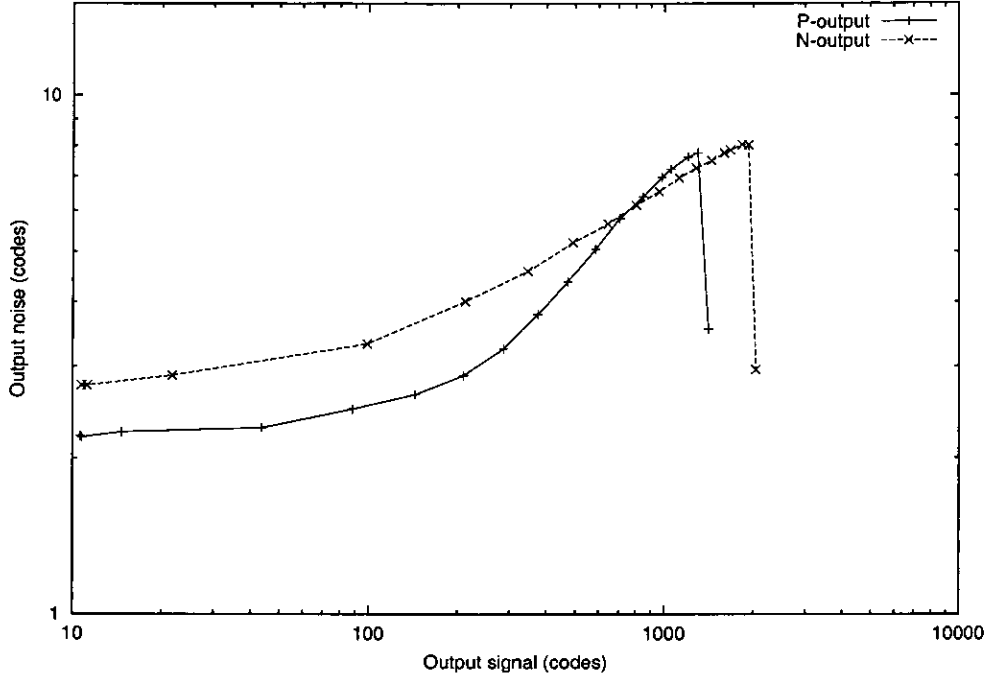


Figure 6.3: Measured photon transfer curve of the image sensor.

theoretical value of $1/2$. The problem of determining the p^+/n_{well} pixel parameters is revisited in Section 6.4.1.

To determine the photo-diode capacitance, the gain from the photo-diode voltage to the output of the ADC in codes must be known. Eldo simulation was used to determine the gain from the photo-diode to the sensor output.¹ This value was found to be 0.73. After the sensor, there is a pre-ADC amplifier with a voltage gain of 2, and at the ADC, 1V is divided into 2048 codes.

This gives:

$$A_{READOUT} = 0.73 \times 2 \quad (6.11)$$

$$A_{ADC} = 2048 \quad (6.12)$$

$$S_{PD} = (K \times A_{READOUT} \times A_{ADC})^{-1} \quad (6.13)$$

$$\Rightarrow S_{PD} = (K \times 2990)^{-1} \quad (6.14)$$

¹This method relies on the matching between simulation models and the silicon results. A better method would be to allow a test input to the column inputs to characterise the transfer function of the read-out stages on the device under test. The present design does not have this feature, but it should be included on future designs. Experience has shown however, that Eldo is quite accurate with the models used, and it is estimated that the error in the gain value used should be within +/- 5%.

Using the values of K determined above, the photo-diode conversion gain can be inferred as 13 and $9 \mu V/e^-$ for the $n_{well}/p_{substrate}$ and p^+/n_{well} photo-diodes, equivalent to a capacitance of 12 fF and 18 fF. This is of the expected order, with the p^+/n_{well} capacitance being higher due to the heavier doping levels at the junction.

The parameter K represents the inverse photo-diode conversion gain ($e^-/code$), therefore the number of electrons collected by the photo-diode is given by:

$$N_{int} = K \times S(\text{codes}) \quad (6.15)$$

It can be noted that the saturation of the signal occurs at the maximum ADC output level. The ADC range is limiting the signal rather than the pixel performance itself. By repeating the measurement without the $2\times$ ADC pre-amplifier and re-calculating K , the saturation levels for the pixel were estimated as $30000 e^-$ for the p^+/n_{well} and $50000 e^-$ for the $n_{well}/p_{substrate}$, which is consistent with the pixel capacitances and voltage ranges. The peak SNR was 43 dB and 47 dB respectively.

6.3.2 Sensitivity

The sensitivity of the sensor was measured with and without microlenses, and with three different colour filters. A diagram of the setup used is shown in Figure 6.4. It consists of a low ripple DC supplied tungsten-halogen bulb to provide light, an integrating sphere to produce a uniform illumination, and a calibrated photo-metric photo-diode to sense the illumination from one output port of the sphere. The sensor was mounted on the other output port and images at a set exposure grabbed for each illumination level. The illumination was varied by changing the neutral density/IR filter between the light source and sphere. To calibrate the relationship between the light level at the two output ports, a set of measurements was taken at both ports using the photo-metric diode and a correction factor computed.

To calculate the sensitivity, a straight line fit through the image mean vs. lux level data was performed. The constant of proportionality between image codes and lux was then converted into $V/lux.s$ using the by multiplying by the ADC voltage step and dividing by the exposure time. As the unit of sensitivity is $V/lux.s$ the spectral content of the light must be specified. The light source used is equivalent to a black body at 3100 K, and the IR filter cut-off was at

630 nm. Table 6.1 shows the results of the measurements with and without microlenses², and for green, yellow, and magenta colour filters.

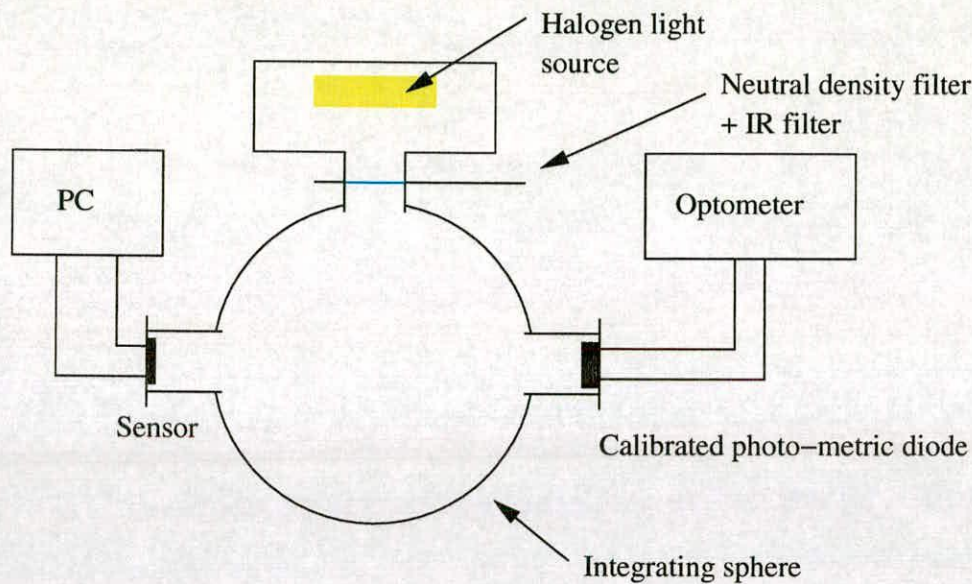


Figure 6.4: Sensitivity measurement setup.

Sensor	$n_{well}/p_{substrate}$ sensitivity (mV/lux.s)	p^+/n_{well} sensitivity (mV/lux.s)
Mono (no μ lens)	188	141
Mono (with μ lens)	257	182
Green (with μ lens)	106	53
Cyan (with μ lens)	118	65
Yellow (with μ lens)	190	116

Table 6.1: Sensitivity measurement results.

In chapter 5 the microlens fill-factor was used with the quantum efficiency to calculate the number of electrons collected by the pixel. On the device, the microlens fill-factor is 77%, and the photo-diode fill-factor is 19%. If the microlens worked perfectly, the ratio in sensitivity between un-lensed and lensed devices would be 4/1. The observed ratio from the sensitivity measurements is actually around 4/3, which is much less, though still a significant improvement. While a 4 times improvement in sensitivity is too much to expect, it was hoped that the

²The use of a light source from an integrating sphere to measure microlensed devices can be problematic due to the fact the microlenses are optimised for a given acceptance angle of light. Incident light from angles outside this range may actually be attenuated by the microlens. However, to verify that this was not the case with these measurements, the relative sensitivity difference between microlensed and standard parts was compared using central portion of images taken using a lens viewing a flat scene under controlled lighting conditions. The same sensitivity ratio was found using the two different methods.

microlens would have a larger effect than is measured.

The lower than expected increase in sensitivity partially be explained by the fact that the microlens was not optimised for this pixel size. Of more significance is that probable impact of the metal 3 light shield over the photo-diode. Consider the diagram shown in Figure 6.5 which shows the worst case with the narrowest opening the light shield. The microlens is only $2.1\ \mu m$ away from the metal 3, the bottom of which is $4.2\ \mu m$ from the actual photo-diode. Therefore, a lot of light which is bent towards the photo-sensitive part of the pixel will simply be reflected off the metal 3 and will not contribute to the sensitivity. The opening in the light shield was set to the same dimensions at the p^+/n_{well} diode to try and maximise the spectral selectivity of the double junction structure. It ensures that light must vertically travel through both junctions. Perhaps, due to the microlens, the opening should be widened to increase the sensitivity. However, the size of opening must ensure most of the light travels through both junctions. There is likely to be a trade-off between sensitivity and spectral response, so optimisation work would be required.

The sensitivity using cyan or yellow filter colours is better than with green as expected (Table 6.1). This shows the benefits in light collection efficiency of using wider bandwidth colour filters over the sensor.

6.3.3 Cross-talk

Excess cross-talk between adjacent pixels can cause a blurring of the resulting image and introduce errors in the colour reconstruction process. To measure the cross-talk on the prototype sensor a section of the pixel array was covered with the top metallisation layer. A small hole was drawn in this metal light shield such that a single pixel was exposed to incident light. This allows the surrounding pixels to be monitored to determine the cross-talk.

As the amount of cross-talk is quite small, care must be taken when measuring it to reduce the effects of noise. The method used was:

1. To remove fixed pattern noise, a dark reference frame was taken. To reduce the temporal noise in this reference frame, an average of 256 real frames was used. This reduces the temporal noise by a factor of $\sqrt{256} = 16$.
2. An LED was then used to sweep the level of illumination on the sensor. At each illumi-

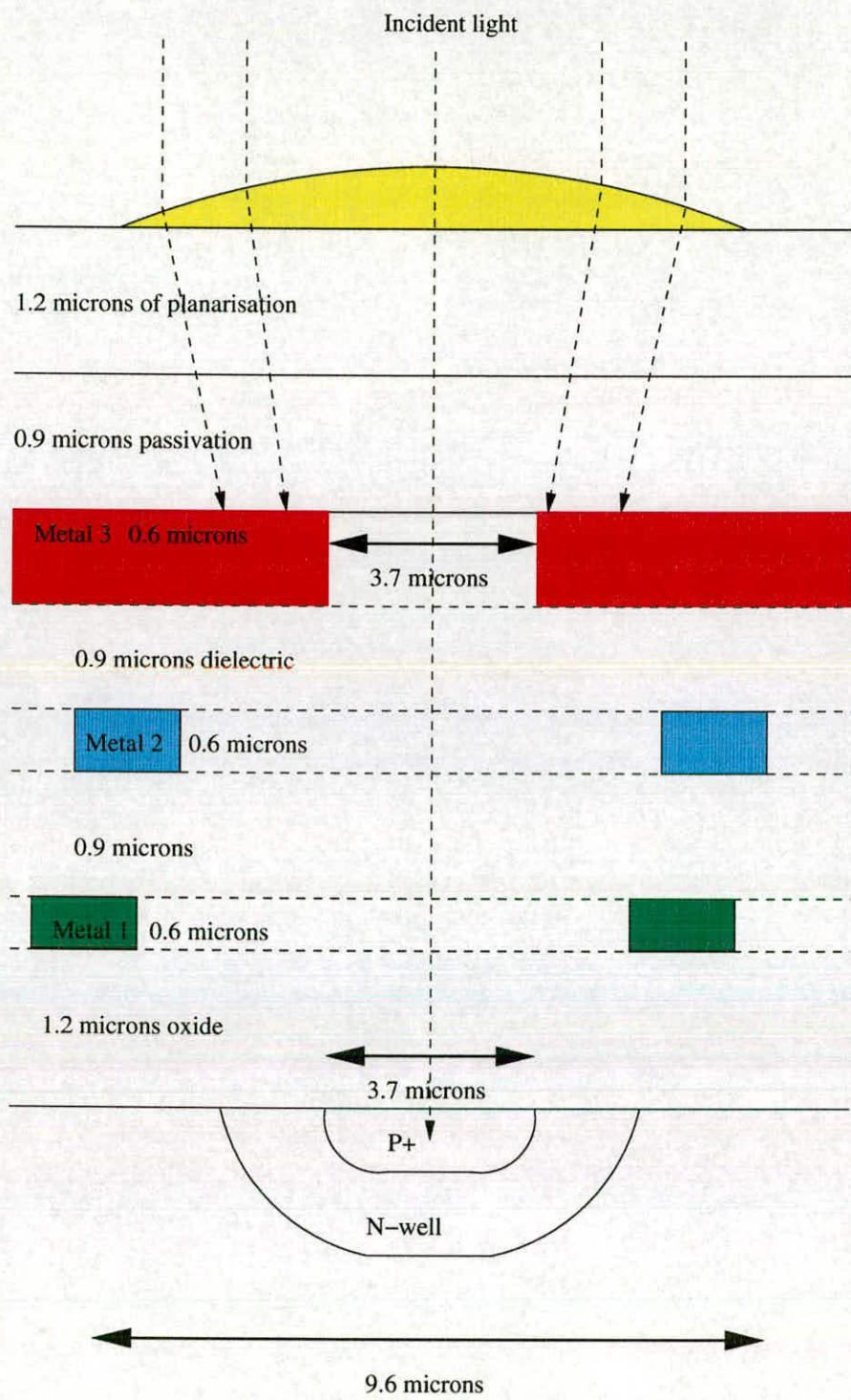


Figure 6.5: *Diagram showing dielectric stack and metal layers between microlens and photo-diode (not to scale).*

nation point an average of 256 frames was recorded, again to reduce the temporal noise in the image.

3. After subtracting the reference frame from each illuminated frame, the percentage cross-talk of each pixel adjacent to the exposed one was computed.
4. Finally, for each adjacent pixel, the percentage cross-talk was plotted against the exposed pixel value. The region of the plot with the most consistent result was chosen as the cross-talk value for that pixel.

Figures 6.6-6.11 show the plotted values for the pixels. In each plot, $-1, -1$ refers to the pixel to the left and one below the illuminated pixel, $+1, +1$ the pixel to the top right, etc. It can be seen that despite the averaging process some of the results are quite noisy. One problem could be that the order of the cross-talk signal at the pixel is only a few ADC codes. Therefore quantisation noise will be quite significant.

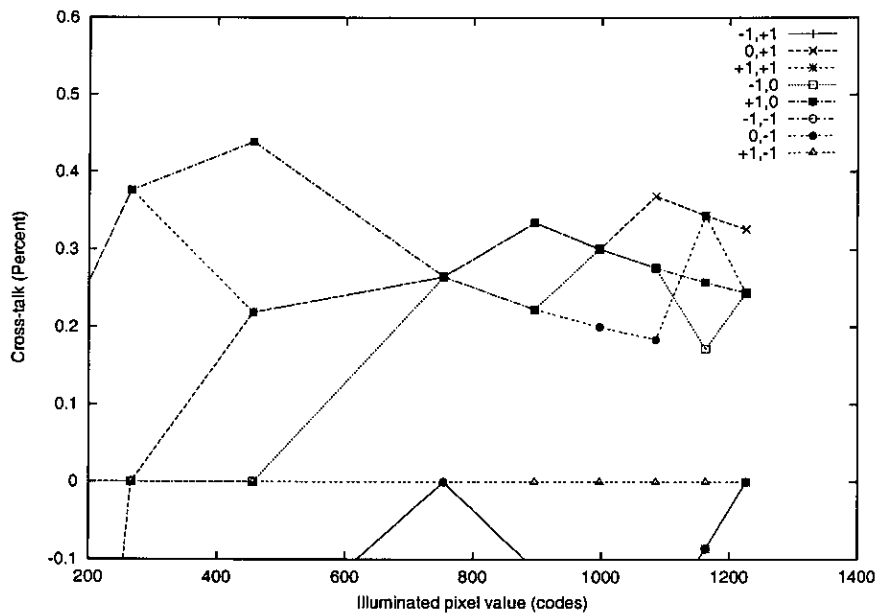


Figure 6.6: *Percentage cross-talk of P-plus outputs vs. illuminated pixel value under blue illumination.*

Figure 6.12 shows the cross-talk for each pixel adjacent to the illuminated one. It can be seen the the cross-talk increases with increasing wavelength for both pixel outputs. Also, as expected, cross-talk is higher with the N-well outputs. According to device simulation results, there should be zero cross-talk from the P-plus outputs. In reality however, some cross-talk can be observed. It is possible that this is due to reflection of photons from metal layers in the pixel

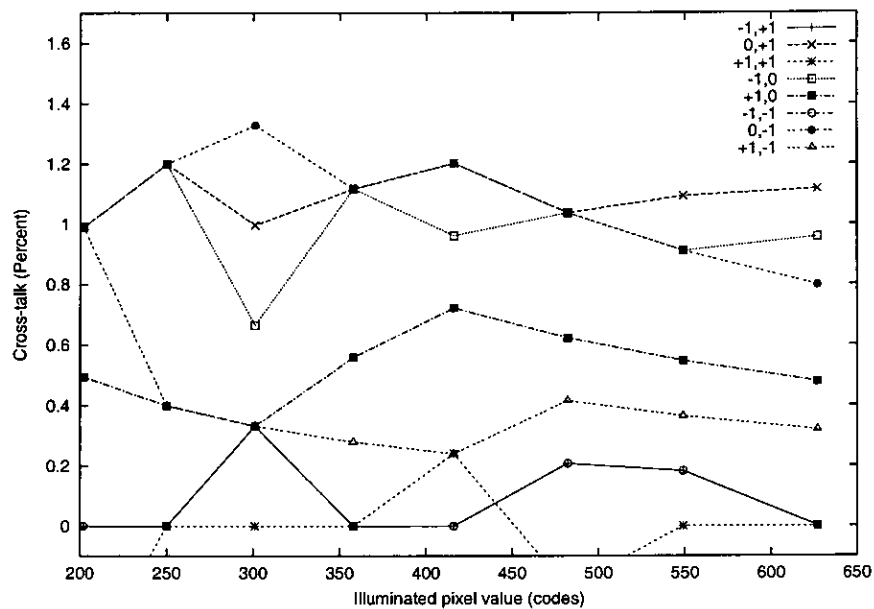


Figure 6.7: Percentage cross-talk of P-plus outputs vs. illuminated pixel value under green illumination.

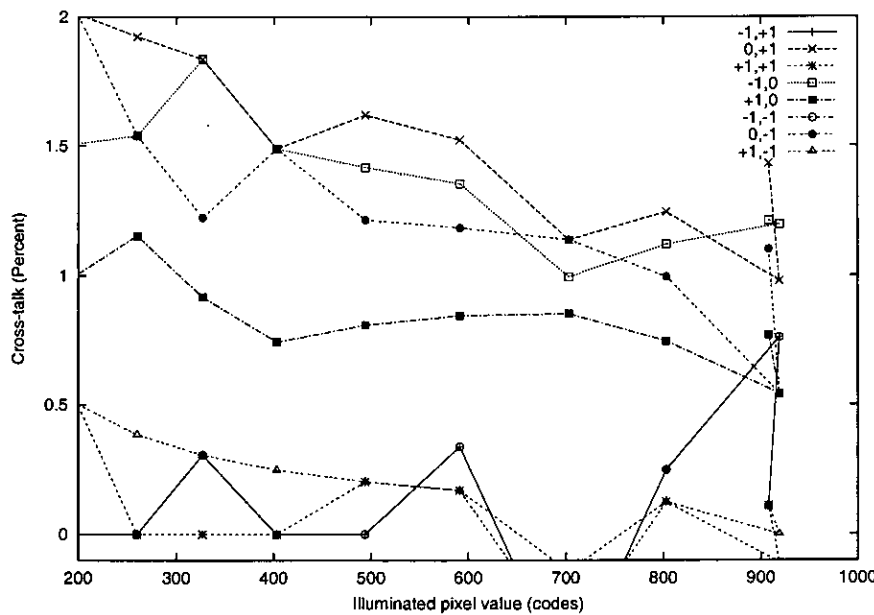


Figure 6.8: Percentage cross-talk of P-plus outputs vs. illuminated pixel value under red illumination.

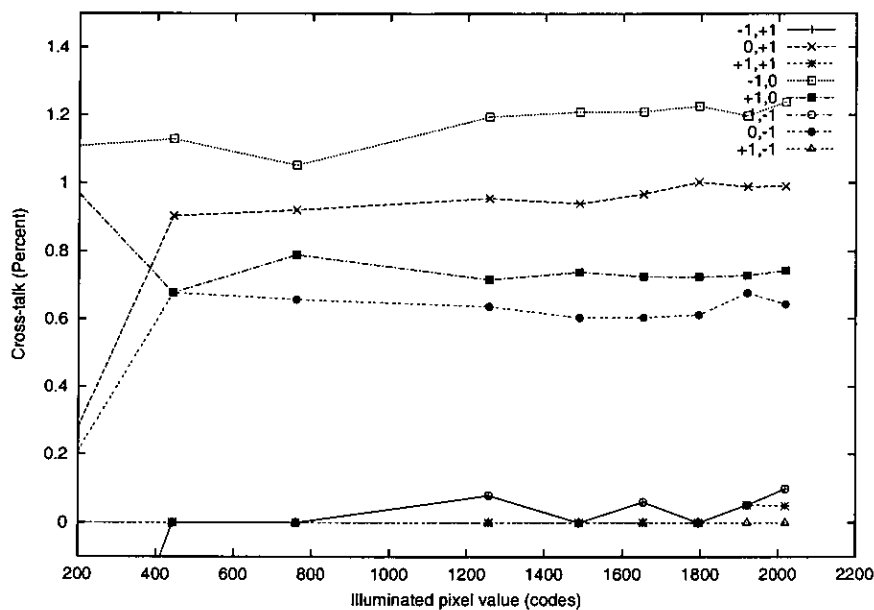


Figure 6.9: Percentage cross-talk of N-well outputs vs. illuminated pixel value under blue illumination.

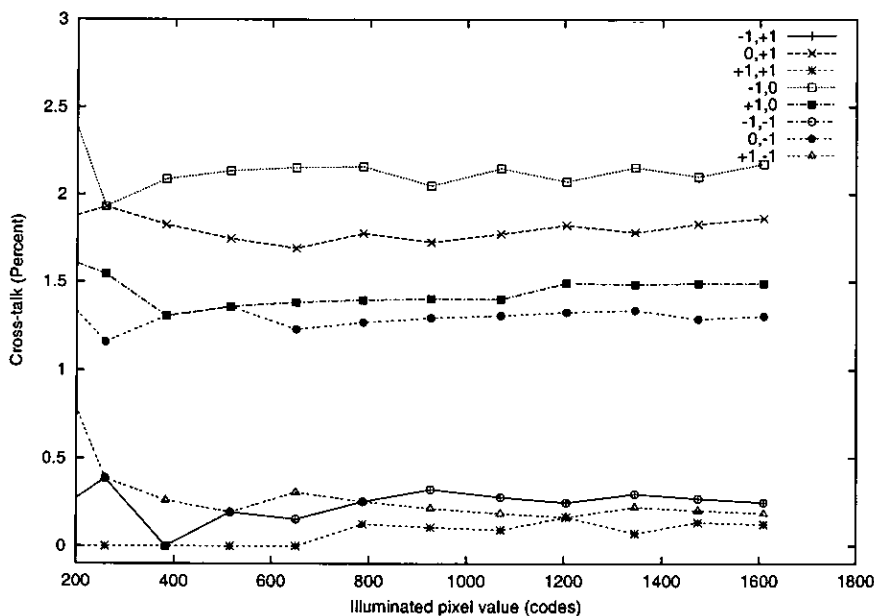


Figure 6.10: Percentage cross-talk of N-well outputs vs. illuminated pixel value under green illumination.

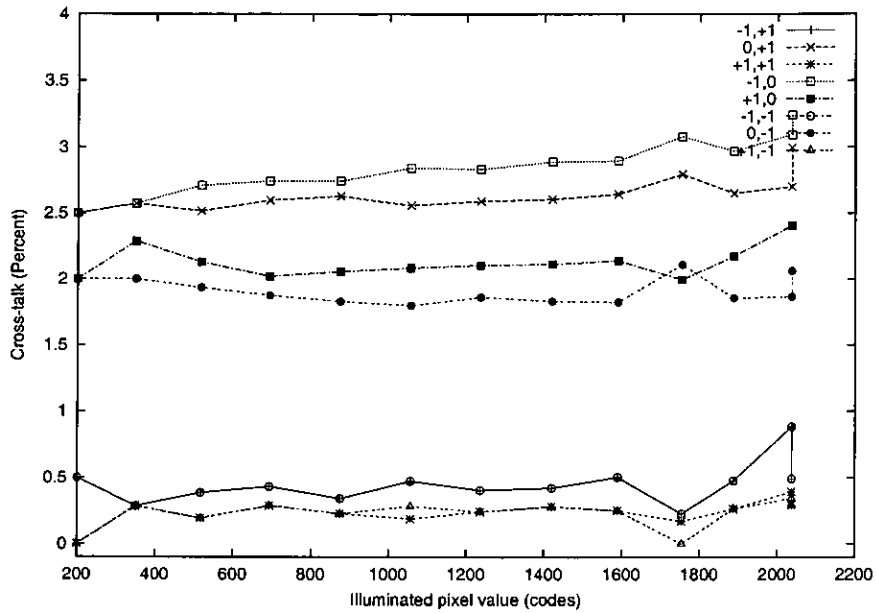


Figure 6.11: *Percentage cross-talk of N-well outputs vs. illuminated pixel value under red illumination.*

rather than carrier diffusion in the silicon.

Certainly, the cross-talk in a normal image is unlikely to be significant. It is likely to be of the same order as the temporal and fixed noise sources in the image and would therefore be virtually unnoticeable.

6.3.4 Pixel response non-uniformity

Poor matching between the conversion gain of the pixels manifests itself in the image as a grainy effect. For a flat scene (for example a uniformly illuminated white card) every pixel should produce the same output voltage, subject of course to a time varying temporal noise. Variation in the conversion from light to voltage in the pixel can be measured by illuminating the sensor uniformly using a diffused light source, averaging a large number of frames (in this case 256) to reduce the temporal noise to a negligible level, removing the FPN and dark current using a reference frame, and then computing the variance of the sensor output.

A plot of standard deviation of a central portion of the image sensor vs. the image mean as the light level is increased is shown in Figure 6.13. It can be seen that the non-uniformity of the p^+/n_{well} pixel output is very high, equivalent to a standard deviation of around 8% of the image mean. The $n_{well}/p_{substrate}$ junction has much better matching - in fact is possible

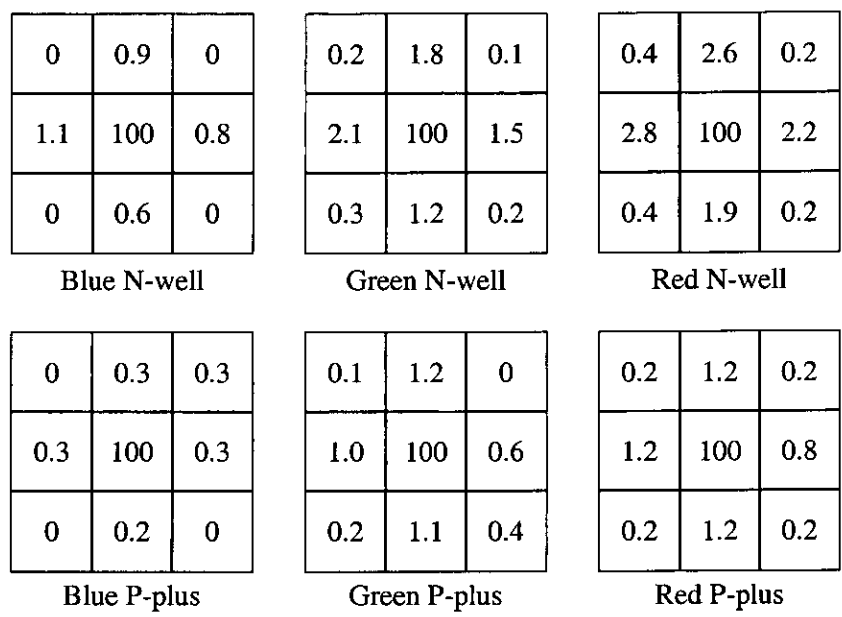


Figure 6.12: Diagram showing percentage cross-talk to adjacent pixels for the two pixel outputs for blue, green, and red illumination.

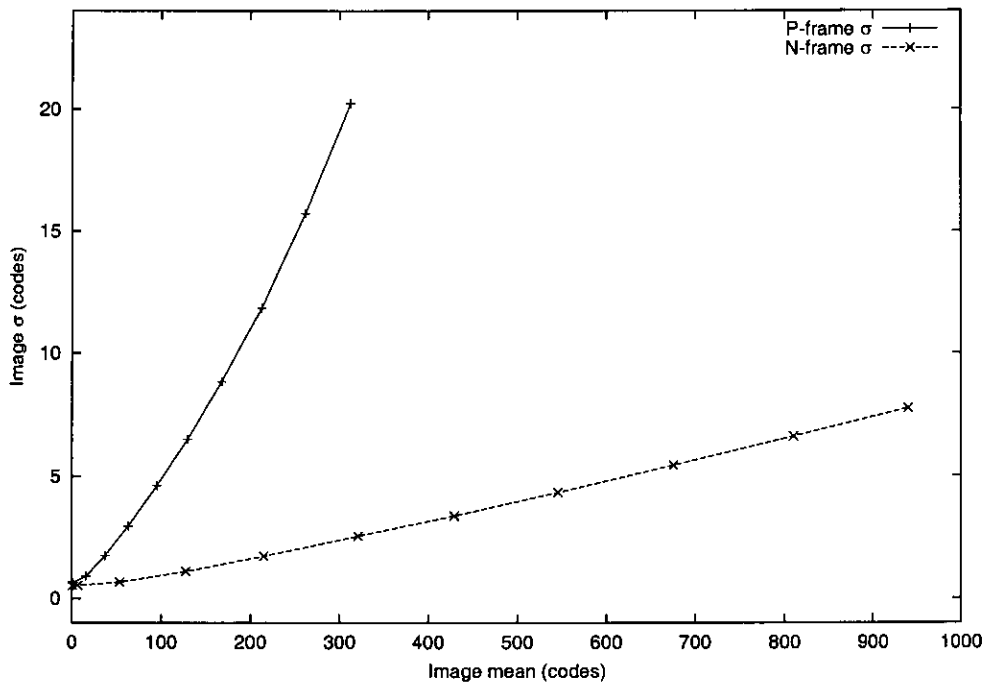


Figure 6.13: Standard deviation of the two pixel outputs vs. image mean as illumination is increased.

that the variation shown is due in part to light source non-uniformity rather than matching, or residual temporal noise.

The large conversion gain non-uniformity of the p^+/n_{well} output could point to a parasitic bipolar action, with the observed behaviour attributed to poor current gain matching between the parasitic $p-n-p$ photo-transistors. β matching between parasitic bipolars in CMOS processes is known to be poor. However, several other observations can be made which contradict this theory:

1. Firstly, after reset, both junctions of the double junction structure are reverse biased, therefore the transistor should be operating in the cut-off regime, and therefore current gain should not be possible due to the removal of minority carriers from the base region. Drift currents in the depletion regions (i.e. photo-diode currents) should be the only currents.
2. Secondly, the current gain of a photo-transistor would cause the total current collected at the p^+/n_{well} (the emitter) to be much larger than that collected on the $n_{well}/p_{substrate}$ junction (the base), which should produce a larger voltage on the p^+/n_{well} output for a given illumination. However, this is not the observed behaviour.
3. Finally and most importantly, device simulations of the double junction structure under the same operating conditions did not show any such bipolar action.

The only other likely explanation is that there is a large variation in the conversion gain at this pixel output between pixels. The junction is quite abrupt and is heavily doped, therefore one might expect a larger variation in the depletion width of the p^+/n_{well} junction. Such a variation would affect both the capacitance and quantum efficiency. However, a standard deviation of 8% is a large variation, larger than would be expected.

It would be interesting to investigate the root cause of the poor matching of the p^+/n_{well} pixel outputs. Due to time constraints this has been left to future work. Some candidate for investigation would be to use the PLDD implant instead of the heavier P^+ to form the top junction, to use just the P^+ implant, or to use an alternative implant for the n_{well} if available. For the meantime, signal processing during the image reconstruction phase has been used to remove the effects of this mismatch.

6.4 Noise

6.4.1 Temporal noise

Temporal noise in the image under reasonable illumination is dominated by the photon shot noise. However, under low light conditions other noise sources, especially reset noise in the pixel, become significant. To measure the noise floor of the sensor, two frames at minimum exposure are taken in the dark, subtracted from each other, and the variance of the result computed. This is then divided by two to give the variance of a single frame. By using zero exposure, noise from the sensor dark current is reduced to a negligible level.



Figure 6.14: *An example frame of image noise after frame subtraction.*

Figure 6.14 shows an image of the residual noise after frame subtraction for the $n_{well}/p_{substrate}$ pixel outputs, scaled such that it covers the entire gray-scale range from white to black. It can be seen that the noise distribution is random, i.e. there is no fixed pattern noise contribution left. The noise was calculated as 2.81 and 2.32 codes RMS for the $n_{well}/p_{substrate}$ and p^+/n_{well} frames. When referred to the photo-diodes this is equivalent to 0.94 and 0.78 mV.

These values can be used to try and obtain a second estimate for the pixel capacitances. The noise at zero exposure can be written as:

$$\sigma_{total}^2 = 2\sigma_{kTC}^2 + \sigma_{READOUT}^2 \quad (6.16)$$

For a well designed sensor $\sigma_{READOUT}$ should be much less than σ_{kTC} . One way to estimate C is therefore to neglect $\sigma_{READOUT}$ completely which gives:

$$C_{PD} = \frac{2kT}{\sigma_{total}^2} \quad (6.17)$$

This method gives a value of ≈ 9.5 fF for the $n_{well}/p_{substrate}$ and ≈ 13.6 fF for the p^+/n_{well} outputs. The values are noticeably lower than those obtained from the photon-transfer method, indicating that the simplifying assumption of neglecting $\sigma_{READOUT}$ is not valid. If the value obtained for the $n_{well}/p_{substrate}$ capacitance taken from the photon-transfer measurement is accepted, the fact that both pixel outputs have identical readout circuitry can be used to give another estimate of p^+/n_{well} capacitance:

$$\sigma_{READOUT}^2 = \sigma_{totalN}^2 - 2\sigma_{kTC_N}^2 \quad (6.18)$$

$$\sigma_{kTC_P}^2 = \frac{\sigma_{totalP}^2 - \sigma_{READOUT}^2}{2} \quad (6.19)$$

A value of 0.44 mV for $\sigma_{READOUT}$ is obtained from this calculation, which gives a value of 21 fF for the p^+/n_{well} capacitance which is fairly close to the value obtained from the photon-transfer measurement.

6.4.2 Fixed pattern noise

The most visible source of fixed pattern noise in image sensors is that which manifests itself as lines in the image. With a column readout architecture such as is used in this sensor, offsets in the column buffer stages contribute *vertical fixed pattern noise* which is to first order independent of the pixel level.

The vertical fixed pattern noise can be measured by taking a frame average at minimum exposure (so that the dark current does not contribute) and averaging the values of all the pixel outputs in a single column. This gives an average value for each column. The standard deviation of these values can then be computed to give a crude measure of the vertical FPN.

However, a more meaningful measurement of vertical FPN should take into account the spatial relationship between the columns. If two columns that are adjacent to each other have very different offsets, this will produce a very obvious line. On the other hand if there is simply a gradual gradient from one side of the pixel array to the other this will not be as obvious. This

leads to a differential measurement of column FPN, where the difference between adjacent columns is plotted against location in the image. This is analogous to a differential non-linearity plot as is often used when characterising analogue-to-digital converters.

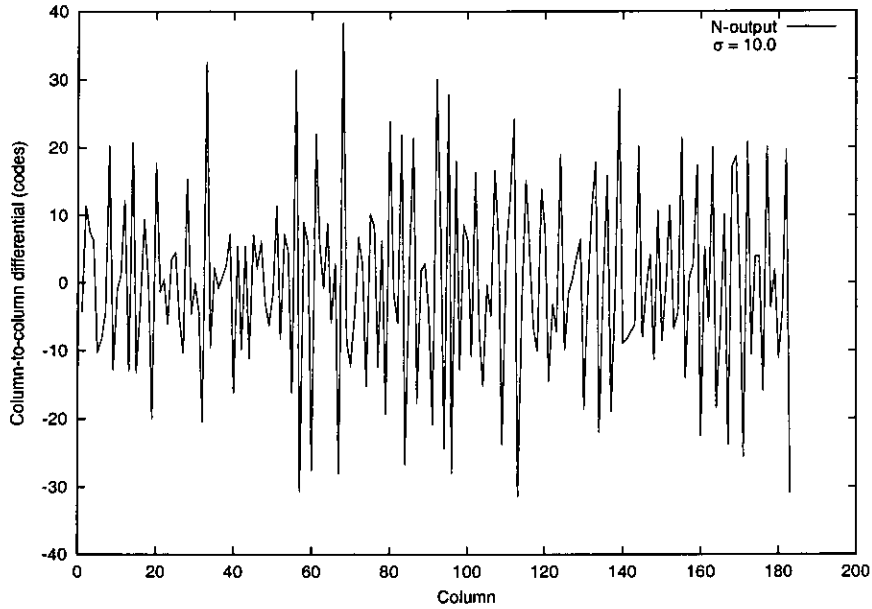


Figure 6.15: *Differential vertical FPN for the N-outputs.*

The differential vertical FPN for the $n_{well}/p_{substrate}$ and p^+/n_{well} pixel outputs is plotted in Figures 6.15-6.16. The standard deviation is given as 10.0 and 13.0 codes for the $n_{well}/p_{substrate}$ and p^+/n_{well} outputs respectively, but this does not give a real estimate of the maximum which is around about 40 codes. This is a large value that is very noticeable in the image.

Such an amount of FPN is to be expected with the column read-out method used, as there is no offset cancellation employed. Offset cancellation for this column has been demonstrated in [100] for example, with the addition of an extra switch and a differential offset sampling output stage. In the measurements in this chapter, and when reconstructing colour images from the sensor, the vertical FPN was digitally subtracted in software before other processing, which produces an equivalent result.

6.4.3 Dark current

Dark current contributes an exposure dependent fixed pattern noise to the image and should be minimised. It also contributes dark current shot noise which is time-varying and of a much lower value than the fixed noise. As was discussed in Chapter 2, dark current is an exponential

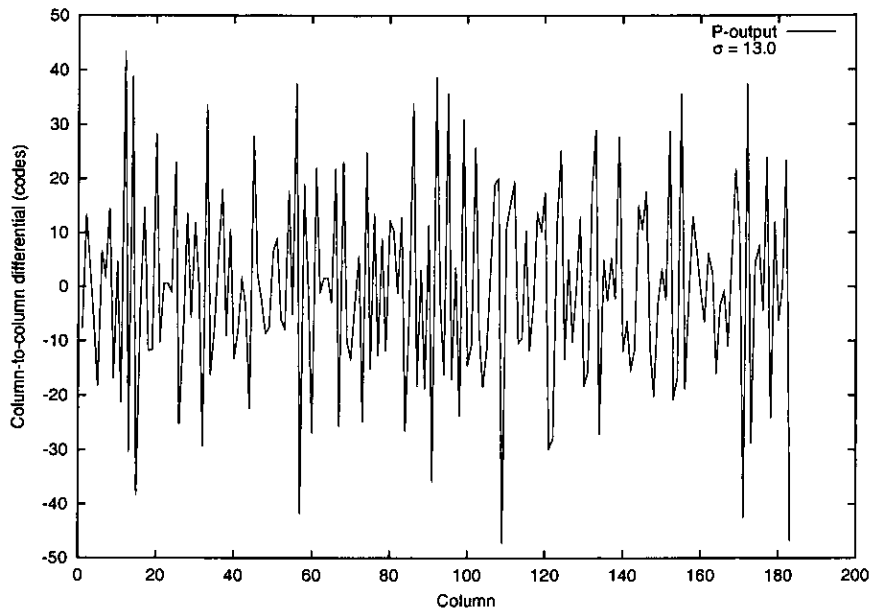


Figure 6.16: *Differential vertical FPN for the P-outputs.*

function of temperature, therefore measurements must be made in a temperature controlled environment.

Figures 6.17-6.19 show a histogram of the dark current measured at 25, 45, and 65°C. It can clearly be seen that both the dark current mean and spread rapidly increase with temperature. These measurements were taken with a pixel integration period of 800 ms. Vertical FPN has been removed in the usual way.

The $n_{well}/p_{substrate}$ pixel output collects the dark current from both junctions, and also has a larger conversion gain which explains the fact the dark current output is larger. The dark current output in codes can be converted to mV, electrons, or amps at the photo-diode, the results of which are shown in Table 6.2.

The assumption that the dark current FPN contribution is the same as the mean dark current is often made. It can be seen however that the contribution due to the spread of the dark current is always lower than the mean which is a positive result. The dark current for the p^+/n_{well} output is also very low, probably due to the pinning effect of the p^+ implant at the surface and the narrow depletion width at the p^+/n_{well} junction.

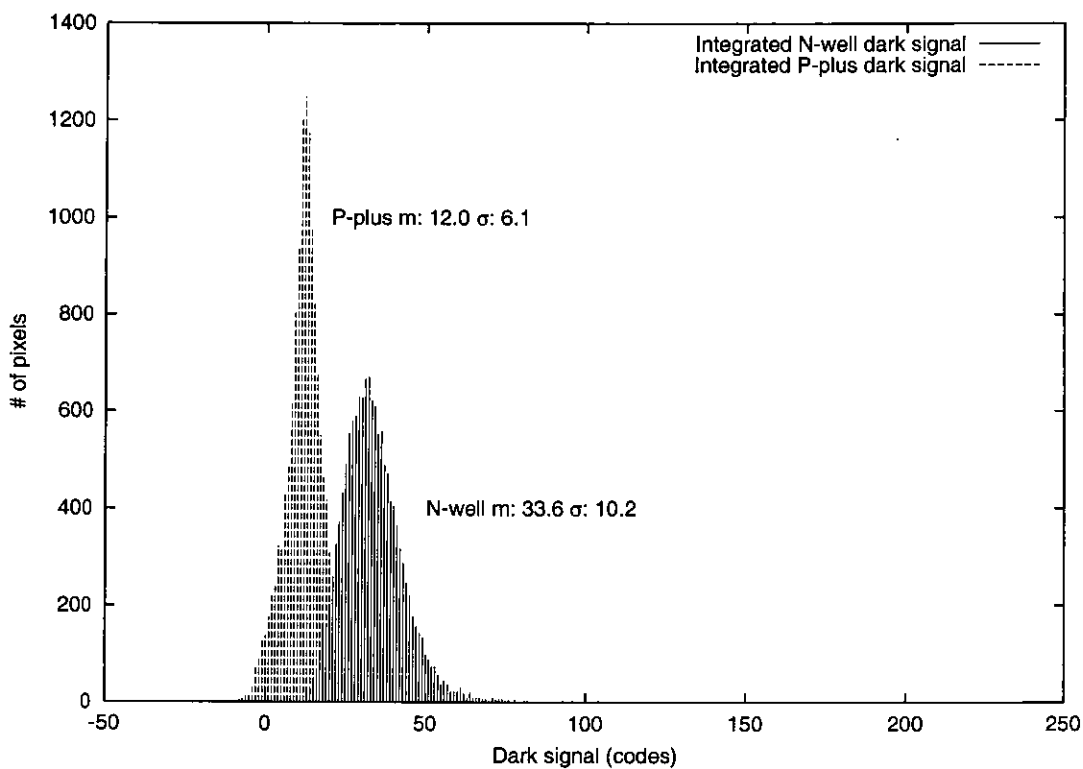


Figure 6.17: Histogram of dark current at 25 degrees C.

Temp. (°C)	p^+/n_{well} output mean dark current			
	codes/s	mV/s	e^-/s	I_{dark}
25	15.0	5.0	540	87 aA
45	45.4	15.2	1640	262 aA
65	239.1	79.9	8608	1.38 fA
p^+/n_{well} output σ of dark current				
25	7.6	2.5	274	44 aA
45	16.5	5.5	594	95 aA
65	61.1	20.4	2200	353 aA
$n_{well}/p_{substrate}$ output mean dark current				
25	42.0	14.0	1092	175 aA
45	192.5	64.3	5005	802 aA
65	931.6	311.2	24222	3.88 fA
$n_{well}/p_{substrate}$ output σ of dark current				
25	12.8	4.3	331	53 aA
45	46.8	15.7	1218	195 aA
65	152.2	50.9	3958	634 aA

Table 6.2: Summary of dark current measurements.

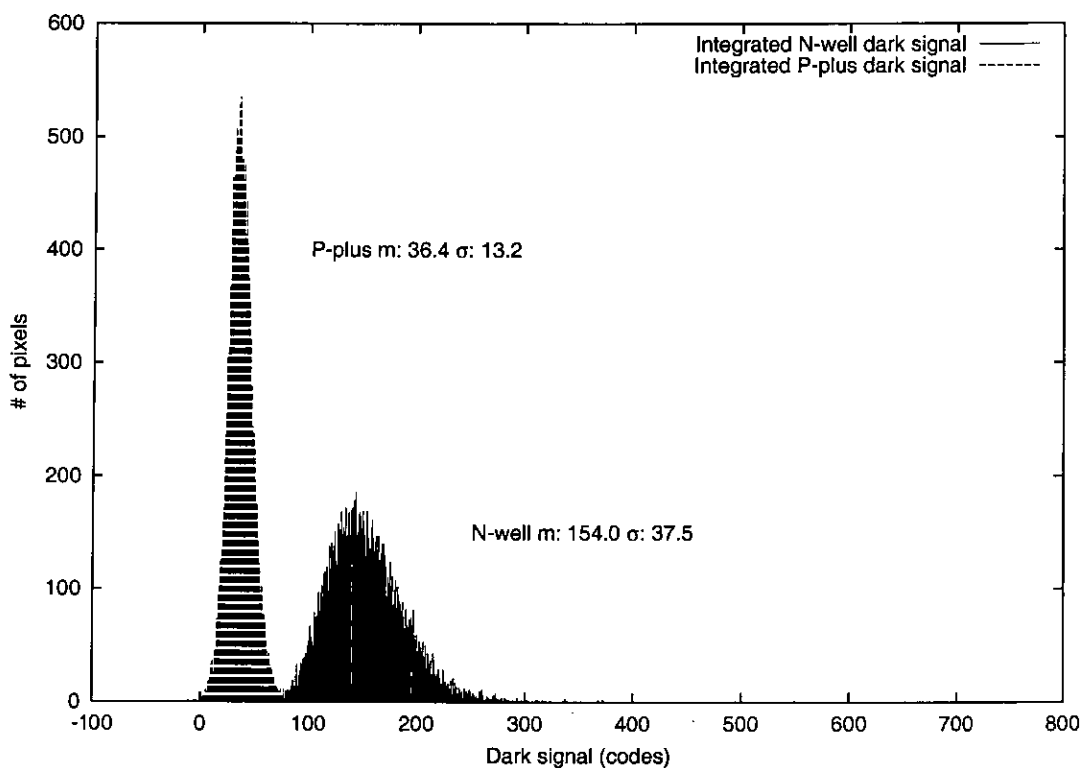


Figure 6.18: Histogram of dark current at 45 degrees C.

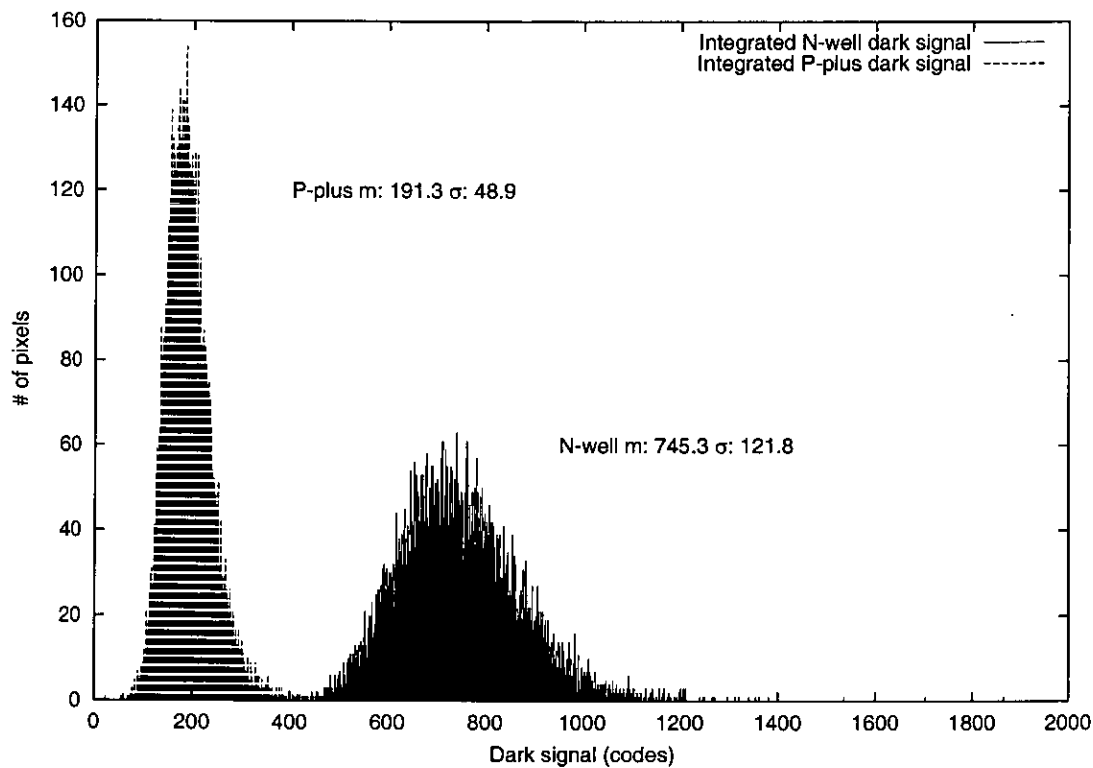


Figure 6.19: Histogram of dark current at 65 degrees C.

6.5 Comparison with standard sensor

The sensor performance can be compared with a standard 3T-pixel sensor disclosed at the *International Solid-State Circuits Conference* [14]. The results of this comparison are shown in Table 6.5.

It can be seen from the table that the performance of the double junction sensor in certain parameters is superior to the standard approach. In particular the peak SNR for the $n_{well}/p_{substrate}$ outputs is better due to the larger pixel capacitance and hence full well capacity. Allocating more voltage range to the p^+/n_{well} pixel outputs would increase this value too, but at present this is limited by the voltage drops of the pixel source followers. An alternative pixel structure which solves this problem is presented in Section 8.3.1. This would also improve the dynamic range which at present is inferior to the standard sensor (for the p^+/n_{well} outputs). It is also interesting that the measured dark current of the sensor is lower than with the standard approach. However, this should not just be attributed to the pixel design, as the manufacturing technologies are different.

Unfortunately, the sensitivity and random noise floor of the prototype sensor is significantly worse than the competing device. The sensitivity difference cannot be accounted for by the read-out and conversion gain differences alone — therefore it must be due to a reduced quantum efficiency. Clearly, the microlenses used cannot recover the losses caused by the reduced photo-diode fill-factor. The raised random noise floor can be attributed to the larger kTC noise and also to the simple readout architecture compared with the standard sensor which uses an in-column ADC.

6.6 Conclusions

This chapter has presented a full characterisation of the low-level performance of the image sensor. In comparison with existing approaches, the performance is acceptable overall, but the sensitivity and gain uniformity need to be improved. In general, there are a lot of process dependent unknowns in the pixel design, therefore to optimise the pixel in future a large number of pixel variants should be evaluated. These variants should vary the spacings and implanted layers in the photo-diode (to try and solve the non-uniformity problem) and also the microlens and light shield design, perhaps by using a lower down metal layer for the light shield (such

Parameter	Double junction sensor		Standard sensor
	$n_{well}/p_{substrate}$	p^+/n_{well}	
Technology	0.35 μm		0.5 μm
Pixel size	9.6 μm		7.5 μm
Microlense fill-factor	77%		70%
Sensitivity	190 mV/lux.s (yellow channel)	116 mV/lux.s (yellow channel)	2.1 V/lux.s (green channel)
Dark current 25°C	190 $pAcm^{-2}$	95 $pAcm^{-2}$	250 $pAcm^{-2}$
Dark current FPN 25°C	331 e^-/s	275 e^-/s	315 e^-/s
Conversion gain	13 $\mu V/e^-$	9 $\mu V/e^-$	40 $\mu V/e^-$
Dynamic range	56 dB	46 dB	57 dB
Saturation SNR	47 dB	43 dB	42 dB
Random noise	73 e^-	88 e^-	42 e^-

Table 6.3: Comparison between double junction and standard sensor performance.

as metal 2). Of course, this may impact the layout of the pixel overall, which is why multiple pixel experiments would be required to optimise the performance.

Chapter 7

Colour image reconstruction

7.1 Introduction

In camera systems, signal processing is used to convert the raw data from the image sensor into a colour image. The typical signal processing used for an RGB sensor was described in section 1.3.4. The process used to obtain the final image is often termed *colour reconstruction*. This can be implemented either in hardware (on the sensor device or in a co-processor) or in software. Here, the colour reconstruction process for the double junction sensor is described. In this work, the algorithms have been implemented in software, but could easily be transferred to appropriate digital hardware.¹

7.2 Colour matrixing

By combining the double junction sensor with two colour filter colours, four spectral responses are obtained. The final display or file format will require 3 values per pixel, most probably RGB values. The conversion from the sensor 4-dimensional colour space to the 3-dimensional space used by the display can be accomplished by a linear transformation. Such a transformation is termed *matrixing* and can be written as:

$$\begin{pmatrix} r_o \\ g_o \\ b_o \end{pmatrix} = \begin{pmatrix} m_{11} & m_{21} & m_{31} & m_{41} \\ m_{12} & m_{22} & m_{32} & m_{42} \\ m_{13} & m_{23} & m_{33} & m_{43} \end{pmatrix} \begin{pmatrix} i_1 - o_1 \\ i_2 - o_2 \\ i_3 - o_3 \\ i_4 - o_4 \end{pmatrix} \quad (7.1)$$

or more succinctly as:

¹The author would like to thank Dr. Stewart G. Smith of STMicroelectronics Imaging Division for all his help with, and explanations of, the colour reconstruction and matrixing processes.

$$\mathbf{C} = \mathbf{M}(\mathbf{I} - \mathbf{O}) \quad (7.2)$$

where \mathbf{I} represents the 4 input values from the sensor for a single pixel and \mathbf{C} the corresponding pixel values (RGB) in the output image. \mathbf{M} is known as the colour matrix, and \mathbf{O} as the offsets. The offsets are there as, for the colour matrix to work, the input must be linear with intensity (e.g. the complete black should have all inputs equal to zero). These matrices must be determined experimentally for a known illumination and display type.

7.2.1 Method

To determine the values for \mathbf{M} and \mathbf{O} a least squares fitting method was used. This experimental procedure was:

1. A set of 24 images of cards of known colour was taken under controlled lighting conditions. In this case standard illuminant D65 (a close match for daylight) was used. To reduce noise an average of 256 frames of each image was used.
2. The mean of the image pixel values was calculated for each pixel output. This resulted in a set of 24 different input \mathbf{I} vectors, each with four values.
3. Using an ordinary least-squares fit to the RGB values of the target colours, the matrices \mathbf{M} and \mathbf{O} were determined.
4. The RMS error in RGB space was calculated to give a crude estimate of the fit. For more insight into the colour reproduction obtained, a chromaticity chart was produced of the error vectors. Additionally, a colour image of the targets adjacent to the actual colour output was produced to allow visual comparison.

7.2.2 Results

A summary of the RMS errors in RGB space after colour matrixing is given in table 7.1. For comparison purposes, the error for a RGB sensor in the same technology using the same fitting method was 9.16 which is significantly lower. This is to be expected, as the colour filters of the RGB sensor are the same as those employed in commercial imagers. These filters are the result of many years of optimisation work and a huge amount of investment. By contrast, the

double junction filters are simply standard filters as used in photography, and are therefore not optimised for the task.

	Magenta	Cyan	Yellow	White	Green	Red	Blue
Magenta	N/A	19.7	16.0	15.9	23.5	N/A	N/A
Cyan	19.7	N/A	16.5	18.6	N/A	15.6	N/A
Yellow	15.9	16.5	N/A	41.4	N/A	N/A	29.7
White	15.3	18.6	41.4	N/A	31.0	39.4	36.3
Green	23.5	N/A	N/A	31.0	N/A	N/A	N/A
Red	N/A	15.6	N/A	39.4	N/A	N/A	N/A
Blue	N/A	N/A	29.7	36.3	N/A	N/A	N/A

Table 7.1: Summary of fit of colour output to RGB targets with various filter combinations (table shows RMS errors in RGB space)

The colorimetric accuracy of the camera would almost certainly benefit from adjustment of the colour filters to suit the double junction responses, together with tailoring of the junction depths and doping levels.

Figures 7.1-7.3 show plots of the error vectors for the 24 target colours. The vectors are plotted in the u'/v' plane. This plane has the property that distances on it represent approximately equal changes in colour to an average human observer [9]. Obviously, the smaller the error vectors the better match the colour output from the camera will be. However, this plot does not illustrate anything about the intensity of the colour, merely its hue, which is why the neutral colours from blank through grey to white all appear at the same point in the chart.

It can be seen that, with a few exceptions, the error vectors are fairly evenly distributed as long as the fit is reasonably good. However, a plot such as in Figure 7.3 indicates a problem with the white balance, as less bright neutral colours have a very large error. In a reconstructed image, this results in grey objects appearing coloured, which is very noticeable to the viewer.

To get a more accurate perspective on the colour performance of the double junction sensor, the error vector plots should be compared with Figure 7.4. This shows the error vectors of an RGB sensor after colour matrixing. Clearly, the colorimetric accuracy is much better.

7.2.3 The problem of white balance

The measurements made to produce the colour matrix were taken under very strictly controlled lighting conditions. Of course, a real camera would be exposed to a variety of lighting condi-

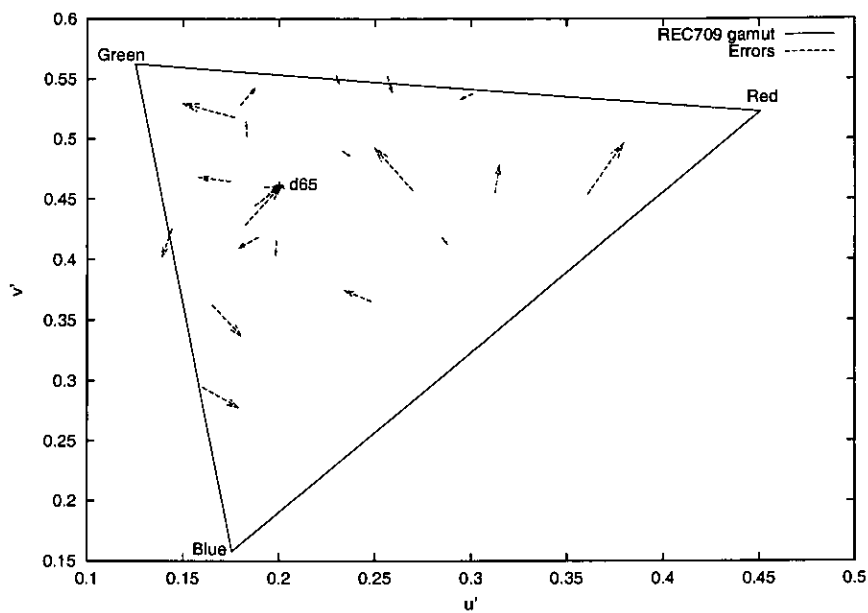


Figure 7.1: Error vectors for the cyan/yellow filter combination after matrixing.

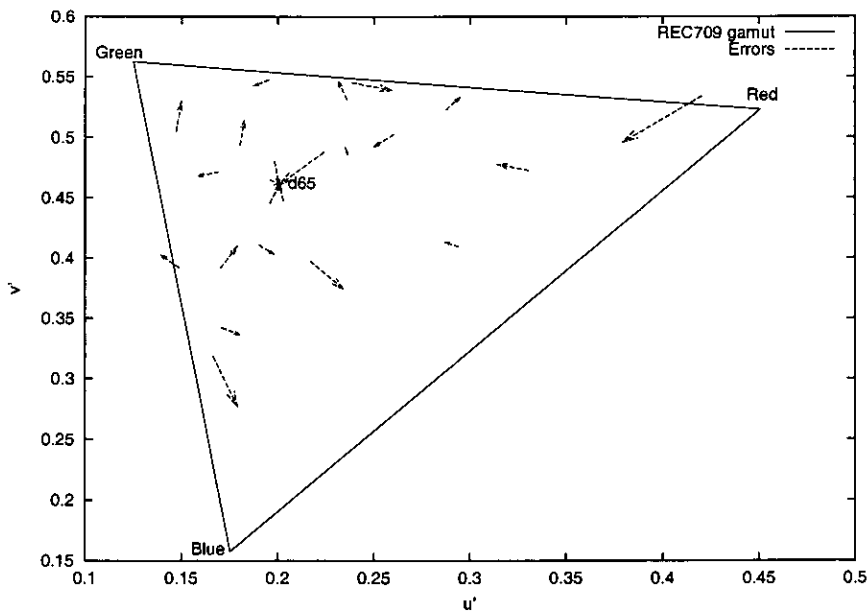


Figure 7.2: Error vectors for the magenta/white filter combination after matrixing.

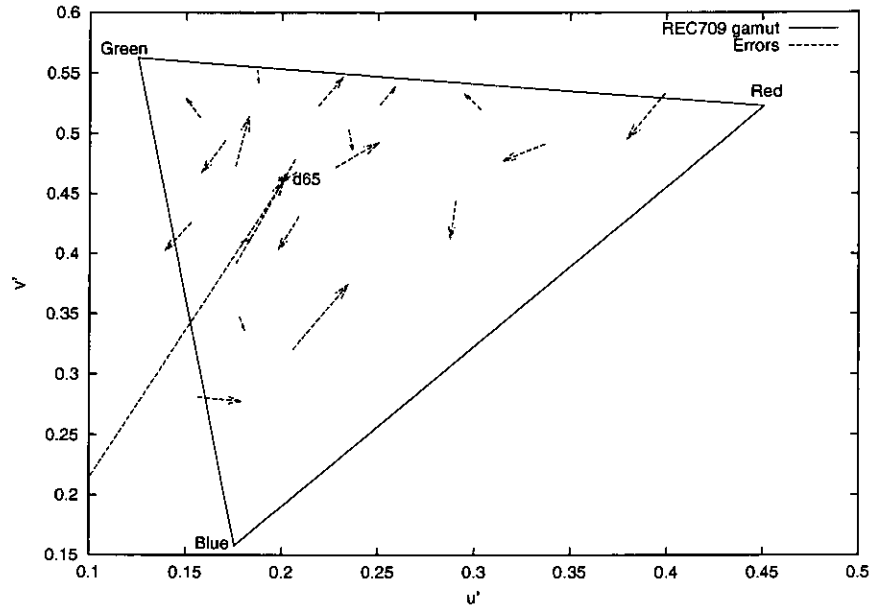


Figure 7.3: Error vectors for the magenta/green filter combination after matrixing.

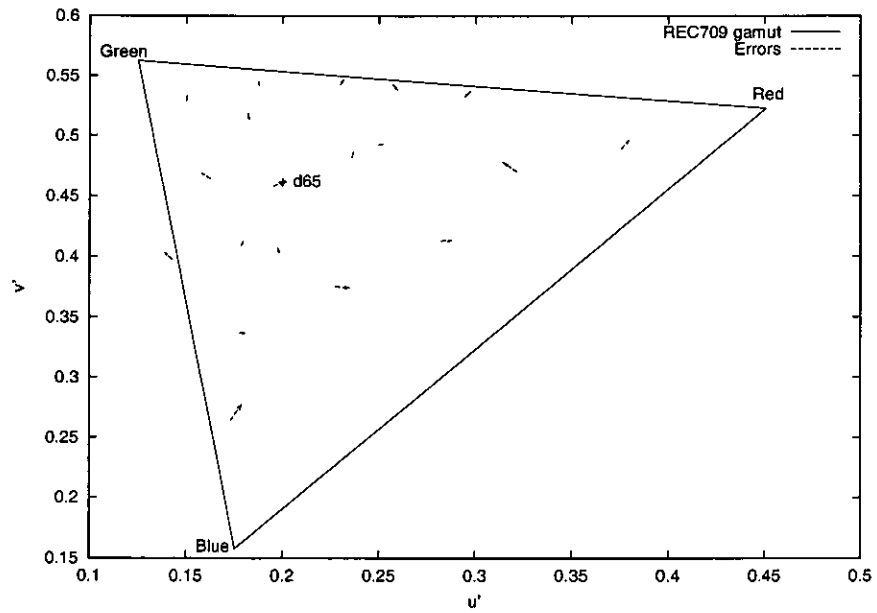


Figure 7.4: Error vectors for a RGB sensor implemented in the same technology.

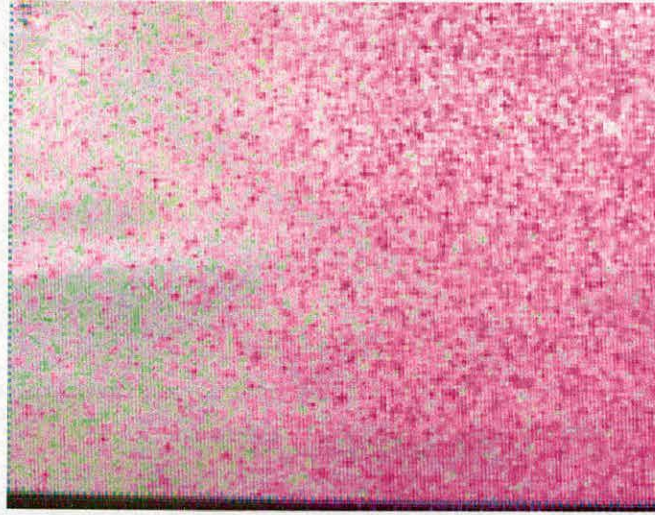


Figure 7.5: *Reconstructed image of a white sheet of paper using the fitted colour matrix.*

tions and must adapt to them such that the output preserves the grayness of neutral objects. In this project, algorithms to perform this on-the-fly white balance have been left for future work.

However, a problem was still encountered when using the colour matrix derived from the measurements. Consider the matrix derived for the cyan/yellow filter combination:

$$\mathbf{M} = \begin{pmatrix} -4.4549 & 4.3953 & 2.0075 & -0.6603 \\ 4.1105 & -4.6898 & -0.8166 & 1.1412 \\ -5.9877 & 10.1615 & 1.1455 & -2.1998 \end{pmatrix} \quad (7.3)$$

To produce the correct colours, this matrix uses large co-coefficients which results in output that is very sensitive to noise or changes in lighting conditions. Figure 7.5 illustrated exactly what effect this has in an image. The figure shows a picture of a blank white sheet of paper taken with the sensor and reconstructed using the matrix above. Even though this picture was taken under controlled lighting, the small changes in the light content that reaches the sensor from one side of the sheet to the other produces a very noticeable change in colour. It is possible that some of the colour is due to reflections and scattered light entering the system without passing through the filter, but the effect is still very large.

To reduce this effect, the sensitivity of the colour matrix needs to be reduced. One way to do this is to introduce noise during the fitting process and fit over a larger number of values. This has two effects:

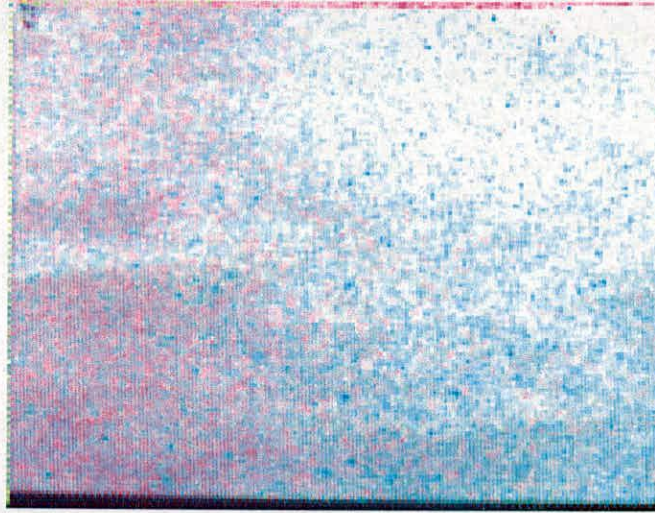


Figure 7.6: *Reconstructed image of a white sheet of paper using the reduced sensitivity colour matrix.*

1. On the plus side, the parameters of the colour matrix become less extreme and their sensitivity to lighting and noise contribution lessens.
2. Unfortunately, this comes at the expense of a desaturation in the colour output.

With the new colour matrix, the false colour on the blank sheet is reduced as expected (Fig. 7.6). However, the plot of the error vectors after matrixing shows that the colours have indeed become less saturated, i.e. they have mostly moved towards the white point.

It is a matter of subjective judgement as to where the best compromise between saturation and sensitivity lies. Hopefully, improvement in the separation between the colour channels would reduce the sensitivity of the resulting colour matrix and alleviate this problem.

7.2.4 Impact of matrixing on signal-to-noise ratio

The four inputs to the colour matrix come from different pixel outputs and therefore contain uncorrelated noise. These noises add in quadrature, and after the matrix the noise in a single channel can be written as:

$$\sigma_C^2 = m_1^2 \sigma_{I_1}^2 + m_2^2 \sigma_{I_2}^2 + m_3^2 \sigma_{I_3}^2 + m_4^2 \sigma_{I_4}^2 \quad (7.4)$$

where m_x represents the colour matrix co-efficients and σ_{I_x} the temporal noise in the differ-

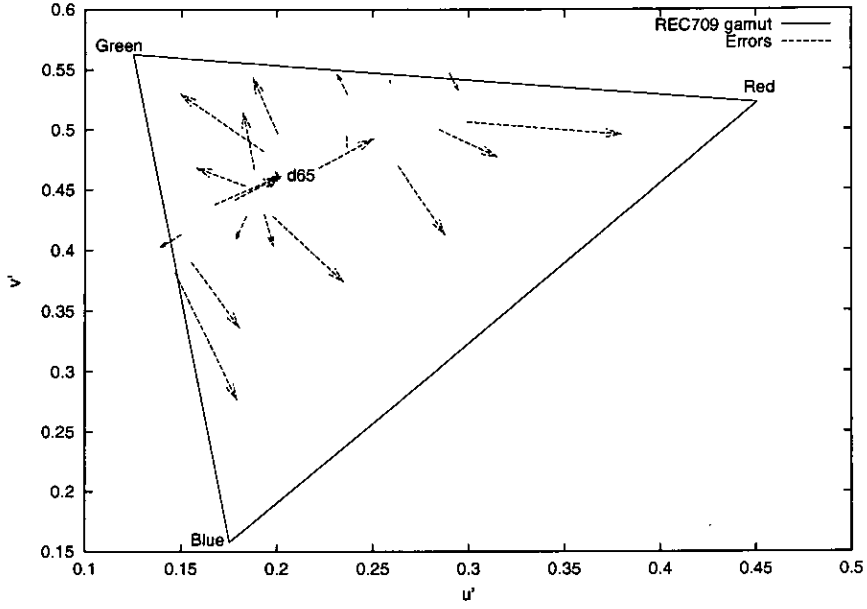


Figure 7.7: Error vectors for the matrix trained over a set of noisy samples.

ent pixel values. The signal can be written as:

$$C = m_1 I_1 + m_2 I_2 + m_3 I_3 + m_4 I_4 \quad (7.5)$$

Equation 7.4 can be used to calculate the noise in the outputs after matrixing for various colour matrices. In the case of the double junction sensor, two of the inputs to the matrix are from $n_{well}/p_{substrate}$ outputs, and the other two from p^+/n_{well} . Therefore $\sigma_{I_1}^2 = \sigma_{I_3}^2$ and $\sigma_{I_2}^2 = \sigma_{I_4}^2$. The contribution due to the $n_{well}/p_{substrate}$ noise will be $\sqrt{m_1^2 + m_3^2} \sigma_{I_1}^2$ and for the p^+/n_{well} will be $\sqrt{m_2^2 + m_4^2} \sigma_{I_2}^2$. The noise after matrixing for different filter colours is summarised in table 7.2.

There are a lot of trade-offs between the colour accuracy and the increase in the noise level in the image. Usually, the blue channel requires the largest matrix co-efficients and hence contains the largest noise. From a noise point of view, the cyan/yellow filter combination seems to perform best. It seems however, that images produced using the reduced sensitivity matrix will contain considerably less noise.

Filter combination	Channel	$n_{well}/p_{substrate}$ noise	p^+/n_{well} noise
cyan/yellow	Red	4.87	4.44
	Green	4.19	4.82
	Blue	6.16	10.40
	RMS	5.14	7.10
magenta/white	Red	6.69	7.48
	Green	0.54	1.50
	Blue	8.40	15.05
	RMS	6.21	9.74
magenta/green	Red	4.26	5.82
	Green	0.69	4.41
	Blue	7.77	14.07
	RMS	5.13	9.16
cyan/yellow low sensitivity	Red	2.42	1.29
	Green	2.11	2.66
	Blue	1.79	4.196
	RMS	2.13	2.96
blue/yellow	Red	21.88	22.82
	Green	22.11	24.74
	Blue	13.30	22.20
	RMS	19.53	23.28

Table 7.2: Noise after colour matrixing for each colour channel with various filter combinations.

7.3 Reconstruction of images

A simple image reconstruction method which produces colour images from raw sensor data was implemented in software. Due to practical constraints, it was only possible to fabricate a sensor with a green and white (no filter) checker-board array. Unfortunately, the colour reproduction from this sensor is very poor (see table 7.1). To test other filter combinations, images were taken with colour filters placed in front of the sensor. These images were then composited in the software to simulate the effect of a colour filter array. The only effect that this will not simulate is the cross-talk between pixels of different colours that would be present with a real CFA. However, section 6.3.3 has shown that this effect is very small.

7.3.1 Reconstruction method

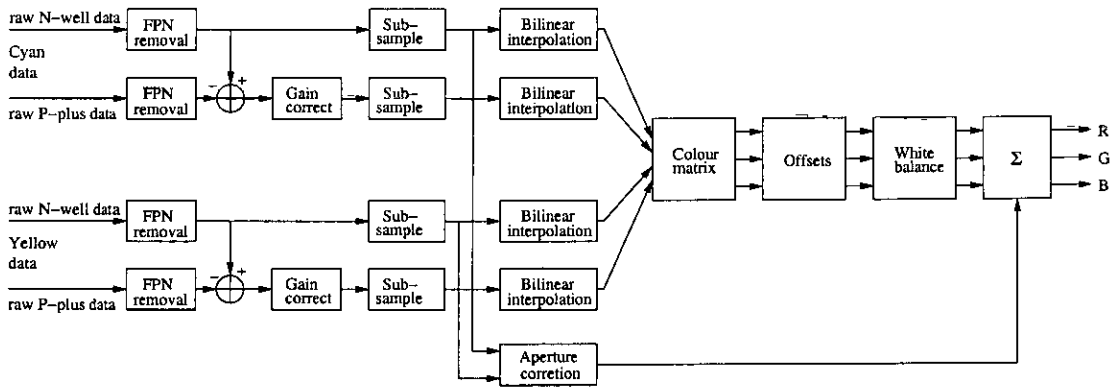


Figure 7.8: Block diagram of the colour image reconstruction process.

Figure 7.8 shows the reconstruction method in block diagram form. An example of the output from each stage is given later in Figures 7.12-7.13. Each of the blocks used is explained below:

FPN removal: In the previous chapter, the vertical FPN of the sensor was found to be very large. To remove this, a reference frame can be subtracted from the raw data. This step can also remove the dark current, if the reference frame is taken at the same exposure and temperature as the image data.

Output subtraction: To recover the actual p^+/n_{well} data values (i.e. the voltage discharge of the p^+/n_{well} photo-diode), the difference between the $n_{well}/p_{substrate}$ and p^+/n_{well} outputs was computed for each pixel value. In actual fact, this step could be performed during the colour matrixing stage, but if performed earlier it allows the raw p^+/n_{well} picture data to be viewed.

Gain correct: In order to compensate for the gain non-uniformity in the p^+/n_{well} output data a gain map was applied to each of the two p^+/n_{well} input frames before further processing. This map was generated from an image taken with the sensor under uniform illumination by computing the ratio of each pixel value to the image mean. To correct the gain errors, each pixel value is divided by the calculated ratio.

Sub-sampling: This step is included to simulate the effect of a checker-board CFA from two images. For the first image, the odd pixels (those shaded grey in Fig. 7.9) are kept, while for the second the even pixels (coloured black) are retained. This data then goes to the interpolation stage.

For a sensor with a CFA, this stage would not be required.

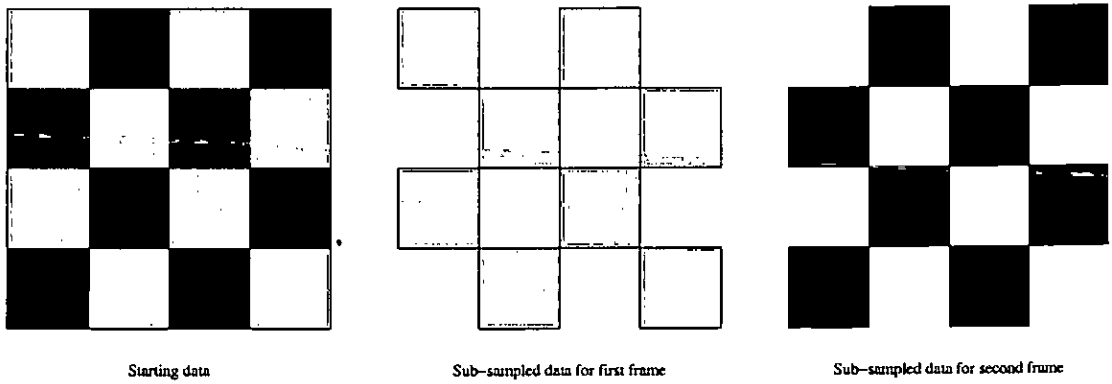


Figure 7.9: Illustration of the sub-sampling step.

Interpolation: In this project, bilinear interpolation has been employed. This is a very simple algorithm, but one which is fairly well suited to the data as there are equal numbers of every spectral response sample. Normally, with data from a Bayer sensor, higher order interpolation algorithms are used.

Bilinear interpolation estimates the missing data for a pixel simply by taking the average of the pixels values adjacent. This is illustrated in Figure 7.10. The estimated value I_1 for the missing pixel in the figure is given simply by:

$$I_1 = \frac{P_1 + P_2 + P_3 + P_4}{4} \quad (7.6)$$

Colour matrixing and offsets: Following interpolation, there are four samples available for every pixel in the final image. The next stage in the reconstruction is to apply the colour matrix and offsets, which produces RGB values suitable for the display.

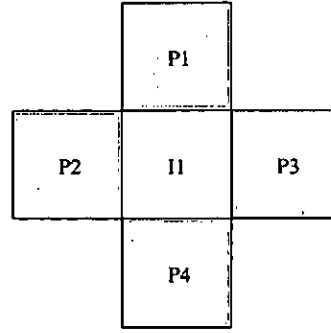


Figure 7.10: *Illustration of the interpolation step.*

White balance: The colour matrix and offsets were determined under a certain illumination (in this case standard illuminant D65). If the image is taken under different lighting conditions the RGB data will not be correctly balanced such that neutral objects still appear grey. This can be corrected by applying suitable gains to the individual RGB channels.

Aperture correction: The interpolation process causes a loss of high frequency detail in the data, which causes a blurring of sharp edges. The roll-off in lens MTF at high spatial frequencies can also contribute to this loss. To recover these edges, a monochrome high pass-filtered version of the original data can be added after the colour reconstruction. For historical reasons, this process is known as *aperture correction*.

With Bayer data, the green data alone is normally used for aperture correction [12]. This green data is of course sampled at a higher spatial frequency than either red or blue. In this project both spectral responses from the $n_{well}/p_{substrate}$ pixel outputs have been used. With cyan and yellow filters both pixel outputs contain a wide portion of the spectrum (including green) which allows them both to be used effectively. The $n_{well}/p_{substrate}$ outputs were preferred to the p^+/n_{well} due to the gain uniformity problem with the latter (see section 6.3.4). This is unfortunate, as cross-talk measurements and device simulations show that the p^+/n_{well} values would be sharper.

The construction of the high pass data is accomplished using a simple Laplacian filter [101]. Referring to Figure 7.11, the construction of a high pass value for pixel P_3 can be accomplished using the following filter:

$$H_3 = 4P_3 - P_1 - P_2 - P_4 - P_5 \quad (7.7)$$

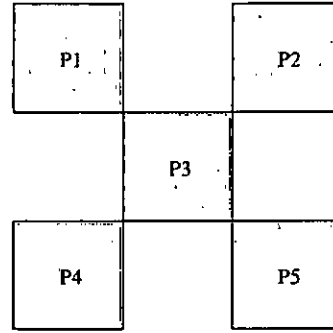


Figure 7.11: *Pixels used to create high pass filtered data.*

where H_3 is the high pass filtered value for pixel P_3 .

Values for alternate pixels will of course come from different coloured pixel data. The two different pixel colours have different sensitivities which must be corrected by using a suitable gain term. Before the high-frequency data is scaled and added to the colourised values, it is thresholded. This is because, in flat areas of the image where no edges are present, the high-pass filter data primarily contains an enhanced version of the temporal noise. By thresholding, the data in these regions is discarded and set to zero.

7.3.2 Example reconstruction

To illustrate the reconstruction process the output of each of the stages is shown below. Figure 7.12 shows the stages up to colour matrixing. The effects of applying the gain map to the p^+/n_{well} pixel data can be seen — the resulting picture is much smoother. The decimation reduces the number of pixels in each channel by a factor of 2. This naturally reduces the resolution of the data for each spectral response, as would be the case if a CFA was present on the sensor. After interpolation there is a large reduction the sharpness of the image as examination of the writing in the image shows — the interpolation process does not restore the lost data.

Figure 7.13 illustrates the steps made to produce the final colour image from the interpolated data. After the colour matrix and offsets are applied RGB data values exist for every pixel in the image. These are shown separately in the figure. When they are combined to produce the colour image as shown, a lot of high frequency data has been lost due to interpolation. To recover the lost high frequency information, the high pass filtered data from the aperture correction block is added to the colour image. It can be seen that the edges and other details in the final image are considerably sharper (the text can be discerned once more), and overall the image is much

more pleasing.

7.4 Colour aliasing

The colour aliasing properties of the sensor were examined using a test pattern. The test pattern, termed a 2-D *chirp*, contains frequency modulated concentric circles of linearly increasing frequency from one corner of the image to the other. Such a test pattern allows the aliasing properties of the imager to be measured for all angles up to the maximum spatial frequency of the chirp.²

To test a sensor, a chirp is first generated of the correct size and maximum spatial frequency. Then, an colour image of the chirp is taken with the sensor.

The chirp picture shown in Figure 7.15 was taken with the double junction sensor using cyan and yellow filters. The maximum horizontal frequency is equal to $f_{pix}/2$, i.e. the Nyquist frequency. The sampling of the colour responses of this sensor is lowest in the 45 degree angle, and it can be seen that it is indeed in this direction that aliasing first occurs. Figure 7.16 shows the same image after aperture correction, which reduces the apparent effect of the aliasing somewhat.

The aliasing properties of the sensor can be compared with the Bayer pattern simply by taking a image of the chirp with a Bayer sensor (Fig. 7.17). It should be noted that the Bayer sensor had a resolution of 368×308 pixels, therefore the image is much smoother and the bilinear interpolation artifacts are less noticeable than with the QCIF double junction device.

With Bayer, the aliasing appears blue and orange moiré in the horizontal or vertical directions, while as magenta and green in the 45 degree direction. There are two different aliasing effects therefore. Where the two effects overlap, this appears like concentric circles in the middle of the lower half of the image. In the double junction image, there is only one type of aliasing. The moiré patterns are composed of magenta, cyan, and yellow, which implies equal aliasing in all three RGB channels as expected. This behaviour is preferable to that of the Bayer pattern as it allows the lens and other parts of the system MTF to be optimised for all pixels. The sampling rate of the colour signals is lowest in the 45 degree direction which is where the aliasing first

²The program to generate the chirp chart was authored by Dr Stewart G. Smith of STMicroelectronics. Thanks are also due to Matthew Purcell who was deeply involved with the chirp measurements.

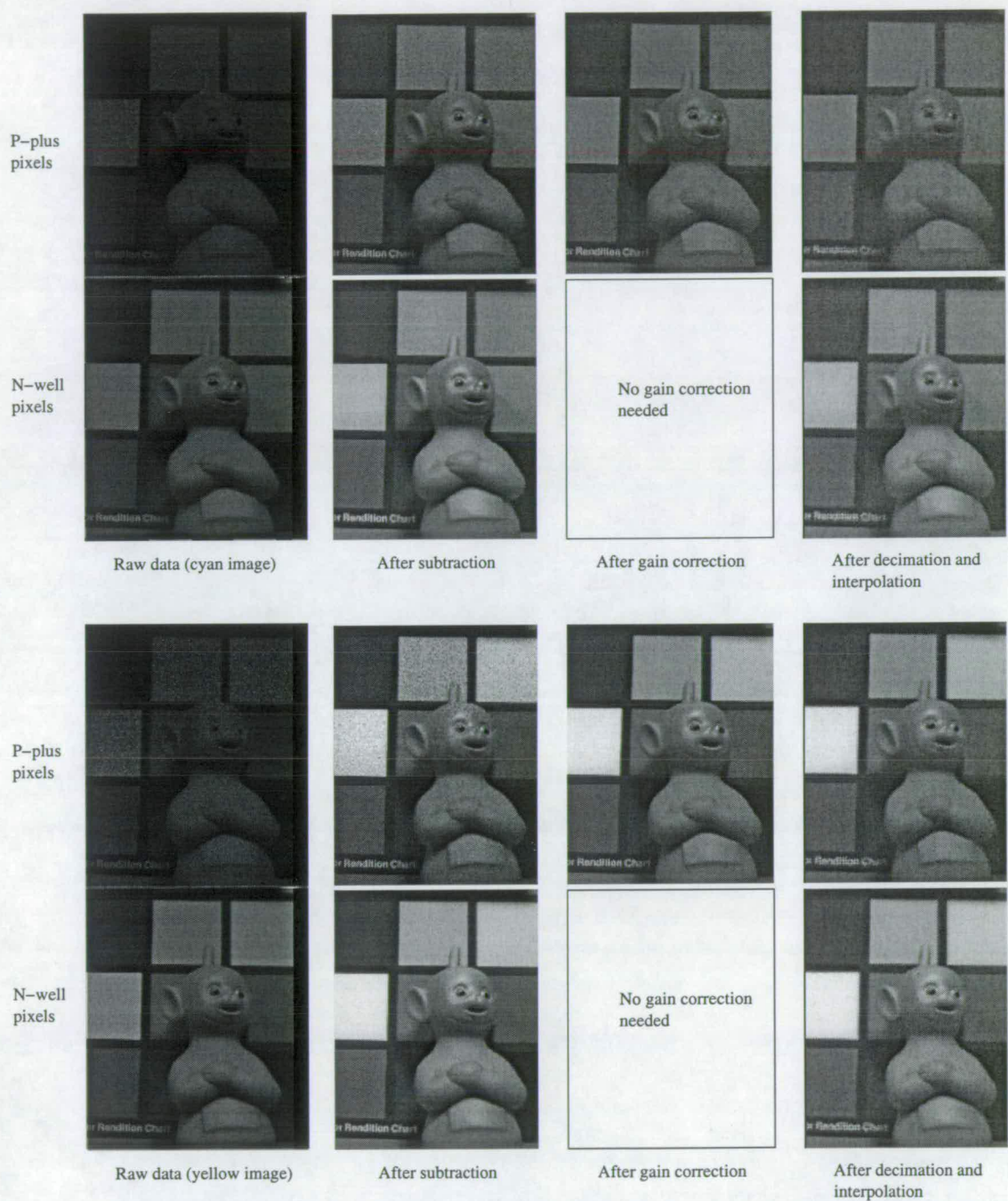


Figure 7.12: Image reconstruction steps prior colour matrixing.

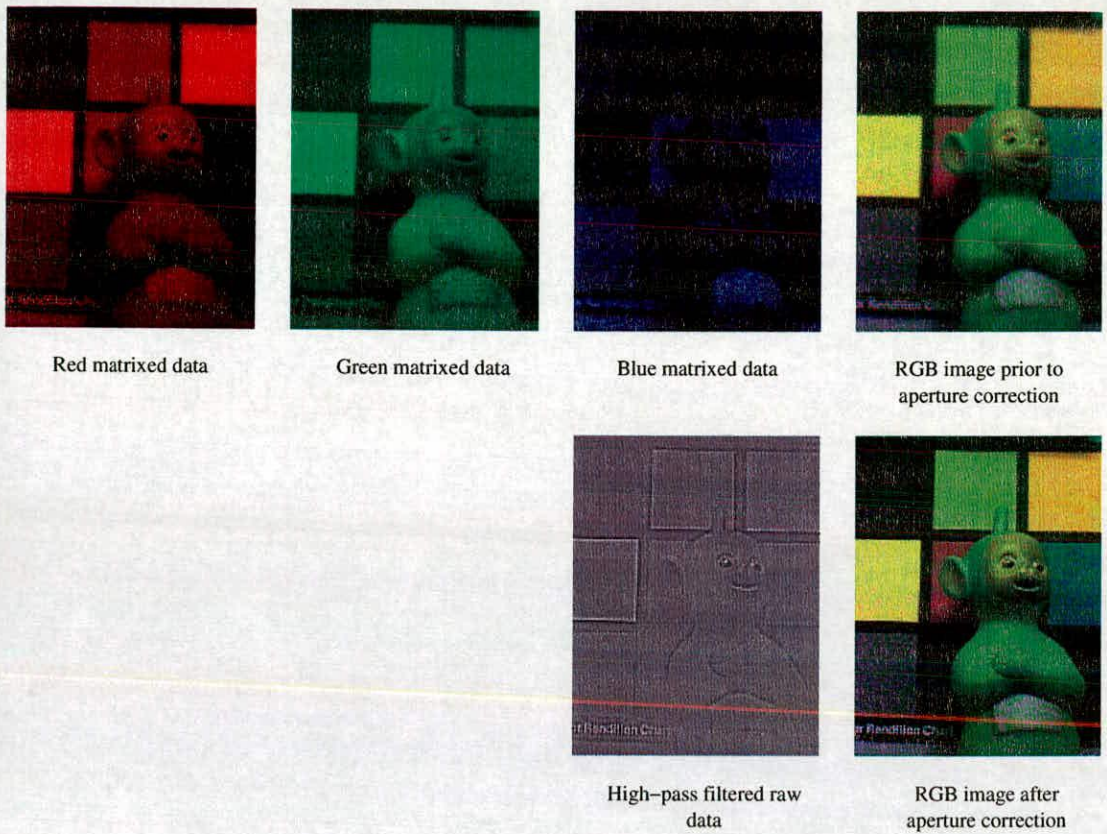


Figure 7.13: *Image reconstruction steps to produce final colour image.*

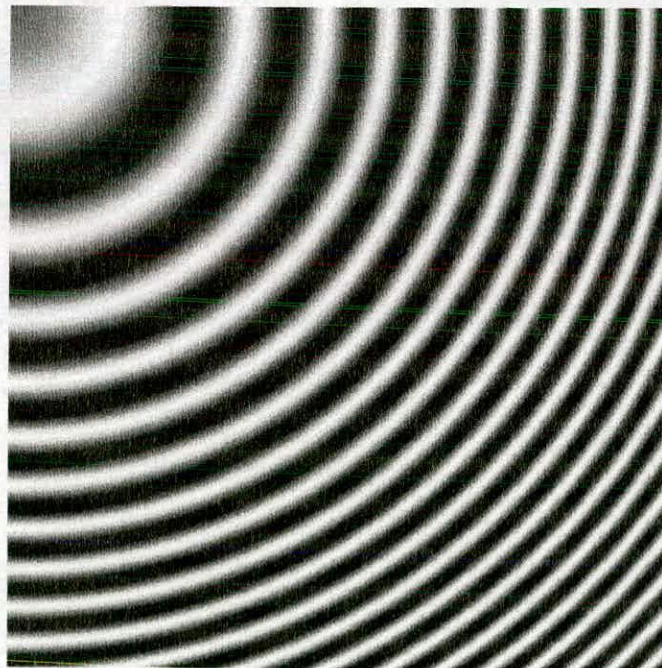


Figure 7.14: *A chirp chart.*

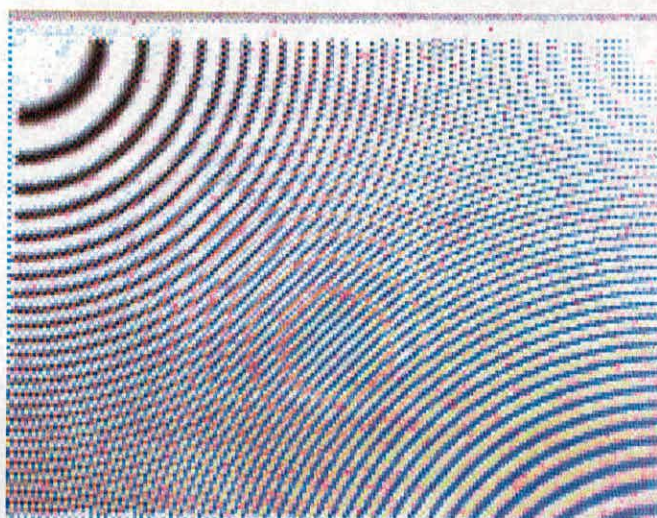


Figure 7.15: *Image of a chirp chart taken with the double junction sensor without aperture correction.*

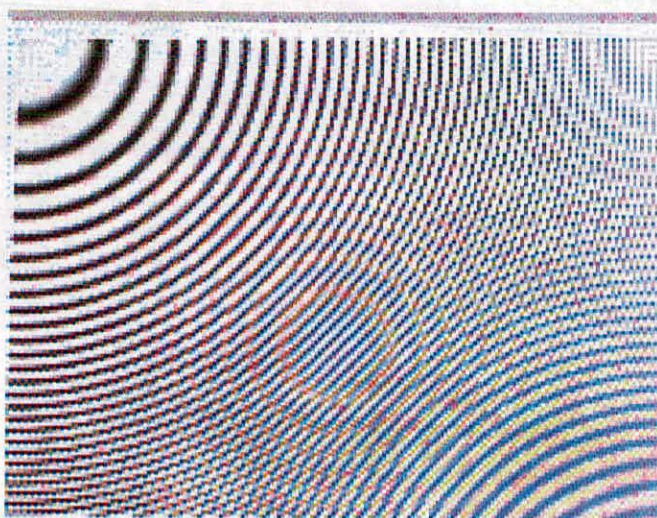


Figure 7.16: *Image of a chirp chart taken with the double junction sensor with aperture correction.*

occurs.

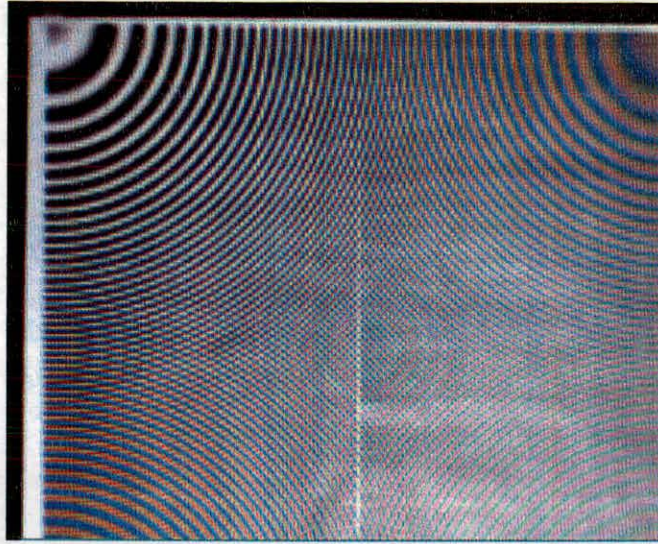


Figure 7.17: Image of a chirp chart taken with a Bayer patterned sensor.

7.5 Conclusion

This chapter has demonstrated that the double junction approach can be successfully used to produce a colour camera system. Figures 7.18-7.19 show a selection of images obtained from the sensor. While these pictures show that reasonable images can be obtained with the camera, the image quality is some way behind commercial systems (Figure 7.20 shows an image taken with a commercial digital stills camera). With the present device, the overall performance of the camera system suffers due to the non-optimal spectral responses. For the technique to be commercially viable this would have to be improved; optimisation of the raw spectral response of the photo-junctions and tailoring the filter responses used would be the first tasks to undertake. In the final chapter, the feasibility of such optimisation is discussed.

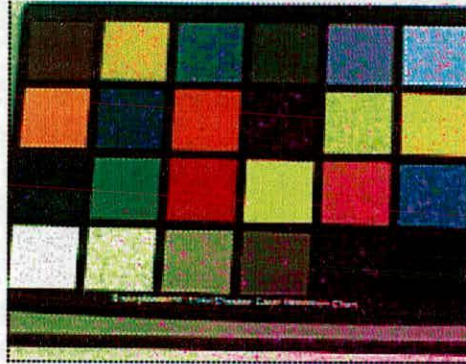


Figure 7.18: *Example image: the Macbeth colour chart.*

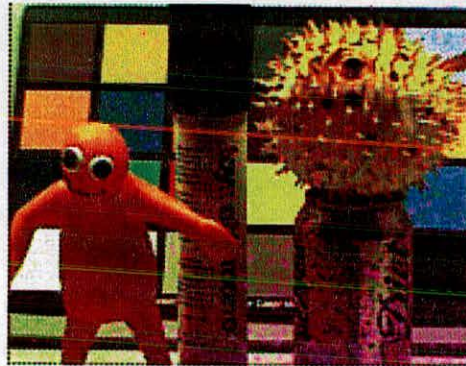


Figure 7.19: *Example image: toys and caffeine (essential project ingredients).*

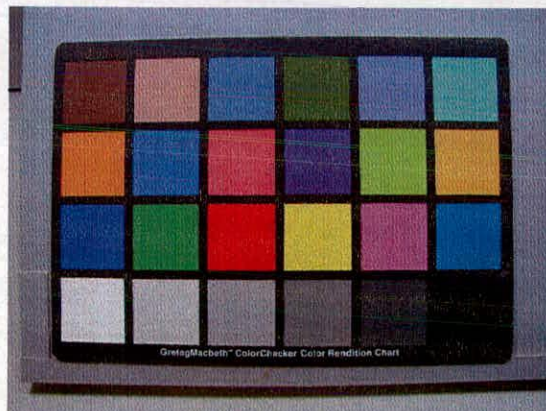


Figure 7.20: *Image of the Macbeth colour chart taken with a commercial digital stills camera.*

Chapter 8

Conclusion

8.1 Critical discussion of current approach

This thesis has evaluated the performance that can be obtained from a double junction image sensor implemented in a standard CMOS technology. The sensor is the first two dimensional image sensor array to be designed using this approach, and as has been shown, produces colour images of acceptable quality, though not as good as using a single photo-diode and RGB filters. The project has covered the design of a CMOS camera from the very low level, such in the quantum efficiency measurement and TCAD modelling of photo-diode structures, through the design of an active pixel and image sensor, to the high-level processing used to obtain final colour images.

The main advantages of the approach are:

- The spectral selectivity of the pixel photo-diode structure allows wider bandwidth colour filters to be used in the array. This is an advantage in low light levels, as the image sensor can convert more of the incident light into signal.
- The colour aliasing artifacts of the sensor are reduced due to the even spatial sampling of all four spectral responses, without the use of sophisticated anti-aliasing algorithms.
- The luminance data of the image is also sampled at a high rate due to the wider bandwidth colour filters used, which provides excellent image sharpness data for a given number of pixels.
- The larger pixel capacitance of the $n_{well}/p_{substrate}$ relative to a smaller standard pixel gives a larger peak SNR and dynamic range.

Unfortunately, there are also significant disadvantages:

- Given the $0.35\ \mu m$ technology used, the pixel size of $9.6\ \mu m$ is quite large. Very recently, a 3T pixel with $3.9\ \mu m$ pitch has been demonstrated in $0.35\ \mu m$ technology [102].

- The colorimetric accuracy of the manufactured sensor is significantly worse than with the standard approach.
- The p^+/n_{well} pixel output SNR and dynamic range are lower, as the voltage range for this output is restricted.
- The non-uniformity of the p^+/n_{well} pixel outputs is also a problem.
- Finally, the sensitivity of the proto-type sensor is also very low.

At the moment, the advantages are certainly outweighed by the disadvantages. The sensitivity of the present sensor is not a fundamental limitation of the approach *per se*, but rather a product of a non-optimised pixel design. It is likely that the non-uniformity problem can also be cured by altering the pixel layout. The voltage range and hence saturation SNR of the pixel can be increased by the use of low V_T source follower transistors and voltage doublers to increase the reset voltages. However, these techniques are equally applicable to the standard approach. The other disadvantages are harder to address. In particular the colorimetric accuracy is a function of the photo-diode doping profile, which is technology dependent and can only be optimised by increasing the process complexity.

The most significant disadvantage is the pixel size, particularly for large arrays. In the semiconductor industry, product development is driven by cost even more than by performance, and naturally a larger sensor die size would lead to a more expensive product. Once again, process enhancements are needed in order to reduce the pixel size by reducing the spacing rules between P+ and N-well layers. In a standard technology, when compared with simpler pixel designs, the double junction pixel is just too large to be competitive.

8.2 Improvements to project approach

As the range of techniques and disciplines required is very wide, certain aspects of the project have necessarily been covered lightly. In the colour processing chapter, simple algorithms were used for interpolation and no adaptive white balance or exposure control algorithm has been developed. It is likely that by using higher order algorithms for interpolation better results would be obtained. It might also be worth investigating the use of alternative fitting methods to perform colour correction. In a commercial camera, adaptive white balance and exposure control would certainly be required.

The raw performance of the sensor needs to be improved to be competitive with the standard approach. While certain parameters, such as the spectral response, are dependent on the process technology and hence beyond the scope of what can be easily altered, especially in an academic project such as this, there are certain aspects of the pixel performance that *are* under the control of the designer.

For example, the layout of the light shield and micro-lens are clearly not optimised, which results in a lower than expected sensitivity. There is also a problem with the conversion gain uniformity in which the pixel layout may be a factor. It is also unlikely that the pixel dark current, capacitance, or dynamic range are optimised.

All these problems may be addressed by performing a series of pixel experiments. The number of silicon runs is always limited, so these experiments should be performed using a *multipixel array*. With a multipixel array, the array is divided into blocks of a given size. For example, with a block size of 25×25 pixels, 42 different pixel variants can be evaluated using a QCIF pixel array. Each block still contains enough pixels to generate the statistics to calculate noise performance, dark current, sensitivity etc. Future projects that focus on a new pixel design should always adopt this approach as there are too many process dependent unknowns to ensure that a single pixel variant will be optimised. A disadvantage of a multipixel array is that it will not produce a uniform image, therefore for a camera system an extra device with only one pixel type must be manufactured.

With the benefits of the results from evaluation of the proto-type sensor, the following experiments can be suggested:

- The light shield and micro-lens layout should be investigated to see what sensitivity improvements can be made. It is suggested that, with a micro-lens present, a wider opening could be made in the light shield which would improve the device sensitivity. For each variation, the colorimetric accuracy should also be evaluated to ensure that the spectral selectivity of the junction responses is still maximised. The light shield may also be more effective if moved to a lower layer of metallisation, such as metal 2, and this should also be investigated, though it will certainly make the routing of signals through the pixel array more difficult.
- The surface P-type layer of the photo-diode structure could be formed from a variety of implants — P^+ only, $PLDD$, and $P^+/PLDD$. The pixel of the prototype sensor used

$P^+/PLDD$. It is possible that one of the other options might reduce the non-uniformity of the junction conversion gain. A series of different N-well to P^+ spacings should also be tried, as at the moment the spacing is at the minimum specified by the design rules. A different spacing may also improve the uniformity.

- The N-well layer interacts with the surface P-type region to form the top junction. Recently, alternative N-well implants have become available in the technology, and these too should be evaluated.
- Currently, the pixel size is limited by the well spacing rules. These rules are imposed to reduce the risk of latch-up, but as there is not much switching activity in the pixel array, it might be possible to break this rule, allowing a smaller pixel size, or a larger photo-diode fill-factor. Therefore, a selection of spacings above and below the design rule should be tried as part of the multipixel array.

8.3 Future work

Image sensor manufacturing technology is constantly improving, with manufacturers adding extra process modules in order to boost the optical performance, lower the dark current, etc. Most often, this involves the use of extra pixel-specific ion implantation steps.

This work has been carried out entirely within a standard CMOS technology without using special process steps. If extra implants, or other custom process steps, are available, more specialised photo-diode structures can be produced.

8.3.1 Triple well double junction structure

One limitation of the double junction approach is that the p^+/n_{well} output voltage is referenced to the $n_{well}/p_{substrate}$. This reduces the effective voltage range for the p^+/n_{well} and hence the dynamic range. By using an extra layer in the photo-diode this problem can be overcome as is shown in Figure 8.1. This extra well is sometimes available in advanced CMOS processes, where it is used for isolation purposes. With the middle p_{well} grounded both n-type regions can discharge independently which allows a pixel circuit such as is shown in Figure 8.2.

There are actually three photo-junctions in the triple-well structure, but with the p_{well} and $p_{substrate}$ both grounded, the two lower junctions are in parallel and the photo-current is in-

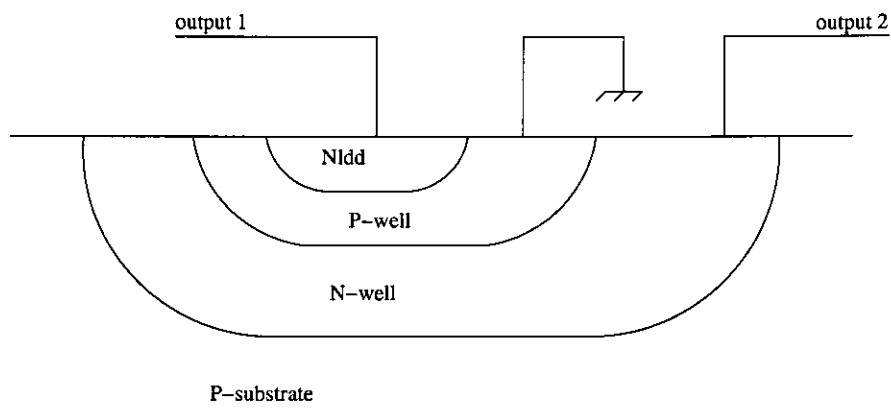


Figure 8.1: Triple-well structure.

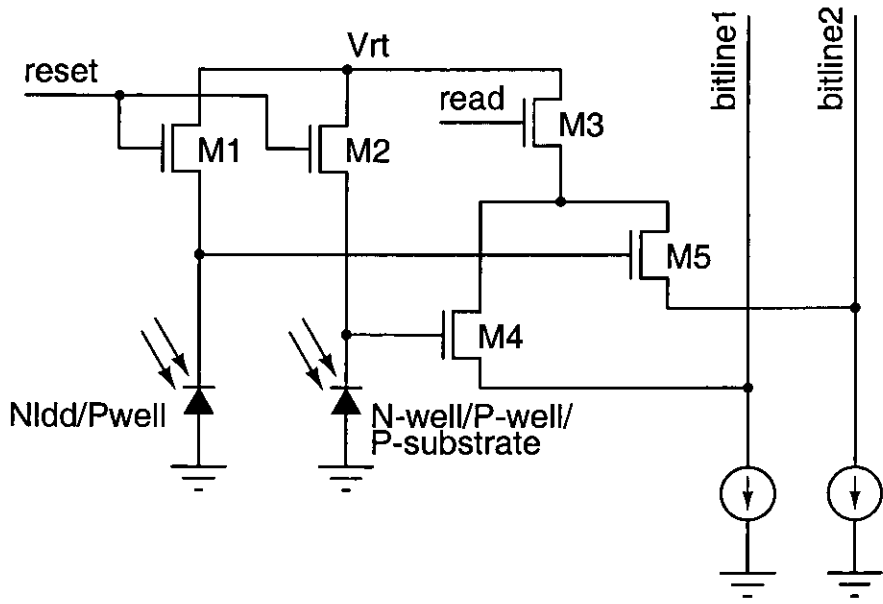


Figure 8.2: Triple-well double junction pixel.

tegrated on the n_{well} . The pixel circuit is fundamentally two 3-T cells with the read select transistor (M3) shared between the two source followers (M4 and M5). The full voltage range, from V_{rt} down to the minimum input voltage of the source follower, can be used for both integrating nodes, which maximises the full-well. The readout and reconstruction process will also be simpler, as it is no longer required to subtract one output from the other. This should also improve the noise performance slightly. One major disadvantage of this approach, however, is the extra area required for the third junction. It might therefore be even more difficult to produce a compact pixel with this photo-diode structure than it was with the double junction.

8.3.2 Amorphous silicon structures

It should be possible to duplicated the double junction pixel used in this thesis using amorphous silicon. However, this requires a method to isolate the photo-diodes from each other, and connect the circuitry to the individual layers, i.e. a means of patterning and connecting to every layer. It seems that a n - p - n sandwich (Fig. 8.3a) with the p -layer connected to ground and the integration taking place on the n -regions would have all the advantages of the triple-well structure. The same pixel circuitry could be used, but implemented underneath the amorphous. This would allow smaller pixels while still maintaining the fill-factor. Additionally, it should be much easier to improve the spectral separation of the responses in amorphous silicon by adjusting the layer thicknesses, doping levels, and band-gaps. However, a colour filter array would obviously be required, and to date the combination of an a-Si image sensor with a CFA has not been presented. It is hard to say how difficult the manufacturing challenges of producing such a sensor would be.

To produce a colour imager without colour filters, extra layers of amorphous could also be used. Alternatively, a standard photo-diode could be placed under the amorphous layers to collect photons that were not absorbed (Fig 8.3b). These photons would, on average, be of longer wavelength, resulting in a third spectral response. It is likely that significant optimisation work would be required to achieve good colour separation between the responses.

A third option would be to use the double junction structure as implemented in this thesis, with a single amorphous photo-diode implemented above to generate a third response (Fig. 8.3c). In theory, the amorphous response could be optimised to collect blue light (and act as a blue filter above the double junction structure), again resulting in three responses sampled at the spatial frequency of the pixels.

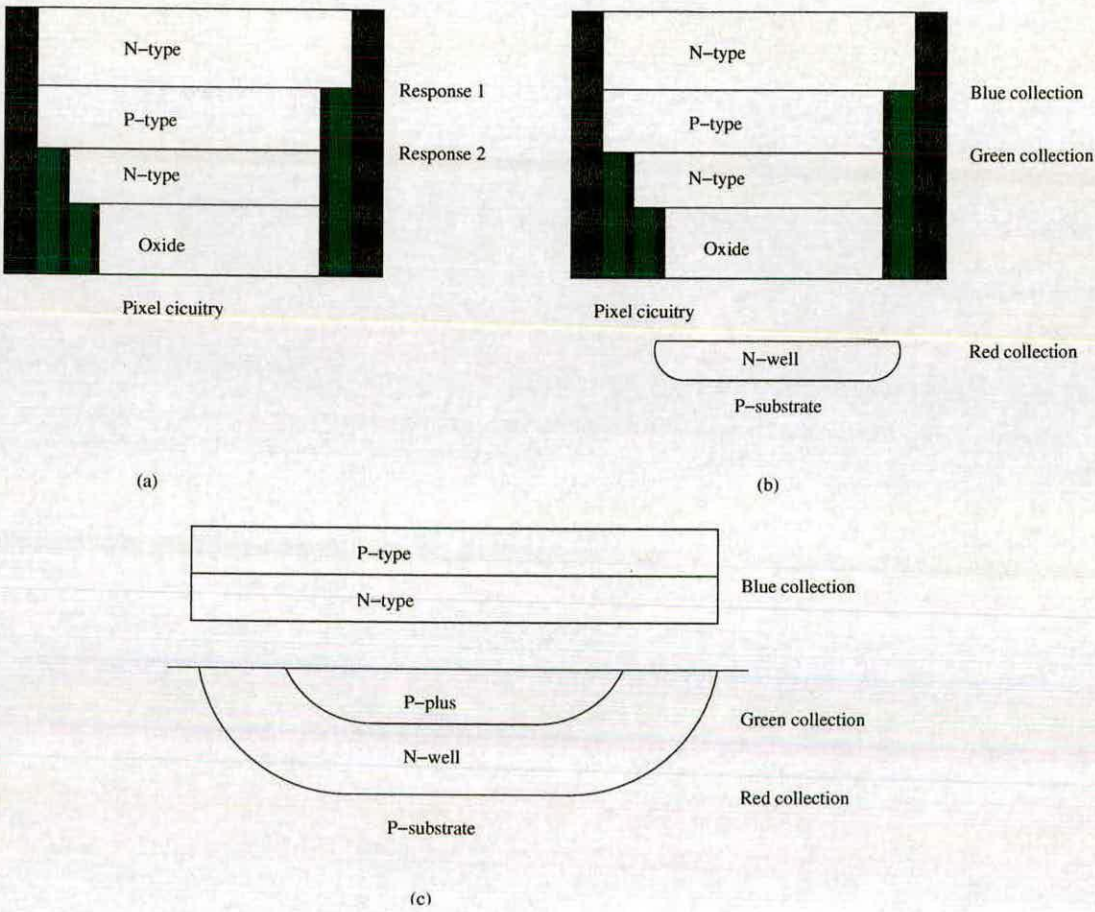


Figure 8.3: Colour sensing pixels using amorphous silicon.

8.4 Final remarks

Throughout the preparation of this thesis, the commercial interest in CMOS image sensors has increased dramatically. More and more companies are prepared to develop CMOS manufacturing technologies with enhanced imaging performance. This work, on the other hand, has worked strictly within the standard CMOS process without optimisation. It is clear that for the double junction approach to be commercially viable a similar allocation of development resources is required. However, the concept of colour imaging with a reduced filter set and a multi-junction photo-diode has been proven. Unfortunately, as the performance compares unfavourably with the already established techniques, it seems unlikely that the required optimisation work will be attempted.

Appendix A

List of publications

1. K.M. Findlater, P.B. Denyer, R.K. Henderson, J.E.D. Hurwitz, J.M. Raynor, D. Renshaw, "Buried double junction pixel using green & magenta filters", *IEEE Workshop on CCDs & Advanced Image Sensors*, Karuizawa, Nagano Japan, pp. P6.1-6.4, June 1999
2. J. Hurwitz, S. Smith, A. Murray, P. Denyer, J. Thomson, S. Anderson, E. Duncan, A. Kinsey, B. Paisley, E. Christison, B. Laffoley, J. Vittu, R. Bechignac, R. Henderson, M. Panaghiston, P. Pugibet, H. Hendry, K. Findlater, "A Miniature Imaging Module for Mobile Applications", *2001 IEEE International Solid-State Circuits Conference*, San Francisco, California, P6.2, February 2001
3. K.M. Findlater, D. Renshaw, J.E.D. Hurwitz, R.K. Henderson, T.E.R. Bailey, S.G. Smith, M.D. Purcell, J.M. Raynor, "A CMOS image sensor employing a double junction photodiode", *IEEE Workshop on CCDs & Advanced Image Sensors*, Lake Tahoe, Nevada USA, pp. P53, June 2001

References

- [1] J. D. E. Beynon and D. R. Lamb, *Charge-coupled devices and their applications*. McGraw-Hill, 1980.
- [2] G. C. Holst, *CCD arrays cameras and displays*. JCD publishing, 1996.
- [3] W. Boyle and G. Smith, "Charge-coupled semiconductor devices," *Bell Systems Technical Journal*, vol. 49, pp. 587–593, 1970.
- [4] G. P. Weckler, "Operation of p - n junction photodetectors in a photon flux integrating mode," *Journal of Solid-State Circuits*, vol. 2, pp. 65–73, Sep 1967.
- [5] D. Renshaw *et al.*, "ASIC vision," in *IEEE Custom Integrated Circuits Conference*, pp. 7.3.1 – 7.3.4, 1990.
- [6] S. G. Smith *et al.*, "A single-chip CMOS 306 x 244-pixel NTSC video camera and a descendant coprocessor device," *Journal of Solid-State Circuits*, vol. 33, pp. 2104–2111, Dec 1998.
- [7] M. J. Loinaz *et al.*, "A 200-mW, 3.3-V, CMOS color camera IC producing 352 x 288 24-b video at 30 frames/s," *Journal of Solid-State Circuits*, vol. 33, pp. 2093–2103, Dec 1998.
- [8] D.D.Oprian *et al.*, "Design, chemical synthesis, and expression of genes for the 3 human color-vision pigments," *BIOCHEMISTRY*, vol. 30, no. 48, 1991.
- [9] R. W. G. Hunt, *The reproduction of colour*. Fountain Press, 5th ed., 1995.
- [10] E. Hecht and A. Zajac, *Optics*. Addison-Wesley, 1974.
- [11] B.E.Bayer, "Color imaging array." U.S. Patent 3 971 065, Mar 1975.
- [12] P. L. P. Dillon *et al.*, "Color imaging system using a single CCD area array," *Journal of Solid-State Circuits*, vol. 13, pp. 28–33, Feb 1978.
- [13] K. A. Parulski, "Color filters and processing alternatives for one-chip cameras," *IEEE Transactions on Electron Devices*, vol. 32, pp. 1381–1389, Aug 1985.
- [14] J. Hurwitz *et al.*, "A miniature imaging module for mobile applications," in *IEEE International Solid-State Circuits 2001 Conference Digest of Technical Papers*, p. P6.2, February 2001.
- [15] J.Adams, K.Parulski, and K.Spaulding, "Color processing in digital cameras," *IEEE Micro*, vol. 18, Nov.-Dec. 1998.
- [16] T. Toi, "Color signal processing technique for single-chip CCD cameras that employ CPUs with SIMD instruction sets," *IEEE Transactions on Consumer Electronics*, vol. 46, no. 2, 2000.

- [17] J. E. Adams, "Interactions between color plane interpolation and other image processing functions in electronic photography," *Proceedings of SPIE*, vol. 2416, 1995.
- [18] T. Sakamoto *et al.*, "Software pixel interpolation for digital still cameras suitable for a 32-bit MCU," *IEEE Transactions on Consumer Electronics*, 1998.
- [19] T. Kuno and H. Sugiura, "New interpolation method using discriminated color correlation for digital still cameras," *IEEE Transactions on Consumer Electronics*, vol. 45, pp. 259–267, Feb 1999.
- [20] R. W. G. Hunt, *The reproduction of colour*, ch. 19, p. 451. Fountain Press, 5th ed., 1995.
- [21] G. C. Holst, *CCD arrays cameras and displays*, ch. 5, pp. 138–146. JCD publishing, 1996.
- [22] O. Christensen, "Quantum efficiency of the internal photoelectric effect in silicon and germanium," *Journal of Applied Physics*, vol. 47, pp. 689–695, Feb 1976.
- [23] S. G. Chamberlain *et al.*, "Spectral response limitation mechanisms of a shallow junction n+-p photodiode," *Journal of Solid-State Circuits*, vol. 13, pp. 167–172, Feb 1978.
- [24] S. M. Sze, *Physics of Semiconductor Devices*, ch. 13, pp. 749–783. John Wiley & Sons, 2nd ed., 1981.
- [25] S. G. Chamberlain, "New profiled photodetector for improved short-wavelength quantum efficiency," *Journal of Applied Physics*, vol. 50, pp. 7228–7231, Nov 1979.
- [26] D. J. Roulston *et al.*, "Modeling and measurement of minority-carrier lifetime versus doping in diffused layers of $n^+ - p$ silicon diodes," *IEEE Transactions on Electron Devices*, vol. ED-29, no. 2, pp. 283–291, 1982.
- [27] S. Park *et al.*, "Optical sensitivity and barrier property depending on ILD layers of CMOS image sensor device," in *6th International Conference on VLSI and CAD*, pp. 211–213, 1999.
- [28] W. C. Dash and R. Rewman, "Intrinsic absorption in single crystal germanium and silicon and 77°K and 300°K," *Physical Review*, vol. 99, pp. 1151–1155, 1955.
- [29] H. Philipp and E. Taft, "Optical constants of silicon in the region 1 to 10 eV," *Physical Review*, vol. 120, pp. 37–38, Oct 1960.
- [30] D. Schroder, R. Thomas, and J. Swartz, "Free carrier absorption in silicon," *Journal of Solid-State Circuits*, vol. SC-13, pp. 180–187, Feb 1978.
- [31] S. Jain, A. Nathan, D. Briglio, D. Roulston, C. Selvakumar, and T. Yang, "Band-to-band and free-carrier absorption coefficients in heavily doped silicon at 4 K and room temperature," *Journal of Applied Physics*, vol. 69, pp. 3687–3690, Jul 1991.
- [32] A. Moini, "Vision chips or seeing silicon," tech. rep., Centre for High Performance Integrated Technologies and Systems, The University of Adelaide, Mar 1997.
- [33] J. Beynon and D. R. Lamb, *Charge-Coupled Devices and their Applications*, ch. 3. McGraw-Hill, 1980.

- [34] D.-N. Yaung *et al.*, "Effects of hydrogen annealing on 0.25 μm cmos image sensor," in *IEEE Workshop on CCDs and Advanced Image Sensors*, p. P21, June 2001.
- [35] M. Bartek *et al.*, "An integrated silicon colour sensor using selective epitaxial growth," *Sensors and Actuators A: Physical*, vol. 41-42, pp. 123-128, 1994.
- [36] S. Mohajerzadeh, A. Nathan, and C. R. Selvakumar, "Numerical simulation of a p-n-p-n color sensor for simultaneous color detection," *Sensors and Actuators A: Physical*, vol. 44, pp. 119-124, 1994.
- [37] R. Merrill, "Color separation in an active pixel cell imaging array using a triple-well structure." U.S. Patent 5 965 875, Oct 1999.
- [38] M. B. Chouikha *et al.*, "Colour detection using buried triple pn junction structure implemented in BiCMOS process," *Electronics Letters*, vol. 34, pp. 120-122, Jan 1998.
- [39] P. Seitz, D. Leipold, J. Kramer, and J. Raynor, "Smart optical and image sensors fabricated with industrial CMOS/CCD semiconductor processes," in *Proceedings of SPIE*, vol. 1900, pp. 21-30, Feb 1993.
- [40] G. de Graaf and R. F. Wolffenbuttel, "Smart optical sensor systems in CMOS for measuring light intensity and colour," *Sensors and Actuators A: Physical*, vol. 67, pp. 115-119, 1998.
- [41] M. B. Chouickha *et al.*, "A CMOS linear array of BDJ color detectors," in *Proc. of SPIE*, vol. 3410, pp. 46-53, Jun 1999.
- [42] G. Lu *et al.*, "Colour detection using a buried double p-n junction structure implemented in the CMOS process," *Electronics Letters*, vol. 32, Mar 1996.
- [43] M.B.Chouikha *et al.*, "Photodetector based on buried junctions and a corresponding method of manufacture.." U.S. Patent 5 883 421, Mar 1999.
- [44] M. L. Simpson *et al.*, "Application specific spectral response with CMOS compatible photodiodes," *IEEE Transactions on Electron Devices*, vol. 46, pp. 905-913, May 1999.
- [45] G. de Graaf, J. Correia, M. Bartek, and R. Wolffenbuttel, "On-chip integrated CMOS optical microspectrometer with light-to-frequency converter and bus interface," in *IEEE International Solid-State Circuits 1999 Conference Digest of Technical Papers*, pp. 208-209, 1999.
- [46] R. Muller and T. Kamins, *Device Electronics for Integrated Circuits*, ch. 4. John Wiley & Sons, 2nd ed., 1986.
- [47] R. Wolffenbuttel, "A simple integrated color indicator," *Journal of Solid-State Circuits*, vol. SC-22, pp. 350-355, June 1987.
- [48] R. Wolffenbuttel, "Operation of the silicon colour filtering element," *Sensors and Actuators*, vol. 16, pp. 13-23, Feb 1989.
- [49] R. F. Wolffenbuttel and G. de Graaf, "Performance of an integrated silicon colour sensor with a digital output in terms of response to colours in the colour triangle," *Sensors and Actuators A: Physical*, vol. 21-23, pp. 574-580, 1990.

- [50] R. Street, R. Weisfield, S. Nelson, and R. Chang, "Page-sized amorphous silicon image sensor arrays," in *Proceedings of SPIE*, vol. 1900, pp. 135–146, Feb 1993.
- [51] H. Kakinuma *et al.*, "Direct-contact type image sensors using a novel amorphous-silicon photodiode array," *IEEE Electron Device Letters*, vol. 12, p. 413415, Aug 1991.
- [52] B. Schneider *et al.*, "TFA image sensors: From the one transistor cell to a locally adaptive high dynamic range sensor," in *IEDM Technical Digest*, pp. 8.7.1–8.7.4, 1997.
- [53] H.-S. Wong, "Technology and device scaling considerations for CMOS imagers," *IEEE Transactions on Electron Devices*, vol. 43, pp. 2131–2142, Dec 1996.
- [54] H.-S. P. Wong, "CMOS image sensors - recent advances and device scaling issues," in *IEDM Technical Digest*, pp. 8.5.1–8.5.4, 1997.
- [55] H.-S. P. Wong *et al.*, "CMOS active pixel image sensors fabricated using a 1.8-v, 0.25- μm CMOS technology," *IEEE Transactions on Electron Devices*, vol. 45, pp. 889–894, Apr 1998.
- [56] M. Sommer *et al.*, "First multispectral diode color imager with three color recognition and color memory in each pixel," in *1999 IEEE Workshop on Charge-Coupled Devices and Advanced Image Sensors*, pp. 187–190, June 1999.
- [57] J. Zimmer, D. Knipp, H. Stiebig, and H. Wagner, "Amorphous silicon-based unipolar detector for color recognition," *IEEE Transactions on Electron Devices*, vol. 46, no. 5, pp. 884–891, 1999.
- [58] T. Lule *et al.*, "Design and fabrication of a high-dynamic-range image sensor in TFA technology," *IEEE Transactions on Electron Devices*, vol. 34, pp. 704–711, May 1999.
- [59] F. Irrera, F. Lemmi, and F. Palma, "Transient behavior of adjustable threshold $\alpha\text{-Si}/\alpha\text{-SiC:H}$ three-color detector," *IEEE Transactions on Electron Devices*, vol. 44, pp. 1410–1416, Sep 1997.
- [60] D. Knipp *et al.*, "Low cost approach to realize novel detectors for color recognition," in *Proc. ICPS 98 (International Congress on Imaging Science)*, pp. 350–353, Sep 1998.
- [61] H. Stiebig *et al.*, "Transient behavior of optimized nipiin three-color detectors," *IEEE Transactions on Electron Devices*, vol. 45, pp. 1438–1444, Jul 1998.
- [62] Q. Zhu *et al.*, "Bias sensitive $\alpha\text{-Si(C):H}$ multispectral detectors," *IEEE Transactions on Electron Devices*, vol. 45, pp. 1393–1398, July 1998.
- [63] M. Topič *et al.*, "Optimization-of $\alpha\text{-Si:H}$ -based three-terminal three-color detectors," *IEEE Transactions on Electron Devices*, vol. 48, pp. 1839–1845, Sep 1999.
- [64] P. G. Herzog *et al.*, "Characterization of novel three and six channel color moiré free sensors," in *Proceedings of SPIE*, vol. 3648, pp. 48–59, Jan 1999.
- [65] G. Yu, J. Wang, J. McElvain, and A. Heeger, "Large-area, full-color image sensors made with semiconducting polymers," *Advanced Materials*, vol. 10, no. 17, pp. 1431–4, 1998.

- [66] K. Tada and K. Yoshino, "Conducting polymer color sensor," *Japanese Journal of Applied Physics: Part 2*, pp. L.1351–L.1353, Oct 1997.
- [67] G. Wu. Private communication, 1999.
- [68] N. Marston, *Solid-state imaging: a critique of the CMOS image sensor*. PhD thesis, University of Edinburgh, Nov 1998.
- [69] S. Ohba *et al.*, "MOS area sensor: Part II — low-noise MOS area sensor with antiblooming photodiodes," *Journal of Solid-State Circuits*, vol. SC-15, pp. 747–752, Aug 1980.
- [70] I. L. Fujimori *et al.*, "A 256 x 256 CMOS differential passive pixel imager with FPN reduction techniques," in *IEEE International Solid-State Circuits Conference 2000 Digest of Technical Papers*, pp. 106–107, Feb 2000.
- [71] M. Schanz *et al.*, "A high-dynamic-range CMOS image sensor for automotive applications," *Journal of Solid-State Circuits*, vol. 35, pp. 932–938, Jul 2000.
- [72] R. Guidash *et al.*, "A 0.6 μm CMOS pinned photodiode color imager technology," in *IEDM Technical Digest*, pp. 8.8.1–8.8.3, 1997.
- [73] I. Inoue *et al.*, "Low dark current pinned photo-diode for CMOS image sensors," in *1999 Workshop on Charge-Coupled Devices and Advanced Image Sensors*, pp. 25–28, June 1999.
- [74] N. Teranishi *et al.*, "No image lag photodiode structure in the interline CCD images sensor," in *International Electron Device Meeting Technical Digest*, pp. 324–327, 1982.
- [75] W. Yang *et al.*, "An integrated 800x600 CMOS imaging system," in *IEEE International Solid-State Circuits 1999 Conference Digest of Technical Papers*, pp. 304–305, Feb 1999.
- [76] S. Agwani *et al.*, "A 1/3" VGA CMOS imaging system on a chip," in *1999 IEEE Workshop on Charge-Coupled Devices and Advanced Image Sensors*, pp. 21–24, June 1999.
- [77] K. Yonemoto *et al.*, "A CMOS image sensor with a simple FPN-reduction technology and a hole accumulated diode," in *IEEE International Solid-State Circuits Conference 2000 Digest of Technical Papers*, pp. 102–103, Feb 2000.
- [78] T. Sugiki *et al.*, "A 60mW 10b CMOS image sensor with column-to-column FPN reduction," in *IEEE International Solid-State Circuits Conference 2000 Digest of Technical Papers*, pp. 102–103, Feb 2000.
- [79] B. Burkey *et al.*, "The pinned photodiode for an interline-transfer CCD image sensor," in *International Electron Devices Meeting Technical Digest*, pp. 28–31, 1984.
- [80] T. Kuriyama, "A 1/3-in 270000 pixel CCD image sensor," *IEEE Transactions on Electron Devices*, vol. 38, pp. 949–953, May 1991.
- [81] R. H. Nixon *et al.*, "256 x 256 CMOS active pixel sensor camera-on-a-chip," *Journal of Solid-State Circuits*, vol. SC-31, pp. 2046–2050, Dec 1996.

- [82] A. J. Blanksby and M. J. Loinaz, "Performance analysis of color CMOS photogate image sensor," *IEEE Transactions on Electron Devices*, vol. 47, pp. 55–64, Jan 2000.
- [83] S. G. Chamberlain and J. P. Y. Lee, "A novel wide dynamic range silicon photodetector and linear imaging array," *Journal of Solid-State Circuits*, vol. SC-19, pp. 41–48, Feb 1984.
- [84] D. Scheffer, B. Dierickx, and G. Meynants, "Random addressable 2048 x 2048 active pixel image sensor," *IEEE Transactions on Electron Devices*, vol. 44, pp. 1716–1720, Oct 1997.
- [85] N. Ricquier and B. Dierickx, "Random addressable CMOS image sensor for industrial applications," *Sensors and Actuators A: Physical*, vol. 44, pp. 29–35, 1994.
- [86] Y. P. Tsividis, *Operation and Modeling of the MOS Transistor*, ch. 4, p. 139. McGraw-Hill, 1988.
- [87] B. Dierickx, "Random addressable active pixel image sensors," in *Proceedings of SPIE*, pp. 2–7, October 1996.
- [88] S. Kavadias, "Logarithmic response CMOS image sensor with on-chip calibration," *Journal of Solid-State Circuits*, vol. 35, pp. 1146–1152, August 2000.
- [89] M. Loose, K. Meier, and J. Schemmel, "A self-calibrated single-chip CMOS camera with logarithmic response," *Journal of Solid-State Circuits*, vol. 36, pp. 586–596, April 2001.
- [90] N. Tu, R. Hornsey, and S. G. Ingram, "CMOS active pixel image sensor with combined linear and logarithmic mode operation," in *Canadian Conference on Electrical and Computer Engineering*, vol. 2, pp. 754–757, 1998.
- [91] J. Mar, "Directions for technology CAD," in *IEEE Region 10 Annual International Conference, Proceedings/TENCON*, pp. 202–203, 1995.
- [92] M. Law, "The virtual IC factory ... can it be achieved?," *IEEE Circuits and Devices Magazine*, vol. 11, no. 2, pp. 25–31, 1995.
- [93] J. D'Ignazio, "TCAD tools leap hurdles to broader use," *Semiconductor International*, vol. 19, no. 4, pp. 25–31, 1996.
- [94] Avant! Corporation, TCAD business unit, *MEDICI User's Manual*, July 2000.
- [95] Silvaco International, *ATLAS User's Manual: Volume 1*, Nov 1998.
- [96] R.H. Myers and D.C. Montgomery, *Response Surface Methodology*, ch. 10. John Wiley & Sons, 1995.
- [97] P.R. Gray and R.G. Meyer, *Analysis and Design of Analog Integrated Circuits*. John Wiley & Sons, 1993.
- [98] J. Janesick, K. Klassen, and T. Elliot, "Charge-coupled-device charge-collection efficiency and the photon-transfer technique," *Optical Engineering*, vol. 28, pp. 972–980, October 1987.

- [99] A. Theuwissen, "Course on solid-state imaging devices." CEI-Europe Course notes, 2000.
- [100] S. K. Mendis *et al.*, "CMOS active pixel image sensors for highly integrated imaging systems," *Journal of Solid-State Circuits*, vol. 32, pp. 187–197, Feb 1997.
- [101] J. C. Russ, *The Image Processing Handbook*, ch. 4, pp. 225–232. IEEE Press, 1994.
- [102] V. Berezin, "Small CMOS pixel design with single row line," in *IEEE Workshop on CCDs and Advanced Image Sensors*, p. P8, June 2001.